

NEEYATI PANDEY

**HYDROLOGICAL  
HAZARDS  
AND RISKS**

# Hydrological Hazards and Risks

---



# Hydrological Hazards and Risks

---

Neeyati Pandey



Published by The InfoLibrary,  
4/21B, First Floor, E-Block,  
Model Town-II,  
New Delhi-110009, India

© 2022 The InfoLibrary

Hydrological Hazards and Risks  
Neeeyati Pandey  
ISBN: 978-93-5590-240-5

This book contains information obtained from authentic and highly regarded sources. All chapters are published with permission under the Creative Commons Attribution Share Alike License or equivalent. A wide variety of references are listed. Permissions and sources are indicated; for detailed attributions, please refer to the permissions page. Reasonable efforts have been made to publish reliable data and information, but the authors, editors and publisher cannot assume any responsibility for the validity of all materials or the consequences of their use.

Trademark Notice: All trademarks used herein are the property of their respective owners. The use of any trademark in this text does not vest in the author or publisher any trademark ownership rights in such trademarks, nor does the use of such trademarks imply any affiliation with or endorsement of this book by such owners.

The publisher's policy is to use permanent paper from mills that operate a sustainable forestry policy. Furthermore, the publisher ensures that the text paper and cover boards used have met acceptable environmental accreditation standards.

# Table of Contents

<b>Chapter 1</b>	Correlation Analysis of Seasonal Temperature and Precipitation in a Region of Southern Italy	<b>1</b>
<b>Chapter 2</b>	An Attempt to Use Non-Linear Regression Modelling Technique in Long-Term Seasonal Rainfall Forecasting for Australian Capital Territory	<b>11</b>
<b>Chapter 3</b>	From Deterministic to Probabilistic Forecasts: The ‘Shift-Target’ Approach in the Milan Urban Area (Northern Italy)	<b>23</b>
<b>Chapter 4</b>	Impact of the Rainfall Duration and Temporal Rainfall Distribution Defined Using the Huff Curves on the Hydraulic Flood Modelling Results	<b>37</b>
<b>Chapter 5</b>	Modelling the Present and Future Water Level and Discharge of the Tidal Betna River	<b>52</b>
<b>Chapter 6</b>	A Novel Method for Evaluation of Flood Risk Reduction Strategies: Explanation of ICPR FloRiAn GIS-Tool and Its First Application to the Rhine River Basin	<b>67</b>
<b>Chapter 7</b>	Assessment of the Performance of Satellite-Based Precipitation Products for Flood Events across Diverse Spatial Scales Using GSSHA Modeling System	<b>83</b>



# Correlation Analysis of Seasonal Temperature and Precipitation in a Region of Southern Italy

Ennio Ferrari <sup>1,\*</sup>, Roberto Coscarelli <sup>2</sup> and Beniamino Sirangelo <sup>3</sup>

<sup>1</sup> Department of Computer Engineering, Modeling, Electronics, and Systems Science (DIMES), University of Calabria, 87036 Rende (CS), Italy

<sup>2</sup> Research Institute for Geo-hydrological Protection (CNR-IRPI), National Research Council of Italy, 87036 Rende (CS), Italy; r.coscarelli@irpi.cnr.it

<sup>3</sup> Department of Environmental and Chemical Engineering (DIATIC), University of Calabria, 87036 Rende (CS), Italy; beniamino.sirangelo@unical.it

\* Correspondence: ennio.ferrari@unical.it

**Abstract:** The investigation of the statistical links between changes in temperature and rainfall, though not widely achieved in the past, is an interesting issue because their physical interdependence is difficult to point out. Aiming at detecting possible trends with a pooled approach, a correlative analysis of temperature and rainfall has been carried out by comparing changes in their standardized anomalies from two different 30-year time periods. The procedure has been applied to the time series of seasonal mean temperature and cumulative rainfall observed in four sites of the Calabria region (Southern Italy), with reference to the series which verify the normality hypothesis. Specifically, the displacements of the ellipses, representing the probability density functions of the bivariate normal distribution assumed for the climatic variables, have been quantified and tested for each season, passing from the first subperiod to the following one. The main results concern a decreasing trend of both the temperature and the rainfall anomalies, predominantly in the winter and autumn seasons.

**Keywords:** seasonal precipitation; seasonal temperature; correlation analysis

---

## 1. Introduction

Rainfall and air temperature are among the most investigated meteorological variables in climatic trend studies, mainly due to the serious implications that their spatial and temporal changes can have on several environmental and socioeconomic aspects [1–3]. With regard to the temporal distribution of rainfall, long-term trends have been detected in several areas of the world [4,5]. In the Mediterranean Basin, an alternation of extreme rainy periods and severe droughts or water shortages has been detected [6]. Furthermore, this area is characterized by significant rainfall variability [7,8], caused by synoptic dynamics of extreme events evolving along this basin [9].

In Italy, which has a central position in the Mediterranean area, investigations of long rainfall series showed a decreasing trend, even if not always significant [10]. More detailed analyses have been carried out at smaller scales with varied behaviour: decreasing rainfall amounts in winter versus precipitation increase in the summer months. In particular, these behaviours were detected in the regions of Southern Italy, such as Campania [11], Basilicata [12], Sicily [13], and Calabria [14].

Regarding temperature, several studies evidenced the increase of the mean values of temperatures both at large [15] and local spatial scales [16]. The magnitude of trends varies according to the study area and the studied period. In addition, the increasing rates of maximum and minimum temperatures present a high variability. In the last decades, the analyses of temperature have been focused on the extreme values [17,18]. Salinger and Griffiths [19] showed that the changes in mean and extreme values are closely interconnected between each other and that low trends in average conditions can

generate high variations in the extremes, especially in their frequency. Donat and Alexander [20] showed that both daytime (daily maximum) and night-time (daily minimum) temperatures have become higher over the past 60 years, but at different rates: greater for minimum than for maximum values. In Italy, which can be considered as a climate change hotspot [21], variations in the probability density functions of the minimum and maximum daily temperature anomalies were studied by Simolo et al. [22]. Caloiero et al. [23] analysed the minimum and maximum monthly temperatures of 19 stations in Calabria and detected a positive trend for spring and summer months and a marked negative one in September.

In fact, an accurate joint analysis of precipitation and temperature is more difficult to be carried out because of the possible interdependence between them [24]. Nevertheless, Rajeevan et al. [25] found that temperature and rainfall in India were positively correlated during January and May, but negatively correlated during July. Huang et al. [26] showed a negative correlation between rainfall and temperature in the Yellow River basin of China. Cong and Brady [27] applied the copula models to the rainfall and temperature data of a province of Sweden, and they evidenced negative correlations in the months from April to July and in September. Caloiero et al. [14] analysed the spatial and temporal behaviour of monthly precipitation and temperature in the Calabria region (Southern Italy), comparing the Péguy climographs [28] on three subperiods of the whole observation period (1916–2010).

In this paper, a joint analysis of temperature and rainfall has been carried out, comparing time series recorded in some gauges located in Calabria (Southern Italy) over two distinct 30-year subperiods (1951–1980 and 1981–2010). In particular, the anomalies of the seasonal values of temperature and precipitation, standardized by means of the mean values and the standard deviations of the period 1961–1990, were analysed. The series have been selected based on the normality hypothesis. The isocontour lines of the probability density function for the bivariate Gaussian distribution have been considered as ellipses centred on the vector mean of each subperiods. Finally, some statistical tests were applied for verifying the variations of these ellipses passing from one subperiod to the other, aiming at detecting joint trends of the seasonal temperature and rainfall anomalies.

## 2. Materials and Methods

### 2.1. Study Area and Data

Calabria is situated in the southern part of the Italian peninsula, with an area of 15,080 km<sup>2</sup> and a perimeter of about 818 km (Figure 1). This region shows high climatic contrasts, due to the geographic position and mountainous nature. Its climate is characterized by typical subtropical summers, with colder snowy winters and fresher summers in the inland zones, typical of Mediterranean areas. Its elongated shape evidences two coastal sides with dissimilar climatic features. The Ionian coast is exposed to the warm African currents, thus experiencing high temperatures with short and heavy precipitation. In contrast, the Tyrrhenian side is more influenced by Western air currents, which cause milder temperatures and orographic precipitation.

The climatic database used in this study, managed by the former Italian Hydrographic Service, concerns the monthly values of cumulated rainfall and mean temperature of some stations characterizing the different climatic conditions of the region for the period 1951–2010. Particular attention has been given to the problems arising from the low quality and inhomogeneities of the data series. Specifically, the monthly database was a part of the high-quality one presented in a previous study, which detected the inhomogeneities through a multiple application of the Craddock test [29]. In particular, four homogeneous monthly cumulated rainfall and mean temperature series were selected, whose percentages of missing data are presented in Table 1. The main statistical features of the seasonal temperature and rainfall series for the reference period 1961–1990 are shown in Table 2.

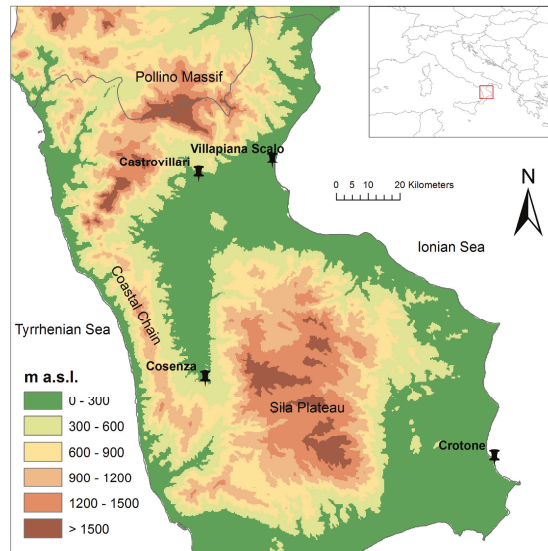


Figure 1. Location of the selected gauges in the Calabria region.

Table 1. Percentages of missing values of monthly mean temperature and cumulated rainfall.

Code	Station	Missing Data (%)					
		Monthly Temperature			Monthly Rainfall		
		1951–1980	1981–2010	Whole Period	1951–1980	1981–2010	Whole Period
930	Villapiana Scalo	0	0	0	5.8	13.6	9.7
1010	Cosenza	0	0.3	0.1	7.5	9.7	8.5
1180	Castrovillari	0	4.7	2.4	5.3	9.4	7.4
1680	Crotone	3.1	5.3	4.2	8.9	11.1	10.0

Table 2. Main statistics of temperature and rainfall for the reference period 1961–1990. ( $\bar{T}$ : mean daily temperature,  $SD_T$ : standard deviation of temperature,  $\bar{R}$ : cumulated rainfall,  $SD_R$ : standard deviation of rainfall).

Season	Station	$\bar{T}$ (°C)	$SD_T$ (°C)	$\bar{R}$ (mm)	$SD_R$ (mm)
Winter	930	10.3	0.8	231.9	81.3
	1010	8.6	1.1	405.4	149.0
	1180	9.2	1.2	371.6	134.7
	1680	11.3	0.8	234.9	89.8
Spring	930	14.9	0.9	125.2	69.0
	1010	14.1	1.4	210.1	74.3
	1180	14.6	1.2	178.0	71.2
	1680	15.4	1.4	117.1	60.3
Summer	930	24.6	1.2	41.4	26.5
	1010	24.0	1.1	64.4	36.4
	1180	24.8	1.3	78.2	57.3
	1680	25.3	1.1	31.9	27.7
Autumn	930	18.5	0.9	203.5	115.1
	1010	17.2	1.2	260.0	99.4
	1180	17.8	1.1	250.1	92.1
	1680	19.4	0.8	250.2	117.1

## 2.2. Methods

The statistical approach here used to explore the relationships between climatic data series which are not perfectly similar, such as monthly rainfall and temperature, is the correlative analysis applied to the standardized anomalies [30]. This approach also allows for the comparisons of data series of different time periods and lengths [31]. The standardized anomalies of seasonal values of temperature and rainfall were calculated for each site by using their means and standard deviations calculated for the reference period 1961–1990. In this way, the origin of the temperature versus precipitation plots shown in this study corresponds to the mean values of this reference time span, while the anomalies of the two variables extend over the four quadrants of the plot. Specifically, the peculiar climatic conditions of each quadrant are: warm and wet for the upper right quadrant, cold and wet for the upper left one, cold and dry for the lower left one, and warm and dry for the lower right quadrant.

Previous studies on the long-term cumulated rainfall in the Calabria region indicated a shift towards drier conditions around the year 1980 [32,33]. Thus, in order to search for possible temporal trends, the whole 1951–2010 time interval of the data set was fragmented into two 30-year periods: 1951–1980 and 1981–2010. The normality hypothesis was separately tested for both the variables and the 30-year periods by means of the Anderson–Darling test [34]. This is a goodness-of-fit test specially devised to give heavier weights to the distribution tails (where outliers are sometimes located) than the Kolmogorov–Smirnov test.

Only in the cases where the normality hypothesis was not rejected, the correlation analysis has been successively performed. In particular, a bivariate Gaussian distribution was applied to the seasonal variables in each site for the two 30-year periods separately. The probability density function of this distribution can be visualized as isocontour lines in the temperature–rainfall ( $T$ – $R$ ) plane with prefixed significance levels  $\alpha_i$ . These lines are  $(1 - \alpha_i)\%$  confidence ellipses centered on the mean values of the variables. In this study, the significance level has been fixed as equal to 0.05, thus characterizing each correlation by means of a 95% confidence ellipse, which is oriented according to the sign of its correlation coefficient [31].

Each ellipse can be described through the vector of the means and the variance–covariance matrix, while its eigenvectors provide the directions of its major and minor axes. If the variables show changes between the two subperiods, the results are displacements of the ellipses in the  $T$ – $R$  plane, generally formed by rigid transformations (translations and/or rotations) and deformations of the ellipses. Specifically, the translation concerns a modification in the means vector of the ellipses, and the rotation is due to variations in the correlation coefficients, while the deformation is linked to a change in the variance–covariance matrix.

All these cases can be verified through the application of specific statistical tests. In particular, the global statistical significance of the change in the means vector ( $\Delta\bar{T}$ ,  $\Delta\bar{R}$ ) can be assessed through the multivariate Hotelling’s test [35], while the statistical significance of the change of each single value of the vector can be verified by means of the univariate  $t$ -test of difference in the mean [30].

Concerning the orientation of the ellipses, the statistical significance of the difference in the correlation coefficients passing from a subperiod to the other one can be tested by preliminarily transforming each correlation coefficient between the seasonal temperature and the rainfall anomalies,  $\rho$ , into  $z$  score through the Fisher  $Z$ -transformation [30]:

$$Z = \frac{1}{2} \ln \left( \frac{1 + \rho}{1 - \rho} \right). \quad (1)$$

In this way, firstly, the  $Z$  value obtained for each subperiod can be used to test the significance of its correlation coefficient, given that  $Z$  is approximately distributed as a normal law with  $\mu = 0$  and  $\sigma = (N - 3)^{-0.5}$ , where  $N$  is the length of the anomalies series. Then, the difference in the correlation coefficients can be tested through the bivariate test statistic:

$$Z_{biv} = \frac{Z_1 - Z_2}{\sqrt{\frac{1}{N_1 - 3} + \frac{1}{N_2 - 3}}}, \quad (2)$$

which combines the  $Z_1$  and  $Z_2$  values evaluated for the correlation coefficients  $\rho_1$  and  $\rho_2$  of the two subperiods 1951–1980 and 1981–2010 with lengths  $N_1$  and  $N_2$ , respectively. The statistical significance of the difference of the ellipses' orientation can be assessed through the statistic  $Z_{bit}$ , which is normally distributed with  $\mu = 0$  and  $\sigma = 1$ . Quantitatively, the change can be expressed as the angle,  $\vartheta$  ( $^\circ$ ), between the directions of the main axes of the ellipses in the two subperiods.

The deformations of the ellipses (variations in shape and/or size) corresponding to the two subperiods can be linked to the difference of the variances of the two variables ( $F$ -test, univariate case). In other terms, the  $F$ -test can be applied to separately consider the variances for seasonal temperature and rainfall in each subperiod. A measure of the ellipse deformation can be related to the change in the axes' length, which can be expressed as a percentage by:

$$\Delta A = 100(\Delta l_1 + \Delta l_2), \quad (3)$$

where  $\Delta l_i$  ( $i = 1, 2$ ) represents the changes in the major and the minor axes of the ellipse, respectively, which are both related to the eigenvalues of the variance–covariance matrix [31]. This value represents in some way the amount of change in the total variability of the seasonal temperature and rainfall. Finally, displacements of the ellipses were visualized and quantified for both the subperiods, looking for changes in the mean values, the correlation coefficients, and the variances of the seasonal temperature and rainfall anomalies.

### 3. Results and Discussion

As a first step of the procedure, the normality hypothesis has been separately verified for each seasonal temperature and rainfall series for both the 30-year periods by means of the Anderson–Darling test [34]. The results obtained for each gauge and 30-year period indicate that the normality hypothesis holds for the 1010 and 930 gauges in three out of four seasons, for the 1180 gauge in two out of three seasons, and for the 1680 gauge only in one (Table 3). Regarding the seasons, the normality hypothesis is fully plausible for winter in all the sites and subperiods. In autumn, the hypothesis is acceptable for three out of four gauges, with the exception of the rainfall of gauge 1680, for both the subperiods. In spring, the normality hypothesis is unacceptable in gauge 1680 for both the variables in 1951–1980, and in gauge 1180 for rainfall in 1981–2010. Concerning the summer, all the gauges show at least one series with a behaviour which is not normally distributed. Globally, a lower number of occurrences of non-normal conditions has been detected in 1951–1980 compared to in 1981–2010.

Based on these results, the seasons and time periods for which the normality conditions have been verified were chosen for the correlation analysis. Specifically, this concerns gauges 930 and 1010 for winter, spring, and autumn, gauge 1180 for winter and autumn, and gauge 1680 for winter only. The correlation analysis procedure has been focused on the 95% confidence ellipses drawn for both the two 30-year periods (Figures 2–4).

In the winter season, decreasing values of the means for both the seasonal temperature and rainfall anomalies have been detected passing from 1951–1980 to 1981–2010 in all the selected gauges, except for a weak increase of the seasonal rainfall of gauge 1680 (Table 4). These results are clearly evidenced by the translations of the centroids of the ellipses (Figure 2a–d). The  $t$ -test, adopted for the verification of these changes in a separate way for  $\Delta \bar{T}$  and  $\Delta \bar{R}$ , provides statistically significant results in six out of eight cases (Table 5). Specifically, the rigid translation of the ellipses proved to be significant for both the winter temperature and rainfall of gauges 930 (with remarkable values of  $-1.5$  and  $-1.0$ , respectively) and 1010, while in the other two gauges, this is only verified by one variable ( $\Delta \bar{R}$  of gauge 1180 and  $\Delta \bar{T}$  of gauge 1680), as shown in Table 4. The statistical significance of the change in the means' vector, jointly assessed by means of the multivariate Hotelling's test, was provided for all the cases, confirming the results obtained through the  $t$ -test (Table 5). The rotation assumes a high significant value for gauge 930 ( $109.1^\circ$ ). The deformations are always not significant, with the highest not-significant increase of 61% observed in gauge 1680 (Table 4).

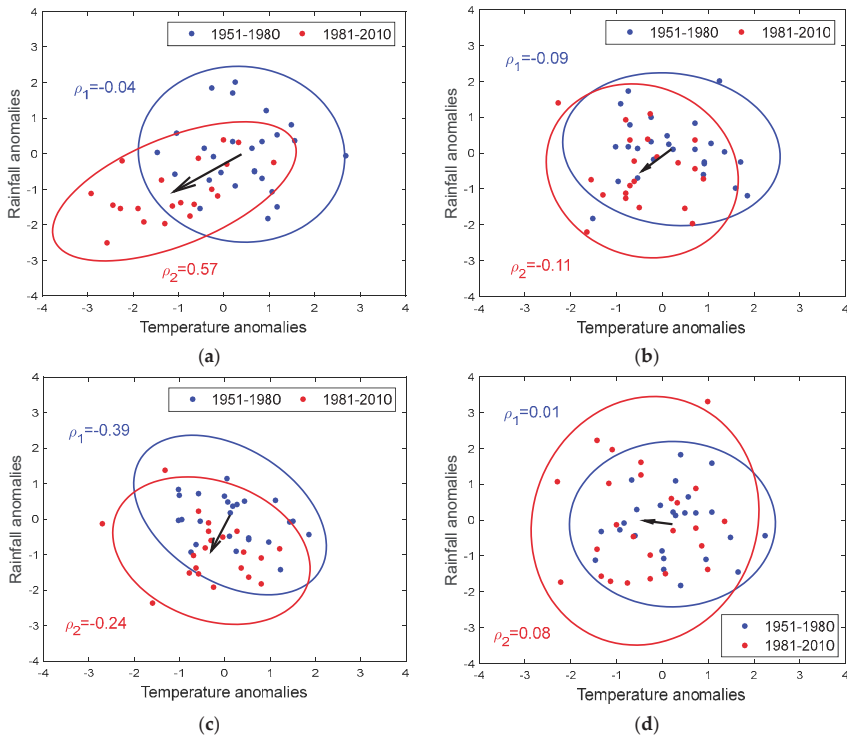


**Figure 2.** The 95% confidence ellipses for the winter season at gauge (a) 930; (b) 1010; (c) 1180; (d) 1680.

In spring, Figure 3a,b shows that both the stations which satisfy the normality hypothesis present decreasing tendencies of temperature and rainfall anomalies, but only gauge 930 (Figure 3a) evidences a significant clear negative tendency ( $-0.8$ ) of the temperature anomalies (Table 4). The Hotelling's test is verified in spring only for gauge 930, and the  $t$ -test is verified for the same gauge only for the temperature anomalies. For the rotations, the only significant value has been observed at gauge 930 ( $69.2^\circ$ ), while not-significant values were detected regarding the deformations.

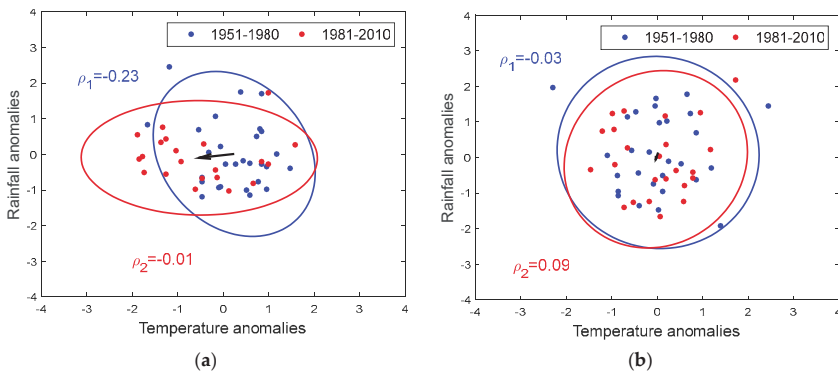


**Figure 3.** The 95% confidence ellipses for the spring season at gauge (a) 930; (b) 1010.

In autumn (Figure 4a–c), notable statistically significant decreasing values (Table 4) have been observed. In particular, gauge 930 (Figure 4a) evidences a more pronounced significant negative tendency for the mean temperature anomalies than for the rainfall ones ( $-0.8$  and  $-0.6$  for the temperature and the rainfall anomalies, respectively), as detected through the  $t$ -test. Gauge 1180 presents the only significant value only for the rainfall anomalies ( $-0.8$ ). These results have been statistically proved also by means of the multivariate Hotelling’s test (Table 5). Not-significant values were observed for the rotations, and the only significant value of deformation has been detected at gauge 930 ( $-59\%$ ).

**Table 3.** Anderson–Darling statistic for temperature and rainfall series. Critical values for different N have been assumed at the 95% confidence level. (The cases in which the normality hypothesis is rejected are in bold italics.)

Season	Gauges	1951–1980		1981–2010	
		Temperature	Rainfall	Temperature	Rainfall
Winter	930	0.229	0.249	0.189	0.473
	1010	0.474	0.325	0.425	0.196
	1180	0.472	0.707	0.392	0.224
	1680	0.249	0.279	0.279	0.443
Spring	930	0.673	0.490	0.490	0.309
	1010	0.349	0.477	0.257	0.321
	1180	0.303	0.305	0.387	<b>0.807</b>
	1680	<b>0.790</b>	<b>0.899</b>	0.261	0.218
Summer	930	0.216	0.406	<b>1.047</b>	<b>0.791</b>
	1010	0.264	0.351	0.309	<b>1.154</b>
	1180	0.321	<b>1.229</b>	0.576	0.448
	1680	0.428	<b>2.053</b>	<b>1.027</b>	<b>1.240</b>
Autumn	930	0.344	0.491	0.338	0.434
	1010	0.242	0.276	0.442	0.223
	1180	0.351	0.196	0.405	0.695
	1680	0.346	<b>1.015</b>	0.190	<b>0.863</b>

**Table 4.** Displacements of the 95% contour ellipses corresponding to each station and variable passing from 1951–1980 to 1981–2010. (Statistically significant results at 95% confidence level are in bold italics.)

Season	Site	Translations		Rotations	Deformations
		$\Delta\bar{T}$	$\Delta\bar{R}$	$\vartheta$ (°)	$\Delta A$ (%)
Winter	930	<b><i>-1.5</i></b>	<b><i>-1.0</i></b>	<b><i>109.1</i></b>	-16
	1010	<b><i>-0.6</i></b>	<b><i>-0.6</i></b>	-51.4	0
	1180	-0.4	<b><i>-1.0</i></b>	9.5	1
	1680	<b><i>-0.6</i></b>	+0.1	1.8	61
Spring	930	<b><i>-0.8</i></b>	-0.1	<b><i>69.2</i></b>	4
	1010	-0.1	-0.2	-14.9	-17
Autumn	930	<b><i>-0.8</i></b>	<b><i>-0.6</i></b>	43.5	<b><i>-59</i></b>
	1010	-0.2	-0.1	13.5	-36
	1180	-0.3	<b><i>-0.8</i></b>	<b><i>-42.8</i></b>	-27

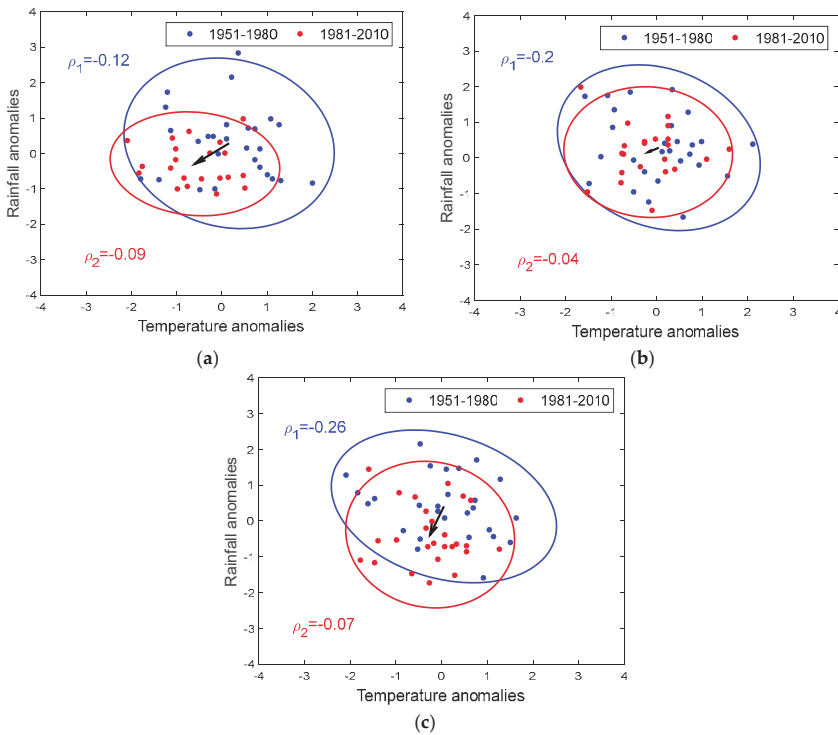


**Figure 4.** The 95% confidence ellipses for the autumn season at gauge (a) 930; (b) 1010; (c) 1180.

**Table 5.** Testing results of the change in the means of the seasonal values of temperature ( $T$ ) and rainfall ( $R$ ) observed in 1951–1980 and 1981–2010. ( $H$ , Hotelling's test;  $t(T)$  and  $t(R)$ , two-sample  $t$ -test. Statistically significant results at the 95% confidence level are in bold italics.)

Season	Site	$H$	$t(T)$	$t(R)$
Winter	930	<b>30.28</b>	<b>-4.84</b>	<b>-3.91</b>
	1010	<b>11.66</b>	<b>-2.39</b>	<b>-2.19</b>
	1180	<b>23.77</b>	-1.59	<b>-3.88</b>
	1680	<b>4.91</b>	<b>-2.18</b>	+0.28
Spring	930	<b>8.70</b>	<b>-2.85</b>	-0.48
	1010	0.46	-0.21	-0.65
Autumn	930	<b>17.39</b>	<b>-3.05</b>	<b>-2.51</b>
	1010	1.37	-0.98	-0.51
	1180	<b>14.78</b>	-1.24	<b>-3.36</b>

#### 4. Conclusions

The variabilities of the seasonal temperature and rainfall observed in four sites located in Calabria (Southern Italy) have been jointly investigated by means of the analysis of the variations in the 95% confidence ellipses of the bivariate normal distribution, evaluated for two different 30-year periods. The values of the various displacements (translations, rotations, and deformations) detected for the ellipses, estimated passing from the first subperiod to the second one, have been presented. Though this study is limited to a few gauges, the joint variations of the two climatic variables show the same tendencies in most of the considered cases. The results confirm the general negative

trend detected for both monthly temperature and rainfall in Southern Italy, detected in previous studies [14,33]. Moreover, the tendency detected for seasonal rainfall confirms the general trend of long-term cumulated precipitation in the Mediterranean area [6,24]. On the contrary, the results here obtained for temperature evidenced that global warming, also revealed in the Mediterranean and the Middle East [24], is not always observed everywhere and in each season of the year, because opposite trends linked to specific local features can be detected, as already evidenced in Calabria by Caloiero et al. [23]. Moreover, it is important to highlight that when the comparison is carried out on results based on datasets with substantial differences, only limited conclusions about trends can be drawn. Nevertheless, even if the obtained results in terms of the joint gradients of rainfall and temperature statistics cannot be used to predict their relationships, because no assessment about the stationarity of the results was carried out, the trends observed, if confirmed in the future, could have potential impacts on several environmental sectors, in particular on agriculture.

**Author Contributions:** Conceptualization, E.F., R.C. and B.S.; Methodology, Software and Validation, E.F., R.C. and B.S.; Formal Analysis and Investigation, E.F. and R.C.; Writing-Review & Editing, E.F. and R.C.

## References

1. Calderini, D.F.; Abeledo, L.G.; Savin, R.; Slafer, G.A. Effect of temperature and carpel size during pre-anthesis on potential grain weight in wheat. *J. Agric. Sci.* **1999**, *132*, 453–459. [CrossRef]
2. Abbate, P.E.; Dardanelli, J.L.; Cantarero, M.G.; Maturano, M.; Melchiori, R.J.M.; Suero, E.E. Climatic and water availability effects on water-use efficiency in wheat. *Crop Sci.* **2004**, *44*, 474–483. [CrossRef]
3. Medori, M.; Michelini, L.; Nogue, I.; Loreto, F.; Calfapietra, C. The impact of root temperature on photosynthesis and isoprene emission in three different plant species. *Sci. World J.* **2012**. [CrossRef] [PubMed]
4. Caloiero, T. Analysis of rainfall trend in New Zealand. *Environ. Earth Sci.* **2015**, *73*, 6297–6310. [CrossRef]
5. Brunetti, M.; Caloiero, T.; Coscarelli, R.; Gullà, G.; Nanni, T.; Simolo, C. Precipitation variability and change in the Calabria region (Italy) from a high resolution daily dataset. *Int. J. Climatol.* **2012**, *32*, 57–73. [CrossRef]
6. Longobardi, A.; Buttafuoco, G.; Caloiero, T.; Coscarelli, R. Spatial and temporal distribution of precipitation in a Mediterranean area (Southern Italy). *Environ. Earth Sci.* **2016**, *75*, 189. [CrossRef]
7. Mehta, A.V.; Yang, S. Precipitation climatology over Mediterranean Basin from ten years of TRMM measurements. *Adv. Geosci.* **2008**, *17*, 87–91. [CrossRef]
8. Reale, M.; Lionello, P. Synoptic climatology of winter intense precipitation events along the Mediterranean coasts. *Nat. Hazards Earth Syst.* **2013**, *13*, 1707–1722. [CrossRef]
9. Lionello, P.; Giorgi, F. Winter precipitation and cyclones in the Mediterranean region: Future climate scenarios in a regional simulation. *Adv. Geosci.* **2007**, *12*, 153–158. [CrossRef]
10. Brunetti, M.; Maugeri, M.; Monti, F.; Nanni, T. Temperature and precipitation variability in Italy in the last two centuries from homogenised instrumental time series. *Int. J. Climatol.* **2006**, *26*, 345–381. [CrossRef]
11. Longobardi, A.; Villani, P. Trend analysis of annual and seasonal rainfall time series in the Mediterranean area. *Int. J. Climatol.* **2010**, *30*, 1538–1546. [CrossRef]
12. Piccarreta, M.; Capolongo, D.; Boenzi, F. Trend analysis of precipitation and drought in Basilicata from 1923 to 2000 within a Southern Italy context. *Int. J. Climatol.* **2004**, *24*, 907–922. [CrossRef]
13. Liuzzo, L.; Bono, E.; Sammartano, V.; Freni, G. Analysis of spatial and temporal rainfall trends in Sicily during the 1921–2012 period. *Theor. Appl. Climatol.* **2016**, *126*, 113–129. [CrossRef]
14. Caloiero, T.; Buttafuoco, G.; Coscarelli, R.; Ferrari, E. Spatial and temporal characterization of climate at regional scale using homogeneous monthly precipitation and air temperature data: An application in Calabria (southern Italy). *Hydrol. Res.* **2015**, *46*, 629–646. [CrossRef]
15. Klok, E.J.; Tank, A. Updated and extended European dataset of daily climate observations. *Int. J. Climatol.* **2009**, *29*, 1182–1191. [CrossRef]
16. Caloiero, T.; Callegari, G.; Cantasano, N.; Coletta, V.; Pellicone, G.; Veltri, A. Bioclimatic Analysis in a Region of Southern Italy (Calabria). *Plant Biosyst.* **2015**. [CrossRef]
17. Liang, K.; Bai, P.; Li, J.J.; Liu, C.M. Variability of temperature extremes in the Yellow River basin during 1961–2011. *Quat. Int.* **2014**, *336*, 52–64. [CrossRef]

18. Caloiero, T. Trend of monthly temperature and daily extreme temperature during 1951–2012 in New Zealand. *Theor. Appl. Climatol.* **2016**. [CrossRef]
19. Salinger, M.J.; Griffiths, G.M. Trends in New Zealand daily temperature and rainfall extremes. *Int. J. Climatol.* **2001**, *21*, 1437–1452. [CrossRef]
20. Donat, M.G.; Alexander, L.V. The shifting probability distribution of global daytime and night-time temperatures. *Geophys. Res. Lett.* **2012**, *39*, L14707. [CrossRef]
21. Giorgi, F. Climate change hot-spots. *Geophys. Res. Lett.* **2006**, *33*, L08707. [CrossRef]
22. Simolo, C.; Brunetti, M.; Maugeri, M.; Nanni, T.; Speranza, A. Understanding climate change-induced variations in daily temperature distributions over Italy. *J. Geophys. Res.* **2010**, *115*, D22110. [CrossRef]
23. Caloiero, T.; Coscarelli, R.; Ferrari, E.; Sirangelo, B. Trend analysis of monthly mean values and extreme indices of daily temperature in a region of southern Italy. *Int. J. Climatol.* **2017**, *37*, 284–297. [CrossRef]
24. Tanarhte, M.; Hadjinicolaou, P.; Lelieveld, J. Intercomparison of temperature and precipitation data sets based on observations in the Mediterranean and the Middle East. *J. Geophys. Res.* **2012**, *117*. [CrossRef]
25. Rajeevan, M.; Pai, D.S.; Thapliyal, V. Spatial and temporal relationships between global land surface air temperature anomalies and Indian summer monsoon rainfall. *Meteorol. Atmos. Phys.* **1998**, *66*, 157–171. [CrossRef]
26. Huang, Y.; Cai, J.; Yin, H.; Cai, M. Correlation of precipitation to temperature variation in the Huanghe River (Yellow River) basin during 1957–2006. *J. Hydrol.* **2009**, *372*, 1–8. [CrossRef]
27. Cong, R.G.; Brady, M. The Interdependence between Rainfall and Temperature: Copula Analyses. *Sci. World J.* **2012**. [CrossRef] [PubMed]
28. Péguy, C.P. Une tentative de délimitation et de schématisation des climats intertropicaux. *Rev. Geogr.* **1961**, *36*, 1–6. [CrossRef]
29. Craddock, J.M. Methods of comparing annual rainfall records for climatic purposes. *Weather* **1979**, *34*, 332–346. [CrossRef]
30. Wilks, D.S. *Statistical Methods in the Atmospheric Sciences*, 2nd ed.; International Geophysics Series; Academic Press: Cambridge, MA, USA, 1995.
31. Rodrigo, F.S. On the covariability of seasonal temperature and precipitation in Spain, 1956–2005. *Int. J. Climatol.* **2014**, *35*, 3362–3370. [CrossRef]
32. Sirangelo, B.; Ferrari, E. Probabilistic analysis of the variation of water resources availability due to rainfall change in the Crati basin (Italy). In *Global Change: Facing Risks and Threats to Water Resources*; Servat, E., Demuth, S., Dezetter, A., Daniell, T., Ferrari, E., Ijjaali, M., Jabrane, R., van Lanen, H., Huang, Y., Eds.; IAHS Publication, N° 340; IAHS Press: Wallingford, UK, 2010; pp. 142–149.
33. Ferrari, E.; Terranova, O. Non-parametric detection of trends and change point years in monthly and annual rainfalls. In Proceedings of the 1st Italian-Russian Workshop on New Trend in Hydrology, CNR-IRPI, Rende, Italy, 24–26 September 2002; pp. 177–188.
34. Kottegoda, N.T.; Rosso, R. *Applied Statistics for Civil and Environmental Engineers*, 2nd ed.; Wiley & Sons: New York, NY, USA, 2008.
35. Hotelling, H. The generalization of Student's ratio. *Ann. Math. Stat.* **1931**, *2*, 360–378. [CrossRef]

# An Attempt to Use Non-Linear Regression Modelling Technique in Long-Term Seasonal Rainfall Forecasting for Australian Capital Territory

Iqbal Hossain \*, Rijwana Esha and Monzur Alam Imteaz

Faculty of Science, Engineering & Technology, Swinburne University of Technology, Melbourne, Hawthorn VIC 3122, Australia; resha@swin.edu.au (R.E.); mimteaz@swin.edu.au (M.A.I.)

\* Correspondence: ihossain@swin.edu.au

**Abstract:** The objective of this research is the assessment of the efficiency of a non-linear regression technique in predicting long-term seasonal rainfall. The non-linear models were developed using the lagged (past) values of the climate drivers, which have a significant correlation with rainfall. More specifically, the capabilities of SEIO (South-eastern Indian Ocean) and ENSO (El Nino Southern Oscillation) were assessed in reproducing the rainfall characteristics using the non-linear regression approach. The non-linear models developed were tested using the individual data sets, which were not used during the calibration of the models. The models were assessed using the commonly used statistical parameters, such as Pearson correlations (R), root mean square error (RMSE), mean absolute error (MAE) and index of agreement (d). Three rainfall stations located in the Australian Capital Territory (ACT) were selected as a case study. The analysis suggests that the predictors which has the highest correlation with the predictands do not necessarily produce the least errors in rainfall forecasting. The non-linear regression was able to predict seasonal rainfall with correlation coefficients varying from 0.71 to 0.91. The outcomes of the analysis will help the watershed management authorities to adopt efficient modelling technique by predicting long-term seasonal rainfall.

**Keywords:** non-linear model; seasonal rainfall; climate drivers; SEIO, ENSO; rainfall prediction

---

## 1. Introduction

Rainfall can be regarded as the most important climate element in the hydrological cycle that has considerable effects on the surrounding environment, including human lives. The spatial and temporal distribution of rainfall has significant impact on the water availability of earth surfaces, and hence on the agricultural activities. Since the agricultural activities and resulting crop production depends on the distribution of rainfall, prediction of monthly and seasonal rainfall is essentially important for the agricultural planning, flood mitigation strategies. However, accurate prediction of seasonal rainfall remains elusive to the scientists. Therefore, seasonal rainfall forecasting becomes plausible amongst the hydrologic researchers around the globe [1,2].

Seasonal forecasting can be classified into two broad categories: the statistical approach and the dynamic approach. In the statistical approach, the statistical relationships between the predictors and the predictands are investigated [3]. In the dynamic approach, seasonal meteorological estimates are used to build a hydrological model. However, there are methodological implications in using meteorological inputs in the current hydrological models [4]. The climate model produces the outputs based on coarse grid scales, which has the potential to capture forecasting uncertainties, and hence lead to bias. Furthermore, the data requirements of the dynamic models hinder the application of the modelling type. As a result, the statistical approach drew considerable attention to the practical users of the prediction models.

Long-term prediction of seasonal rainfall has the potential to help in the decision-making process for planning appropriate watershed management strategies [4]. Moreover, advanced prediction of rainfall can provide information to adopt the consequences of climate change [5]. As a result, the urge for the application of seasonal rainfall forecasting is increasing day by day. Therefore, seasonal forecasting is routinely performed by different research institutes, to have better understanding of climate change throughout the world. However, there exist limiting factors which act as the barriers for the wider application of the seasonal prediction models [6]. For example, the seasonal predictions are affected by the predictors, predictands, region and season [7]. Nevertheless, the chaotic dynamics of the atmosphere may lead to the erroneous prediction of seasonal rainfall [8]. The uncertainties in the model parameterization further hinder the prediction of seasonal rainfall.

Till today, precipitation is the most challenging climatic phenomena, which can be predicted with least accuracy [7]. On the other hand, most of the research studies on precipitation prediction have been conducted over a regional area of the world and in a particular season [9–12]. There exist only a few studies that concentrate on the precipitation analysis of the whole world [7,8,13]. Most of the studies conducted used number of various scores to evaluate predicted rainfall with the observed rainfall, such as, correlations, ranked probability score and Brier skill score. However, there is still doubt regarding the accuracy of the predictions of the seasonal models, which has immense implications in the decision-making process [14]. Nevertheless, there exists overconfidence and lack of reliability in the prediction of seasonal rainfall using the currently available models [15]. Therefore, it is necessary to assess the comprehensive performance of different models and their uncertainties in predicting seasonal rainfall.

It is well established that large-scale atmospheric circulation patterns significantly affect the annual precipitation around the globe including Australia. The atmospheric circulation configuration is dominated by the patterns of the sea surface temperature. Many researchers accept the capability of the El Nino Southern Oscillation (ENSO) in predicting time-series events. After analysing the role of ENSO on seasonal precipitation, Manzanos et al. [13] found that September to October is the most skillful season to predict rainfall around eastern Australia. Hossain et al. [9]; Hossain et al. [16] also identified the effects of ENSO and Indian Ocean Dipole (IOD) on West Australian rainfall. Therefore, the evaluation of the ENSO capability in time-series prediction is the fundamental requirement. Other climatic variables, such as sea surface temperature over the Atlantic and Indian Ocean have considerable impacts on the climate variability near the surrounding regions [17]. Recent studies also suggested that Indian Ocean Dipole (IOD) has the considerable effects on the climate variability in the continental regions including Australia [18,19]. Rasel et al. [20] revealed the effects of Southern Annular Mode (SAM) as a potential contributor of South Australian rainfall variability.

A number of studies have been examined to identify appropriate modelling technique for the prediction of seasonal rainfall. However, only a single climate driver is not capable of replicating the accurate precipitation characteristics. Multi-predictors models have the higher prediction skill than the single predictor models [21]. Nevertheless, there may exist dissimilar characteristics of seasonal rainfall patterns with the same rainfall totals [1]. On the other hand, there exist non-linear characteristics of the seasonal climate [8]. Therefore, a closer look at the appropriate mechanism of seasonal rainfall formation becomes essentially important.

This paper presents the efficiency of non-linear regression modelling technique in predicting long-term seasonal rainfall forecasting. The non-linear analysis was performed using the lagged (past) values of the climate indices as the potential predictors of long-term seasonal rainfall. Since there exist significant correlations between seasonal rainfall and two to three months average values of the climate indices, lagged values of the predictors were considered in this research. Furthermore, many researchers identified the ENSO and IOD as the most significant predictors of Australian seasonal rainfall. In this research, the efficiency of the climate indices in rainfall forecasting were assessed using the non-linear regression analysis technique. The non-linear analysis was performed considering South-eastern Indian Ocean (SEIO), Nino3.4 (sea surface temperature anomalies from 5° S to 5° N and

170° W to 120° W), southern oscillation index (SOI) and dipole model index (DMI) as the significant influential parameters of seasonal rainfall variation. The analysis was performed and applied to three rainfall stations in Australian Capital Territory (ACT). Seasonal rainfall forecasting can have practical implications to a wide range of users in diverse sectors, such as agriculture, energy, water supply and stormwater management [22]. The outcomes of the analysis may be the benchmark for future generations in predicting seasonal rainfall.

**2. Study Area and Data Collection**

The Australian Capital Territory (ACT) located in the south-east of the country is enclaved within the state of New South Wales (NSW). Unlike other Australian cities whose climates are moderated by the sea, the ACT experiences four distinct seasons. As a result, the inter-annual variation of precipitation in the ACT is higher. Annually, the ACT receives approximately 623 mm rainfall. The highest rainfall could be observed in spring and summer and the lowest in winter. This study concentrates on the application of non-linear regression modelling technique in the ACT for the prediction of long-term seasonal rainfall. The non-linear models were developed using the large-scale climate drivers. Therefore, the research requires both long-term rainfall data and climate indices data.

In Australia, the Bureau of Meteorology (BoM) collects and stores rainfall data from more than 2000 stations. For the achievement of the objectives of this paper, three rainfall stations located in the ACT were selected as a case study. Specific location of the rainfall stations is shown in Figure 1.

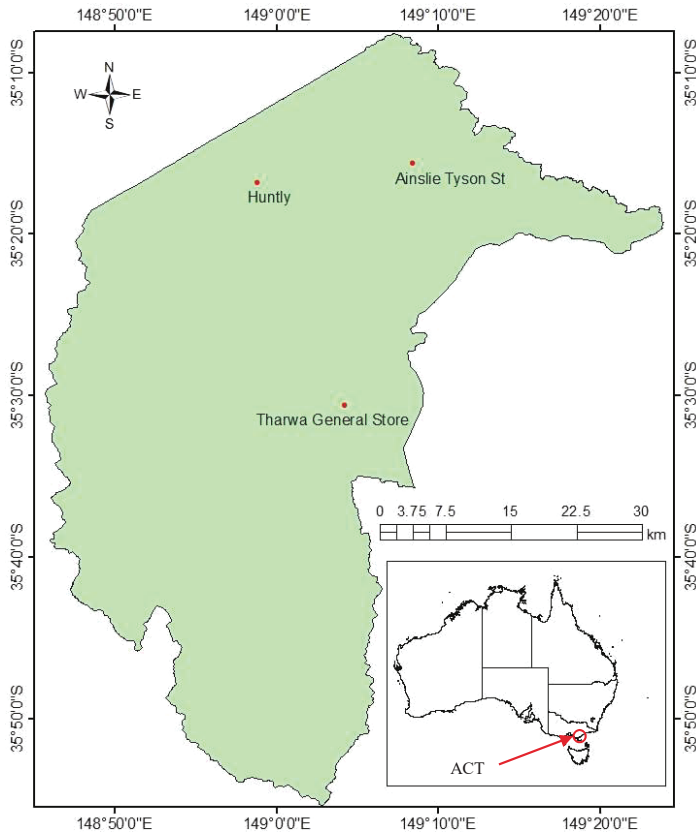


**Figure 1.** Selected rainfall stations in Australian Capital Territory.

Long-term monthly rainfall data from 1971 to 2017 were downloaded from Australian Bureau of Meteorology (<http://www.bom.gov.au/climate/data/?ref=ftr>). The rainfall stations were selected based on the availability of long-term data which have fewer missing values. Monthly variation of the rainfall for the selected rainfall stations throughout the study period is shown in Figure 2. The long-term variation of the same rainfall could be seen in Figure 3 (blue curve). Seasonal rainfall was estimated from the collected monthly rainfall data. In this paper, the average of the spring (September-October-November) rainfall data were used to perform non-linear regression analysis. The data collected were used not only to construct the non-linear regression models but also to validate the prediction capability of the developed models.

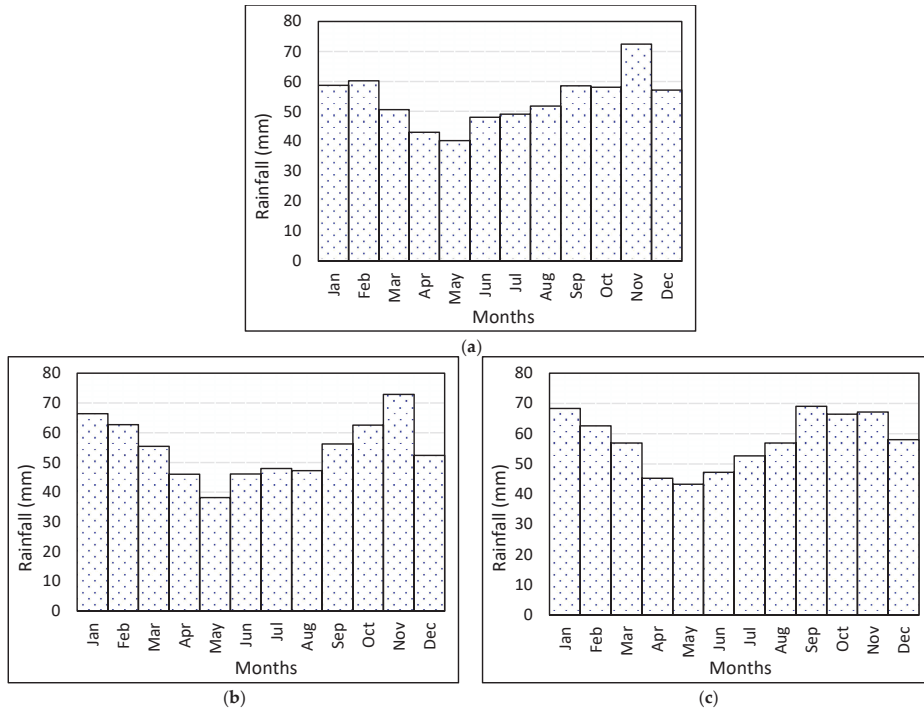


**Figure 2.** Monthly variations of rainfalls for the selected stations throughout the study period. (a) Ainslie Tyson St; (b) Tharwa General Store; (c) Huntly.

To replicate the appropriate characteristics of seasonal rainfall, it is required to identify which month's climate indices should be used in the analysis. Since the main focus of this paper is the efficiency of non-linear regression modelling technique in predicting long-term seasonal rainfall, the climate indices which have a significant correlation with rainfall were analysed and used for the construction of the non-linear models. Monthly values of the long-term climate indices data from 1971 to 2017 were collected from the climate explorer website (<https://climexp.knmi.nl/start.cgi>). Monthly values of the SEIO, Nino3.4, SOI and DMI were downloaded to achieve the objective of this research. In this paper, 90% of the data were used to construct the non-linear models and 10% of the data were used to assess the performance of the constructed models.

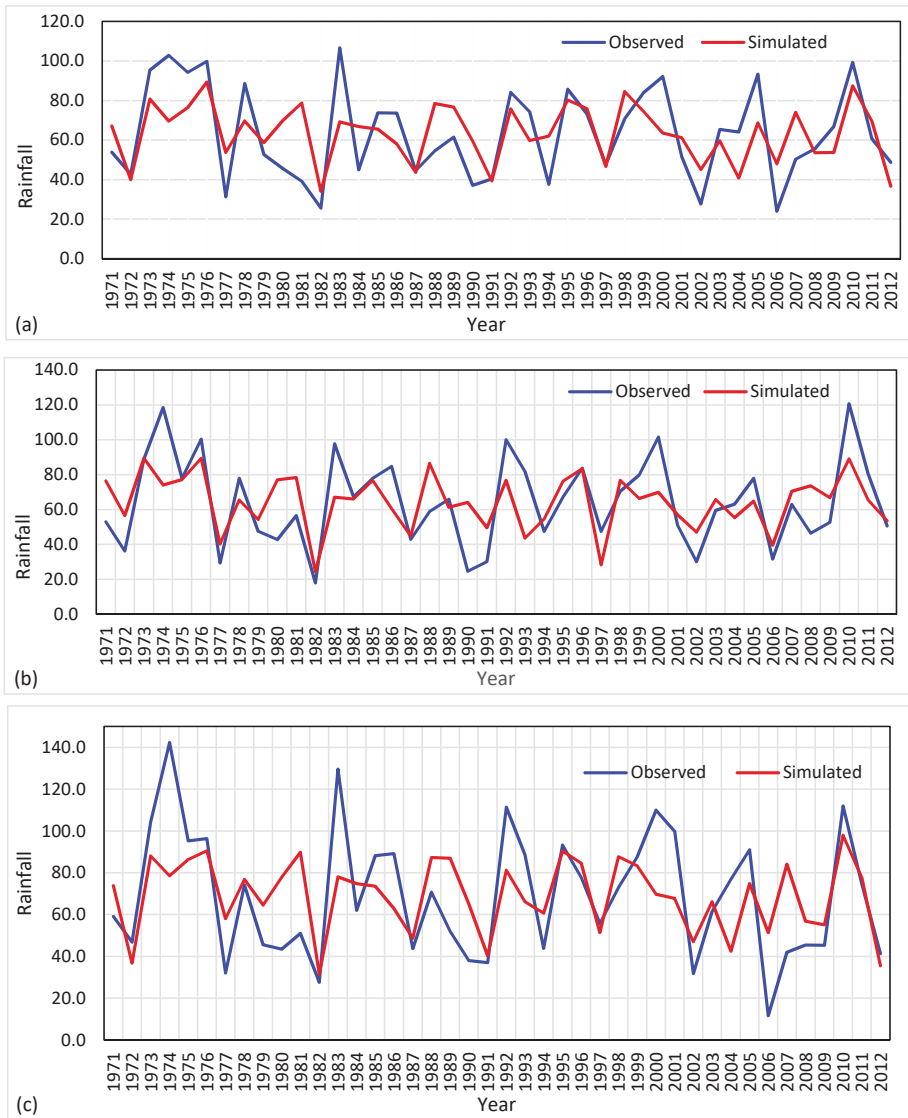


**Figure 3.** Comparison of the modelling output during the calibration period. (a) Ainslie Tyson St; (b) Tharwa General Store; (c) Huntly.

**3. Methods**

Traditional exploration of the relationship between two or more parameters are obtained by statistical regression analysis. In this study, non-linear regression analysis was performed to obtain steady relationship between long-term seasonal rainfall and large scale climate indices. In the non-linear regression technique, the arbitrary relationship between the predictands and predictors are obtained. One or more independent variables dictate the determination of non-linear relationship

amongst the model parameters [23]. The general relationship of the non-linear regression can be explained according to Equation (1) [24]:

$$Y = b_1X_i + b_2X_j + b_3X_i^2 + b_4X_j^2 + \dots + b_nX_iX_j + e \quad (1)$$

where,  $Y$  is the dependent variable;  $b_1, b_2, \dots, b_n$  are coefficients of the independent variables;  $n$  is the number of observations;  $X$  is the independent variables and  $e$  is model error. The fitted model has the potential to predict the value of  $Y$  for the additional observed values of  $X$ .

There may exist different non-linear functions which is suitable to replicate the appropriate rainfall pattern. To find out the suitable predicting model for streamflow, researchers have performed a series of simple regression analysis [25]. To recommend a suitable seasonal rainfall predicting model, six different functions: linear, quadratic, cubic, exponential, power and logarithmic were assessed in this study. The function which has the higher Pearson correlation with the rainfall was considered as the potential model for rainfall prediction. The long-term seasonal rainfall data were used for the estimation of the correlations. The predictions may be penalized due to the lack of understanding of the physical processes. The interactions amongst the sub-processes of the variables may further hinder the predictive capability [26]. Therefore, individual correlations amongst the climate indices were performed to assess the significant correlations. The climate indices which have significant correlation amongst themselves were not used to develop the non-linear regression models.

Since the forecast verification assesses the capability of re-producing the observed data, the process is considered as an essential process of any model development [27]. In this research, the assessment of the forecast quality of the developed non-linear regression models were performed using the commonly used statistical errors, Pearson correlations, root mean square error (RMSE), mean absolute error (MAE) and index of agreement (d). The regression model which has the highest correlation between the seasonal rainfall and combined indices during the validation period (2013–2017) was considered as the recommended predictor model.

#### 4. Results and Discussion

From the available linear and non-linear functions, the Pearson correlations between the climate indices and the ACT spring rainfall was determined from the fitted data sets. The function which has the higher correlation was considered as the suitable model for rainfall prediction. The correlations of the regression analysis is shown in Tables 1–3 for Ainslie Tyson St, Tharwa General Store and Huntly rainfall stations respectively. The month shown in the subscript is the value of the corresponding climate index for the specified month. The star (\*) in the table refers that the correlation is significant at the 0.05 level.

**Table 1.** Pearson correlations of the regression analysis for Ainslie Tyson St station.

Index	Linear	Quadratic	Cubic	Exponential	Power	Logarithmic
DMI <sub>Jun</sub>	0.083	0.097	0.154	0.082	0.182	0.187
NINO3.4 <sub>Jun</sub>	0.420 *	0.428 *	0.436 *	0.411 *	0.153	0.157
NINO3.4 <sub>Jul</sub>	0.462 *	0.462 *	0.495 *	0.456 *	0.056	0.061
NINO3.4 <sub>Aug</sub>	0.503 *	0.503 *	0.524 *	0.499 *	0.332	0.338
SEIO <sub>Jun</sub>	0.127	0.265	0.267	0.135	0.331	0.312
SEIO <sub>Jul</sub>	0.208	0.280	0.323 *	0.218	0.305	0.309
SEIO <sub>Aug</sub>	0.236	0.242	0.243	0.232	0.099	0.098
SOI <sub>Jun</sub>	0.380 *	0.385 *	0.389 *	0.374 *	-0.055	0.071
SOI <sub>Jul</sub>	0.407 *	0.407 *	0.470 *	0.405 *	0.451	0.242
SOI <sub>Aug</sub>	0.502 *	0.517 *	0.527 *	0.488 *	0.002	0.002

**Table 2.** Pearson correlations of the regression analysis for Tharwa General Store station.

Index	Linear	Quadratic	Cubic	Exponential	Power	Logarithmic
DMI <sub>Jun</sub>	0.193	0.198	0.226	0.190	0.183	0.192
NINO3.4 <sub>Jun</sub>	0.457 *	0.480 *	0.507 *	0.440 *	0.232	0.240
NINO3.4 <sub>Jul</sub>	0.518 *	0.519 *	0.573 *	0.508 *	0.089	0.099
NINO3.4 <sub>Aug</sub>	0.542 *	0.542 *	0.589 *	0.533 *	0.298	0.303
SEIO <sub>Jun</sub>	0.152	0.325 *	0.329 *	0.166	0.279	0.246
SEIO <sub>Jul</sub>	0.195	0.253	0.301 *	0.204	0.226	0.230
SEIO <sub>Aug</sub>	0.218	0.222	0.231	0.214	0.022	0.022
SOI <sub>Jun</sub>	0.350 *	0.355 *	0.355 *	0.344 *	0.042	0.159
SOI <sub>Jul</sub>	0.407 *	0.407 *	0.472 *	0.407 *	0.518 *	0.376
SOI <sub>Aug</sub>	0.516 *	0.532 *	0.532 *	0.500 *	0.071	0.070

**Table 3.** Pearson correlations of the regression analysis for Huntly station.

Index	Linear	Quadratic	Cubic	Exponential	Power	Logarithmic
DMI <sub>Jun</sub>	0.122	0.122	0.151	0.121	0.105	0.109
NINO3.4 <sub>Jun</sub>	0.383 *	0.387 *	0.391 *	0.376 *	0.288	0.283
NINO3.4 <sub>Jul</sub>	0.450 *	0.451 *	0.474 *	0.448 *	0.161	0.176
NINO3.4 <sub>Aug</sub>	0.476 *	0.476 *	0.510 *	0.476 *	0.375	0.380
SEIO <sub>Jun</sub>	0.136	0.260	0.280	0.136	0.268	0.246
SEIO <sub>Jul</sub>	0.216	0.235	0.280	0.221	0.231	0.236
SEIO <sub>Aug</sub>	0.248	0.258	0.274	0.241	0.076	0.076
SOI <sub>Jun</sub>	0.267	0.274	0.274	0.262	-0.097	0.019
SOI <sub>Jul</sub>	0.322 *	0.322 *	0.399 *	0.321 *	0.495 *	0.320
SOI <sub>Aug</sub>	0.467 *	0.477 *	0.478 *	0.453 *	0.011	0.010

For Ainslie Tyson St rainfall station, the cubic function has the maximum correlations between spring rainfall and all the climate indices except SEIO<sub>Jun</sub>. This climate index has the maximum correlation with power function as shown in Table 1. Similarly for Huntly rainfall station, the cubic function has the maximum correlations between spring rainfall and the climate indices except SOI<sub>Jul</sub>. As evidenced in Table 2, power function has the maximum correlation with rainfall and this predictor. However for Tharwa General Store rainfall station, cubic function has the maximum correlations between spring rainfall and all the climate indices as can be seen in Table 3. Generally, the cubic function is the best predictor and the logarithmic function is the least predictor for seasonal rainfall forecasting. A similar outcome was obtained by Esha and Imteaz [25] in predicting streamflow.

To develop a generalised non-linear model for the prediction of seasonal rainfall, the functions which have the maximum correlation were further analysed. Seventeen combined non-linear models were developed for each of the rainfall stations. The arrangement was selected in such a way that there is no significant correlation amongst the input combinations. The correlation coefficients for each of the developed models were also estimated. The combined indices that have been used to construct the non-linear regression models and their correlations are shown in Table 4 for all the selected three rainfall stations.

It is clear from Table 4 that only single model is not capable to predict seasonal rainfall with sufficient accuracy for all the rainfall stations. The table reveals that DMI-SOI based models are appropriate for predicting seasonal rainfall with maximum correlation 0.71. However, the appropriate combination is not in the same month for all the stations. For instance, DMI<sub>Jun</sub> influence is dominant for all the three stations, whereas associated dominant indices are; SOI<sub>Jul</sub> for Tharwa General Store station and SOI<sub>Aug</sub> for Ainslie Tyson St station. For Huntley station, combined effect of SEIO<sub>Jul</sub> and Nino3.4<sub>Aug</sub> provided the highest correlation, with a Pearson correlation of 0.579. The outcomes support that the effects of climate indices vary spatially, and only single variable/index is not capable

of predicting rainfall with sufficient accuracy. However, the combinations having higher correlations during the calibration were not considered as recommended models for rainfall prediction.

**Table 4.** Pearson correlations of the developed models for the selected rainfall stations.

Indices Combination	Correlations		
	Ainslie Tyson St	Tharwa General Store	Huntly
SEIO <sub>Jun</sub> -Nino3.4 <sub>Jun</sub>	0.533 *	0.620 *	0.485 *
SEIO <sub>Jun</sub> -Nino3.4 <sub>Jul</sub>	0.581 *	0.675 *	0.549 *
SEIO <sub>Jun</sub> -Nino3.4 <sub>Aug</sub>	0.589 *	0.661 *	0.556 *
SEIO <sub>Jul</sub> -Nino3.4 <sub>Jun</sub>	0.544 *	0.597 *	0.477 *
SEIO <sub>Jul</sub> -Nino3.4 <sub>Jul</sub>	0.587 *	0.646 *	0.537 *
SEIO <sub>Jul</sub> -Nino3.4 <sub>Aug</sub>	0.622 *	0.629 *	0.579 *
SEIO <sub>Aug</sub> -Nino3.4 <sub>Jun</sub>	0.463 *	0.537 *	0.444 *
SEIO <sub>Aug</sub> -Nino3.4 <sub>Jul</sub>	0.519 *	0.597 *	0.516 *
SEIO <sub>Jun</sub> -SOI <sub>Jun</sub>	0.472 *	0.489 *	0.400 *
SEIO <sub>Jun</sub> -SOI <sub>Jul</sub>	0.589 *	0.604 *	0.494 *
SEIO <sub>Jun</sub> -SOI <sub>Aug</sub>	0.602 *	0.616 *	0.530 *
SEIO <sub>Jul</sub> -SOI <sub>Jun</sub>	0.446 *	0.408 *	0.338 *
SEIO <sub>Jul</sub> -SOI <sub>Aug</sub>	0.619 *	0.625 *	0.547 *
SEIO <sub>Aug</sub> -SOI <sub>Aug</sub>	0.529 *	0.544 *	0.493 *
DMI <sub>Jun</sub> -SOI <sub>Jun</sub>	0.545 *	0.410 *	0.310 *
DMI <sub>Jun</sub> -SOI <sub>Jul</sub>	0.552 *	0.710 *	0.456 *
DMI <sub>Jun</sub> -SOI <sub>Aug</sub>	0.659 *	0.564 *	0.507 *

The combinations which produce maximum correlation during the validation period were considered to be the recommended models. For this case, SEIO<sub>Jul</sub>-Nino3.4<sub>Aug</sub> is the best model for the Ainslie Tyson St and Huntly stations; whereas SEIO<sub>Jul</sub>-SOI<sub>Aug</sub> is the highest correlation producers for Tharwa General Store station. Therefore, three models that have the highest correlation between the spring rainfall and the climate variables during the validation period have been proposed. Derived models are outlined in Equations (2)–(4) for Ainslie Tyson St, Tharwa General Store and Huntly rainfall stations respectively.

$$\begin{aligned}
 (\text{Rainfall})_{\text{Spring}} = & -74.0733 \times \text{SEIO}_{\text{Jul}}^3 + 69.3359 \times \text{SEIO}_{\text{Jul}}^2 + 11.5707 \times \text{SEIO}_{\text{Jul}} \\
 & + 6.21085 \times \text{Nino3.4}_{\text{Aug}}^3 - 1.57148 \times \text{Nino3.4}_{\text{Aug}}^2 - 26.6653 \\
 & \times \text{Nino3.4}_{\text{Aug}} + 54.6311
 \end{aligned} \quad (2)$$

$$\begin{aligned}
 (\text{Rainfall})_{\text{Spring}} = & -91.0857 \times \text{SEIO}_{\text{Jul}}^3 + 71.6046 \times \text{SEIO}_{\text{Jul}}^2 + 12.3435 \times \text{SEIO}_{\text{Jul}} \\
 & - 1.5962 \times \text{SOI}_{\text{Aug}}^3 - 3.07473 \times \text{SOI}_{\text{Aug}}^2 + 20.7424 \times \text{SOI}_{\text{Aug}} \\
 & + 57.8264
 \end{aligned} \quad (3)$$

$$\begin{aligned}
 (\text{Rainfall})_{\text{Spring}} = & -91.5749 \times \text{SEIO}_{\text{Jul}}^3 + 69.4111 \times \text{SEIO}_{\text{Jul}}^2 + 20.8865 \times \text{SEIO}_{\text{Jul}} \\
 & + 8.33879 \times \text{Nino3.4}_{\text{Aug}}^3 - 1.96053 \times \text{Nino3.4}_{\text{Aug}}^2 + 33.6301 \\
 & \times \text{Nino3.4}_{\text{Aug}} + 59.2245
 \end{aligned} \quad (4)$$

Since the cubic function has the potential to produce the higher correlation between seasonal rainfall and the considered climate indices, the equations have been developed for the cubic function. The combined capability of other functions will be assessed in future.

The plotted comparison of the analysis during the calibration period is shown in Figure 3. According to Figure 3, the non-linear regression models are not capable to replicate the actual seasonal rainfall with considerable accuracy. The statement is especially true for the extreme rainfall. When the rainfall is extremely high or extremely low, the approach is unable to capture the rainfall characteristics as evidence in Figure 3. More sophisticated analysis needs to be performed to replicate

the extreme seasonal rainfalls. However, before concluding general remark, analysis on other area should be performed.

The plotted results of the prediction comparison during the validation period is shown in Figure 4. According to Figure 4, non-linear regression models should be used carefully to predict the seasonal rainfall with reasonable accuracy. To some extent, the approach is capable to predict the rainfall for some stations. For example, the approach is over predicting for Huntley rainfall station as evidence in Figure 4c. Therefore, other sophisticated modelling approaches should be explored for more accurate predictions of seasonal rainfall.

To evaluate the performance of the non-linear models developed, various statistical parameters were calculated. The outputs of the comparison are shown in Table 5. According to the table, the model with correlation more than 0.91 has higher RMSE and MAE than the model with correlation 0.71. In addition, models with correlation 0.86 is having more errors than the other two models. Similar outcomes were also observed for the index of agreement. Therefore, models which have higher correlation do not necessarily produce a lower error rate. The index of agreement close to one is considered to be the best predicting model. Therefore, the models could be used to predict seasonal rainfall with reasonable accuracy. However, the analysis should be performed with more rainfall stations in the same area and other states.

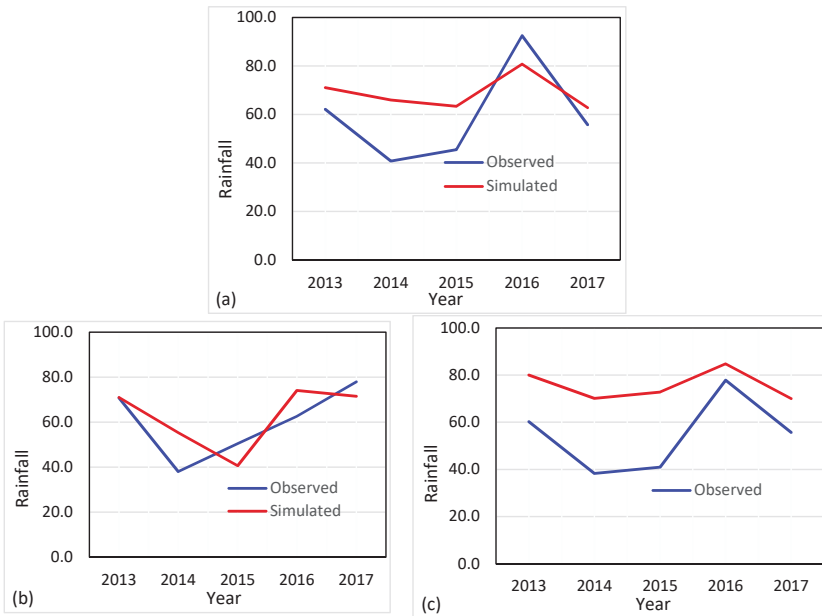


Figure 4. Comparison of the modelling output during the validation period. (a) Ainslie Tyson St; (b) Tharwa General Store; (c) Huntly.

Table 5. Estimated statistical parameters during validation period.

Parameters	Ainslie Tyson St	Tharwa General Store	Huntly
R	0.91	0.71	0.86
RMSE	15.62	10.68	23.08
MAE	14.2	9.0	20.9
d	0.71	0.82	0.56

## 5. Conclusions and Recommendations

Over the last two decades, prediction of seasonal time-series events were given considerable attention. As a result, many modelling approaches were developed and applied to predict seasonal rainfall. However, due to the spatial and temporal variation of rainfall, none of the available models are capable to predict seasonal rainfall with considerable accuracy.

In this research, the efficiency of non-linear regression models were assessed in predicting long-term seasonal rainfall. The non-linear models were constructed considering the lagged climate indices as the potential predictors of seasonal rainfall. Three rainfall stations located in the ACT were selected as a case study. The climate drivers SEIO, Nino3.4, SOI, and DMI were used and analysed in this study. The individual correlations between spring rainfall and the climate indices were determined for six functions (one linear and five non-linear). The functions which have the highest correlation between spring rainfall and the climate indices were further analysed to develop non-linear regression models. Seventeen combined non-linear regression models were developed and assessed to explore appropriate model(s) capable of predicting seasonal rainfall. The correlations between the outputs of the fitted models and the observed data were determined. The models which produce maximum correlation were considered as the potential model for seasonal rainfall forecasting. The accuracy of the predicted models' outputs was assessed by the widely used statistical parameters, R, RMSE, MAE and d. From the analyses of the current study, the following general conclusions could be made:

- Cubic function is capable of producing maximum correlation between seasonal rainfall and the climate indices.
- Logarithmic function produces the minimum correlations between seasonal rainfall and the climate indices.
- DMI-SOI based non-linear models are more suitable to predict seasonal rainfall, as they produce higher correlations.

However, before concluding a general remark, more rainfall stations should be analysed in this area and in other areas, which would be a part of a future study. Moreover, other non-linear modelling and genetic algorithm techniques will be explored, which are likely to be able to predict seasonal rainfalls with higher accuracy.

**Author Contributions:** Conceptualization, I.H.; Methodology, I.H.; Software, I.H.; Formal analysis, I.H.; Writing-Original Draft Preparation, I.H.; Writing-Review & Editing, I.H.; Visualization, I.H.; Methodology, R.E.; Software, R.E.; Formal analysis, R.E.; Conceptualization, M.A.I.; Supervision, M.A.I.; Writing-Original Draft Preparation, M.A.I.; Writing-Review & Editing, M.A.I..

## References

1. Tennant, W.J.; Hewitson, B.C. Intra-seasonal rainfall characteristics and their importance to the seasonal prediction problems. *Int. J. Climatol.* **2002**, *22*, 1033–1048. [CrossRef]
2. Frias, M.D.; Iturbide, M.; Manzanos, R.; Bedia, J.; Fernandez, J.; Herrera, S.; Cofino, A.S.; Gutierrez, J.M. An R package to visualize and communicate uncertainty in seasonal climate prediction. *Environ. Model. Softw.* **2018**, *99*, 101–110. [CrossRef]
3. Jenicek, M.; Seibert, J.; Zappa, M.; Staudinger, M.; Jonas, T. Importance of maximum snow accumulation for summer low flows in humid catchments. *Hydrol. Earth Syst. Sci.* **2016**, *20*, 859–874. [CrossRef]
4. Crochemore, L.; Ramos, M.H.; Pappenberger, F. Bias correcting precipitation forecasts to improve the skill of seasonal streamflow forecasts. *Hydrol. Earth Syst. Sci.* **2016**, *20*, 3601–3618. [CrossRef]
5. Winsemius, H.C.; Dutra, E.; Engelbrecht, F.A.; Archer Van Garderen, E.; Wetterhall, F.; Pappenberger, F.; Werner, M.G.F. The potential value of seasonal forecasts in a changing climate in southern Africa. *Hydrol. Earth Syst. Sci.* **2014**, *18*, 1525–1538. [CrossRef]

6. Goddard, L.; Aitchellouche, Y.; Baethgen, W.; Dettinger, M.; Graham, R.; Hayman, P.; Kadi, M.; Martinez, R.; Meinke, H. Providing seasonal-to-interannual climate information for risk management and decision-making. *Procedia Environ. Sci.* **2010**, *1*, 81–101. [CrossRef]
7. Barnston, A.G.; Li, S.; Mason, S.J.; Dewitt, D.G.; Goddard, L.; Gong, X. Verification of the First 11 Years of IRI's Seasonal Climate Forecasts. *J. Appl. Meteorol. Climatol.* **2010**, *49*, 493–520. [CrossRef]
8. Wang, B. Advance and prospectus of seasonal prediction: Assessment of the APCC/CliPAS 14-model ensemble retrospective seasonal prediction (1980–2004). *Clim. Dyn.* **2009**, *33*, 93–117. [CrossRef]
9. Hossain, I.; Rasel, H.M.; Imteaz, M.A.; Mekanik, F. Long-term seasonal rainfall forecasting: Efficiency of linear modelling technique. *Environ. Earth Sci.* **2018**, *77*, 28. [CrossRef]
10. Mekanik, F.; Imteaz, M.A.; Gato-Trinidad, S.; Elmahdi, A. Multiple linear regression and artificial neural network for long-term rainfall forecasting using large scale climate modes. *J. Hydrol.* **2013**, *503*, 11–21. [CrossRef]
11. Kim, H.M.; Webster, P.J.; Curry, J.A. Seasonal prediction skill of ECMWF System 4 and NCEP CFSv2 retrospective forecast for the Northern Hemisphere winter. *Clim. Dyn.* **2012**, *39*, 2957–2973. [CrossRef]
12. Lim, E.P.; Hendon, H.H.; Anderson, D.L.T.; Charles, A.; Alves, O. Dynamical, statistical-dynamical, and multimodel ensemble forecasts of Australian spring season rainfall. *Mon. Weather Rev.* **2011**, *139*, 958–975. [CrossRef]
13. Manzananas, R.; Frias, M.D.; Cofino, A.S.; Gutierrez, J.M. Validation of 40 year multimodel seasonal precipitation forecasts: The role of ENSO on the global skill. *J. Geophys. Res. Atmos.* **2014**, *119*, 1708–1719. [CrossRef]
14. Rayner, S.; Lach, D.; Ingram, H. Weather forecasts are for wimps: Why water resource managers do not use climate forecasts. *Clim. Chang.* **2005**, *69*, 197–227. [CrossRef]
15. Langford, S.; Hendon, H.H. Assessment of international seasonal rainfall forecasts for Australia and the benefit of multi-model ensembles for improving reliability. In *the Centre for Australian Weather and Climate Research Technical Report No. 039*; The Centre for Australian Weather and Climate Research: Victoria, Australian, 2011.
16. Hossain, I.; Rasel, H.M.; Imteaz, M.A.; Moniruzzaman, M. Statistical correlations between rainfall and climate indices in Western Australia. In *Proceedings of the 21st International Congress on Modelling and Simulation, Gold Coast, Australia, 29 November–4 December 2015*; pp. 1991–1997.
17. Goddard, L.; Mason, S.J.; Zebiak, S.E.; Ropelewski, C.F.; Basher, R.; Cane, M.A. Current approaches to seasonal to interannual climate predictions. *Int. J. Climatol.* **2001**, *21*, 1111–1152. [CrossRef]
18. Saji, N.H.; Yamagata, T. Interference of teleconnection patterns generated from the tropical Indian and Pacific Oceans. *Clim. Res.* **2003**, *25*, 151–169. [CrossRef]
19. Ashok, K.; Guan, Z.; Yamagata, T. Influence of the Indian Ocean Dipole on the Australian winter rainfall. *Geophys. Res. Lett.* **2003**, *30*, 1821. [CrossRef]
20. Rasel, H.M.; Imteaz, M.A.; Mekanik, F. Evaluating the effects of lagged ENSO and SAM as potential predictors for long-term rainfall forecasting. In *Proceedings of the International Conference on Water Resources and Environment (WRE 2015), Beijing, China, 25–28 July 2015*; Miklas, S., Ed.; Taylor & Francis Group: London, UK, 2015; pp. 125–129.
21. Liu, Y.; Fan, K. An application of hybrid downscaling model to forecast summer precipitation at stations in China. *Atmos. Res.* **2014**, *143*, 17–30. [CrossRef]
22. Manzananas, R.; Gutierrez, J.M.; Fernandez, J.; van Meijgaard, E.; Calmanti, S.; Magarino, M.E.; Cofino, A.S.; Herrera, S. Dynamical and statistical downscaling of seasonal temperature forecasts in Europe: Added value for user applications. *Clim. Serv.* **2018**, *9*, 44–56. [CrossRef]
23. Bilgili, M. Prediction of soil temperature using regression and artificial neural network models. *Meteorol. Atmos. Phys.* **2010**, *110*, 59–70. [CrossRef]
24. Adamowski, J.; Chan, H.F.; Prasher, S.O.; Ozga-Zielinski, B.; Sliusarieva, A. Comparison of multiple linear and nonlinear regression, autoregressive integrated moving average, artificial neural network, and wavelet artificial neural network methods for urban water demand forecasting in Montreal, Canada. *Water Resour. Res.* **2012**, *48*. [CrossRef]

25. Esha, R.I.; Imteaz, M.A. Seasonal streamflow prediction using large scale climate drivers for NSW region. In Proceedings of the 22nd International Congress on Modelling and Simulation, Hobart, Australia, 3–8 December 2017; pp. 1593–1599.
26. Pegion, K.; Kirtman, B.P. The impact of air-sea interactions on the simulation of tropical intraseasonal variability. *J. Clim.* **2008**, *21*, 6616–6635. [CrossRef]
27. Jolliffe, I.T.; Stephenson, D.B. *Forecast Verification: A Practitioner's Guide in Atmospheric Science*; John Wiley & Sons: Hoboken, NJ, USA, 2003.

# From Deterministic to Probabilistic Forecasts: The ‘Shift-Target’ Approach in the Milan Urban Area (Northern Italy)

Gabriele Lombardi <sup>1,\*</sup>, Alessandro Ceppi <sup>1</sup>, Giovanni Ravazzani <sup>1</sup>, Silvio Davolio <sup>2</sup>  
and Marco Mancini <sup>1</sup>

<sup>1</sup> Department of Civil and Environmental Engineering, DICA, Politecnico di Milano, 20133 Milano, Italy; alessandro.ceppi@polimi.it (A.C.); giovanni.ravazzani@polimi.it (G.R.); marco.mancini@polimi.it (M.M.)

<sup>2</sup> Institute of Atmospheric Sciences and Climate, National Research Council of Italy, CNR-ISAC, 40129 Bologna, Italy; s.davolio@isac.cnr.it

\* Correspondence: gabriele.lombardi@polimi.it

**Abstract:** The number of natural catastrophes that affect people worldwide is increasing; among these, the hydro-meteorological events represent the worst scenario due to the thousands of deaths and huge damages to private and state ownership they can cause. To prevent this, besides various structural measures, many non-structural solutions, such as the implementation of flood warning systems, have been proposed in recent years. In this study, we suggest a low computational cost method to produce a probabilistic flood prediction system using a single forecast precipitation scenario perturbed via a spatial shift. In fact, it is well-known that accurate forecasts of heavy precipitation, especially associated with deep moist convection, are challenging due to uncertainties arising from the numerical weather prediction (NWP), and high sensitivity to misrepresentation of the initial atmospheric state. Inaccuracies in precipitation forecasts are partially due to spatial misplacing. To produce hydro-meteorological simulations and forecasts, we use a flood forecasting system which comprises the physically-based rainfall-runoff hydrological model FEST-WB developed by the Politecnico di Milano, and the MOLOCH meteorological model provided by the Institute of Atmospheric Sciences and Climate (CNR-ISAC). The areas of study are the hydrological basins of the rivers Seveso, Olona, and Lambro located in the northern part of Milan city (northern Italy) where this system works every day in real-time. In this paper, we show the performance of reforecasts carried out between the years 2012 and 2015: in particular, we explore the ‘Shift-Target’ (ST) approach in order to obtain 40 ensemble members, which we assume equally likely, derived from the available deterministic precipitation forecast. Performances are shown through statistical indexes based on exceeding the threshold for different gauge stations over the three hydrological basins. Results highlight how the Shift-Target approach complements the deterministic MOLOCH-based flood forecast for warning purposes.

**Keywords:** floods; urban river basins; Shift-Target approach; hydrological simulations; probabilistic forecasts

---

## 1. Introduction

From a civil protection point of view, hydro-meteorological forecasts can be seen as a powerful tool of non-structural measures to produce early flood warnings and better counteract potential river flood impacts, whose number is increasing worldwide [1]. Nevertheless, in order to be credible by local authorities and, above all, by citizens, a prediction system must be verified [2], and the verification analysis should be conducted with a large sample of consistent forecasts and observations. In this context,

Demargne et al. [3] proposed the following key questions to guide forecast verification analysis: How suitable are the forecasts for a given application? Are they sufficiently unbiased for the decisions to be made? Are they sufficiently skillful compared to a reference forecast system to justify the method in use?

The ultimate criterion of a good forecast is the decision adopted from it and, from our point of view, it should communicate the information that an end-user needs. Already proposed by Murphy [4] in 1993, good forecasting is not only a matter of “getting it right”, but also to make the receivers understand it, and, above all, to be able to draw conclusions from it [5]. Adopting this framework, in this analysis, we are not interested in predicting river discharge with an accurate flood peak in magnitude as well as timing, but in predicting the probability of exceeding any threshold before the event, in order to provide early flood warnings to local authorities.

Nowadays, it is well known in the scientific community around the world that ensemble or probabilistic forecasts contain more information than single-valued forecasts [6,7], a key topic of the EFAS (European Flood Awareness System) and HEPEX (<https://hepex.irstea.fr/>) projects “to demonstrate the added value of hydrological ensemble predictions (HEPS) for emergency management and water resources sectors to make decisions that have important consequences for economy, public health and safety [8]”.

Notwithstanding this, local authorities and citizens continue to disseminate and prefer deterministic hydro-meteorological forecasts, in particular in Italy where this study is set, without including any notion of probability (or chance) of a phenomenon occurring (such as flooding) when the forecast information is communicated. This is possibly an attempt of the authorities to avoid public confusion from multiple, conflicting warnings, while citizens habitually trust a single forecast only, and they are not educated enough to deal with probabilistic prediction.

The use of ensemble prediction systems allows researchers to properly quantify and communicate forecast uncertainties, but from our experience, we are aware that the communication of uncertainties to end-users is difficult and critical [9,10]. For instance, think about a forecast of a 50% probability: users often consider it to indicate that the forecaster is simply “sitting on the fence” [11]. However, if the observed frequency of the event is low, then a 50% probability is a strong signal. Just think of a 50% probability for an airplane to crash before a flight: no passenger would fly on that airplane! Therefore, developments to formalize forecast uncertainty began exploring human expertise and forecasters’ capacity to translate forecast uncertainty into statistical confidence intervals [12].

In addition to initial conditions (e.g., missing data, anthropogenic interferences) and hydrological model uncertainty (e.g., calibration of parameters, conceptualization of the model, etc.), another key issue of forecast output uncertainty [13] is the capacity to correctly identify future precipitation both in space and time, which is especially critical when integrating precipitation on small watersheds for hydrological forecasts with a high impact on QPE (Quantitative Precipitation Estimates). Unfortunately, accurate forecasts of deep moist convection and associated extreme rainfall are arduous to be precisely predicted in terms of amount, timing, and target over small hydrological basins due to uncertainties arising from numerical weather prediction (NWP) models, including physical parameterizations and numerical schemes, and to the rapid growth of errors already affecting the initial atmospheric state. Therefore, a probabilistic forecasting approach that can cope and deal with these uncertainties is required [14,15].

Since only a deterministic precipitation forecast is available to produce hydrological forecasts, in this analysis, we tested a pragmatic approach proposed by Thies et al. [16] to account for the precipitation forecast uncertainty: a low computational cost method was set up to produce probabilistic hydrological forecasts based on spatially shifting a single-valued precipitation forecast scenario using different spatial domain shifts.

In particular, we explore an alternative way of the Thies’ approach: from a deterministic precipitation forecast issued by the MOLOCH meteorological model (described in Section 2.2), we obtain 40 ‘ensemble members’, equivalent to 40 spatial shifts of the predicted rainfall field in eight directions (North, South, West, East, North-West, North-East, South-West, South-East) at each step of 10 km from 0 to 50 km (which approximately is the entire basin dimensions), maintaining the

temperature domain so that it is unchanged. This strategy, called the 'Shift-Target' (ST) approach, provides 40 discharge forecasts which we assumed to be equally likely in terms of occurrence probability in space and it investigates how the spatial uncertainty may impact the flood forecasts and the potential exceedance of flood warning thresholds.

In order to run hydro-meteorological predictions, we use a flood forecasting system which couples the physically based rainfall-runoff hydrological model FEST-WB with the MOLOCH meteorological model as described in Section 2. The area of interest comprises the three hydrological basins of the rivers Seveso, Olona, and Lambro, located in the northern part of Milan, northern Italy: an urban area which has been subjected to a high flood hazard in the past.

This implemented system works every day in real-time and it can be freely consulted at this web site: [sol.mmido.it](http://sol.mmido.it) (MMI, Milano, Italy). This adopted open source policy allows the public to see and exploit the results of our investment in science, and monitoring real-time products can inspire new research that improves techniques; even crowdfunding has been launched between 2017 and 2018.

For a meaningful verification analysis of the system performance, hindcasting (or retrospective forecasting) has been carried out for the period between 2012 and 2015 and the results are based on verification metrics (including contingency scores relative to various exceedance threshold values) for different gauge stations within the three basins.

The paper has a double scope: first, it aims to demonstrate the value of probabilistic hydrological forecasts obtained through the ST procedure in comparison with the single-valued MOLOCH-based hydrological forecast; second, to assess if the proposed shift method can be useful for civil protection services.

The paper is structured as follows: Chapter 2 describes the materials and methods: Section 2.1 shows the area of study which comprises the Milan urban basins; Sections 2.2 and 2.3 present the MOLOCH meteorological model and the FEST-WB hydrological model, respectively; and Sections 2.4 and 2.5 describe the coupling strategy and the verification scores, respectively. Chapter 3 shows the performance of the Shift-Target approach based on MOLOCH shift forecasts and Chapter 4 documents this paper's conclusions.

## 2. Materials and Methods

### 2.1. Area of Study

Milan is one of the most densely populated city in Italy with 1,316,000 inhabitants living in 182 km<sup>2</sup>. Several rivers and creeks drain to Milan (Figure 1). The main rivers are the Lambro (area of 500 km<sup>2</sup>), the Seveso (area of 207 km<sup>2</sup>), and the Olona (area of 208 km<sup>2</sup>), plus a number of minor tributaries, for a total drainage surface of about 1300 km<sup>2</sup>.

Several flood events hit Milan in the past so that, starting from the 1970s, a series of structural flood mitigation measures, such as the Ponte Gurone dam over the Olona basin, the North-West filling channel over the Seveso, and the Pusiano dam over the Lambro, have been adopted with the aim of reducing the flood risk in the urban areas in the last decades. However, despite the complex flood protection system, the city was still impacted by floods in recent years: the 18 September 2010 with 80 M€ damages along the Seveso and Lambro rivers, the 8 July 2014 with 55 M€ damages along the Seveso river, the 15 November 2014 with 6 M€ damages along the Seveso and Lambro rivers, and the 15 July 2009 with 30 M€ along the Olona river.

According to Nemeč's [17] recommendation, "to keep the people away from the water, and not the water away from the people", the implementation of a hydro-meteorological prediction system may provide additional support as a non-structural measure for early warning. In fact, since these basins have a response time of a few hours, warnings with a sufficient lead time will enable civil protection authorities and the public to exercise caution and take preventive measures to mitigate the impacts of flooding [18].

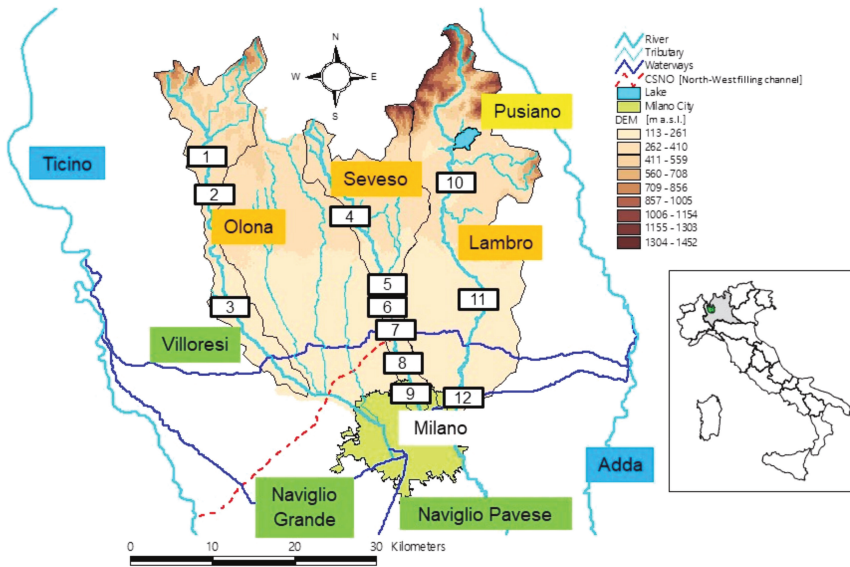


**Figure 1.** River basins draining to Milano urban area. White rectangles denote sections for which the realtime forecasting system provide warnings: (1) Lozza, (2) Castiglione Olona, (3) Castellanza, (4) Cantù, (5) Cesano Maderno, (6) Bovisio Masciago, (7) Paderno Dugnano, (8) Cormano, (9) Milano Niguarda, (10) Lambrugo, (11) Peregallo, (12) Milano via Feltrè. Reprinted from [14], with permission from Elsevier.

At present, hydro-meteorological forecasts, published online, are implemented over the twelve gauge sections shown in Figure 1. However, for the 2012–2015 reforecasting period, not all the observed data were available; hence the verification analysis (shown in Section 2.5) is carried out for only half of the gauge stations, those with at least 900 days of available data.

## 2.2. The MOLOCH Meteorological Model

MOLOCH [19] is a non-hydrostatic, fully compressible, convection-resolving model, developed at the CNR-ISAC (National Research Council of Italy, Institute of Atmospheric Sciences and Climate). It integrates the set of atmospheric equations using a latitude–longitude rotated grid and a hybrid terrain-following vertical coordinate, depending on air density, which relaxes to horizontal surfaces at a higher elevation from the ground. Details on numerical schemes and model physics, as well as the results of the application to severe weather events and floods, can be found in [20–22]. Time integration is based on a time-split scheme with an implicit treatment of the vertical propagation of sound waves and a forward-backward scheme for the horizontal propagation of gravity and sound waves. Advection is computed using a second order implementation of the Godunov method [23], which is particularly suited to integrate in time the conservation of a scalar quantity [24]. The atmospheric radiation is based on a combined application of the Ritter and Geleyn scheme [25] and the ECMWF scheme [26]. The turbulence scheme is based on an eddy kinetic energy – mixing length ( $E - l$ ), 1.5-order closure theory [27], where the turbulent kinetic energy equation (including advection) is evaluated. A soil model with seven layers takes into account orography, the geographical distribution of soil types, soil physical parameters, and vegetation coverage, as well as soil physical processes. The microphysical scheme is based on the parameterization proposed by [28] with successive upgrades, and it describes the conversions and interactions of cloud water, cloud ice, and hydrometeors (rain, snow and graupel). MOLOCH is implemented over Italy with a daily operational chain (<http://www.isac.cnr.it/dinamica/projects/forecasts>) that also comprises the hydrostatic model BOLAM [20], and provides operational forecasts for the following 45 h. The initial and

boundary conditions for the BOLAM model are derived from the analyses (00 UTC) and forecasts of the Global Forecast System (GFS, NOAA/NCEP, USA) global model, while MOLOCH is nested (1-way) in BOLAM, initialized with a 3-h BOLAM forecast in order to avoid downscaling based on pure interpolation from the global model. In the period 2012–2017, MOLOCH has undergone continuous development. In particular, its implementation has changed. In fact, its horizontal resolution increased from 2.2 km to 1.25 in October 2016. At present, MOLOCH employs 60 atmospheric levels with output fields available at an hourly frequency.

### 2.3. The FEST-WB Hydrological Model

For transforming rainfall into runoff, we used the physically-based, spatially distributed FEST-WB (Flash–flood Event–based Spatially distributed rainfall–runoff Transformation, including Water Balance) model, developed by the Politecnico di Milano on top of MOSAICO library [29,30]. The FEST-WB accounts for the main processes of the hydrological cycle: snow melting and accumulation, infiltration, evapotranspiration, surface runoff, flow routing, and subsurface flow. The river basin is discretized with a mesh of regular square cells ( $200 \times 200$  m in this study), where water fluxes are calculated at an hourly time step. For further details on the development and application of the FEST-WB, the reader can refer to [31–34].

### 2.4. The Coupling Strategy

The proposed forecasting cascade system couples (1-way) the MOLOCH meteorological model with the FEST-WB model using the same strategy adopted in [13,33]. Temperature and precipitation outputs are forced into the hydrological model in order to forecast the main hydrological variables (discharge, evapotranspiration, soil moisture, etc.). In this study, we only focus on forecast runoff in the selected gauge sections mentioned in Section 2 for the entire MOLOCH lead time (45 h), adding 12 h for discharge routing at the end of the hydrological forecasting period to get the entire recession limb of the hydrograph. This choice is due to the chance that the precipitation and the observed peak discharge occur before the end of the forecast horizon but the runoff peaks are forecasted later.

Furthermore, since the first few hours of NWP forecasts are not generally reliable, due to the spin-up time of NWP models, we skipped the first 3 h of forecast, hence 54-h flow hindcasts are produced every day between 10 February 2012 and 31 December 2015, which represent up to ~1400 forecasts in total.

Similar to the method proposed by [35], here we aim to account for the spatial uncertainty of the precipitation forecast provided by the meteorological model for the hydrological basins (especially for smaller ones) by applying the ST method to the single-valued MOLOCH forecast. Forecasting the precipitation cells tens of kilometers away from their correct location could lead to significant errors in the hydrological response of the catchments; especially in these watersheds, which have a prolonged North–South shape.

In Figure 2, we show an example of 40 discharge ensemble forecasts produced by the ST method for the Cantù gauging section displayed with the ‘peak-box’ plot proposed by [36].

Figure 2 shows an example for the 8 July 2014 event, which was one of the most severe episodes in the last 20 years in this area. In this case, the 40-km West-shifted forecast (labelled ‘W04’ in Figure 2) exceeded the highest critical warning threshold, whereas the forecast based on the original MOLOCH precipitation did not exceed any of the warning thresholds. This means that if the “unperturbed” Moloch forecast of the precipitation system was affected by a location error of about 40 km westward, then the intense precipitation would have fallen over our watershed, producing a forecast discharge peak of  $31.8 \text{ m}^3/\text{s}$ .

To summarize the warning information given by all flow ensemble forecasts, the ‘Union Jack’ plot (Figure 3) displays the 40 maximum discharges values over the 54-h horizon associated with their spatial shift in all eight directions with a background cell color according to exceeded discharge thresholds.

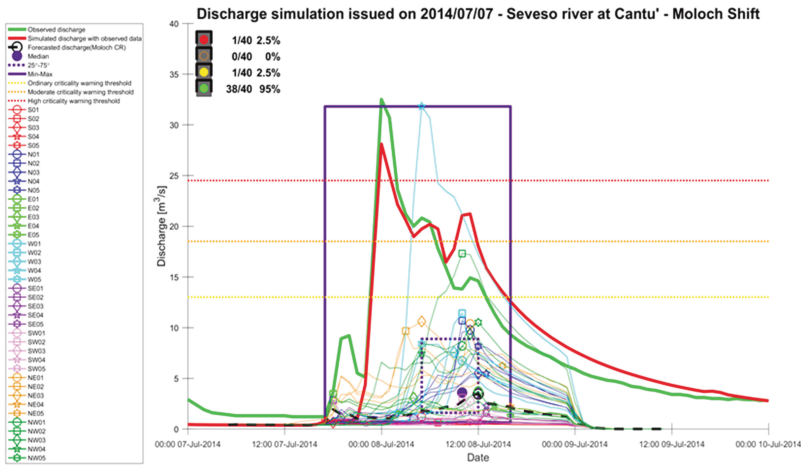


Figure 2. Forty discharge forecasts obtained by forty precipitation domain shifts, issued on 7 July 2014 over the Seveso basin closed at the Cantù gauge section. Observed discharge is shown in the green line and simulated discharge by FEST-WB forced with observed data in red, while different colors identify the hydrological forecasts driven by the Shift-Target (ST) approach.

North-West	-0.5LONg	-0.4LONg	-0.3LONg	-0.2LONg	-0.1LONg	North	+0.1LONg	+0.2LONg	+0.3LONg	+0.4LONg	+0.5LONg	North-East
+0.5LAT	10.5	Na	Na	Na	Na	8.2	Na	Na	Na	Na	6.2	+0.5LAT
+0.4LAT	Na	7.4	Na	Na	Na	5.5	Na	Na	Na	2.2	Na	+0.4LAT
+0.3LAT	Na	Na	9.4	Na	Na	5.5	Na	Na	10.6	Na	Na	+0.3LAT
+0.2LAT	Na	Na	Na	17.3	Na	10.7	Na	9.7	Na	Na	Na	+0.2LAT
+0.1LAT	Na	Na	Na	Na	8.2	9.8	10.4	Na	Na	Na	Na	+0.1LAT
West	8.4	31.8	7.6	11.4	6.7	3.4	3.7	3.5	3.1	2.3	1.3	East
-0.1LAT	Na	Na	Na	Na	2.7	1.2	1	Na	Na	Na	Na	-0.1LAT
-0.2LAT	Na	Na	Na	3.1	Na	0.63	Na	2.9	Na	Na	Na	-0.2LAT
-0.3LAT	Na	Na	1.8	Na	Na	0.63	Na	Na	1.1	Na	Na	-0.3LAT
-0.4LAT	Na	0.69	Na	Na	Na	0.8	Na	Na	Na	2.3	Na	-0.4LAT
-0.5LAT	0.69	Na	Na	Na	Na	1.6	Na	Na	Na	Na	1.6	-0.5LAT
South-West	-0.5LONg	-0.4LONg	-0.3LONg	-0.2LONg	-0.1LONg	South	+0.1LONg	+0.2LONg	+0.3LONg	+0.4LONg	+0.5LONg	South-East

Figure 3. Union Jack plot forecast for the Cantù section issued on 7 July 2014: the 40 values are the maximum discharge forecasts over the entire simulation horizon according to the latitude and longitude shift from 0.1 to 0.5 degree, which is approximately 10 to 50 km.

Representing the 40 forecasted peak discharges on the ‘Union Jack’ with colour-coded impacts meets the requirements of the civil protection services to quickly assess the worst-case scenario based on the potential spatial error of the MOLOCH precipitation forecast.

When operating in real-time, it is possible to follow the evolution of the storm through cell tracking tools, using weather radar images. Forecasters could then evaluate which of the 40 ensemble members may be more realistic based on the storm evolution over the last hours, leading to a better understanding of the ‘most likely’ flooding scenario. Therefore, the Shift-Target approach can provide useful information, letting us know about an a-priori possible flood scenario.

It is worth noting that we are not investigating which is the most probable spatial shift or to calculate a spatial weight of these shifts. Concerning this issue, a specific research activity is actually under development, but this is not the aim of our paper. Here, we simply assume that all the 40 combinations are equally likely. Even an error in the peak time is not taken into consideration, since for local Italian civil protection bodies, the most important information is the exceedance of warning thresholds during the 24-h of the following day, in order to implement flood risk protection measures. Hence, in this framework, we would like to evaluate whether this low computational method, which generates a probabilistic precipitation forecast, performs better than the deterministic MOLOCH, and if its performance can generate an added value for civil protection purposes.

2.5. Verification Scores

Common statistical indexes used in scientific literature ([www.cawcr.gov.au/projects/verification](http://www.cawcr.gov.au/projects/verification)) [37] are calculated setting up a 4 × 4 contingency table which compares forecasted and observed events exceeding or not exceeding the three warning thresholds (Table 1); these thresholds are concurrently used by the contingency table and their values are provided for each gauge station by the Regional Civil Protection of Lombardy. Yellow, orange, and red thresholds are related to the discharge with 2-, 5-, and 10-year return periods, respectively.

**Table 1.** Performance of flows derived from the single-valued Moloch forecast and from the spatially shifted ensemble forecasts. A refers to Hits, B to Misses, C to False Alarm, and D to Correct Negatives, while the subscripts 1, 2, and 3 are levels of wrong prediction.

		Observed			
		No	Yes	Yes	Yes
Forecasted	No	D	B <sub>1</sub>	B <sub>2</sub>	B <sub>3</sub>
	Yes	C <sub>1</sub>	A	B <sub>1</sub>	B <sub>2</sub>
	Yes	C <sub>2</sub>	C <sub>1</sub>	A	B <sub>1</sub>
	Yes	C <sub>3</sub>	C <sub>2</sub>	C <sub>1</sub>	A

In this analysis, we calculate the Accuracy, the Bias Score, the Percent False Alarm (PFA), the Percent Missed Alarm (PMA), and the Correct Negatives Ratio (CNR). Since these three latter scores consider the non-occurred events, which are the majority in the dataset, we also calculate the FAR (False Alarm Ratio), the POD (Probability of Detection), and the Probability of Missed Alarm (POMA), especially to assess the performance in those critical situations when a warning threshold has been exceeded, excluding the other corrected non-events. In fact, for low frequency events such as severe weather warnings, there is a high frequency of “not forecast/not occurred” events. This gives high performance values that are misleading with regard to the forecasting of the low frequency event. For a 4 × 4 contingency table, statistical indexes are slightly different from the classical 2 × 2 as in [38,39]. Hence, in Table 2, we report all the equation formulae used to calculate the performance indexes in Section 2.5.

**Table 2.** Equation formulae used to calculate the common statistical indexes.

	Formula	Best Score	Range
N	$\sum A + \sum B + \sum C + D$	/	/
Accuracy	$(\sum A + D)/N$	100%	0/100%
Bias Score <sub>2×2</sub>	$(A + C)/(A + B)$	1	0/+∞
Bias Score <sub>n×n</sub>	$Yes_F / Yes_O$	1	0/+∞
PFA	$\sum C/N$	0%	0/100%
PMA	$\sum B/N$	0%	0/100%
FAR <sub>2×2</sub>	$C/(A + C)$	0%	0/100%
FAR <sub>n×n</sub>	$\sum C/Yes_F$	0%	0/100%
POMA <sub>2×2</sub>	$B/(A + B)$	0%	0/100%
POMA <sub>n×n</sub>	$\sum B/Yes_O$	0%	0/100%
POD <sub>2×2</sub>	$A/(A + B)$	100%	0/100%
POD <sub>n×n</sub>	$\sum A/Yes_O$	100%	0/100%
CNR <sub>2×2</sub>	$D/(B + D)$	100%	0/100%
CNR <sub>n×n</sub>	$D/No_F$	100%	0/100%

Percent False Alarm (PFA), Percent Missed Alarm (PMA), False Alarm Ratio (FAR), Probability of Missed Alarm (POMA), Probability of Detection (POD), Correct Negatives Ratio (CNR).

In particular,  $No_F$  is the sum of all terms in the first row of Table 1;  $Yes_F$  is the sum of the second, third, and fourth row; and  $Yes_O$  is the sum of all terms in the second, third, and fourth column.

Furthermore, another issue relates to verifying the magnitude of our mistakes: i.e., how far are false or missed alarms from observations? If a red alert was issued, was my forecast orange, yellow, or green? This kind of error has a different impact for civil protection authorities. Hence, we introduce new statistical indexes (Table 3) weighted on the distance between observations and false/missed alarms for the three thresholds (yellow, orange, and red). In other words, the closer the wrong prediction is to the Hits, the lesser its error is weighted. The errors are counted as a unit fraction equal to  $k/s$ , where  $k$  is the step distance from the Hits and  $s$  is the number of thresholds (here, it is equal to 3). The worst cases are three steps distance from the Hits, hence dividing it by the number of thresholds, we obtain the unit.

**Table 3.** Weighted equation formulae used to calculate the common statistical indexes.

	Formula	Best Score	Range
PFA <sub>weighted</sub>	$\sum^k(\sum C_k \times k/s)/N$	0%	0/100%
PMA <sub>weighted</sub>	$\sum^k(\sum B_k \times k/s)/N$	0%	0/100%
FAR <sub>n×n</sub> weighted	$\sum^k(\sum C_k \times k/s)/(\sum C + \sum A + \sum B_{Yes_F})$	0%	0/100%
POMA <sub>n×n</sub> weighted	$\sum^k(\sum B_k \times k/s)/(\sum B + \sum A + \sum C_{Yes_O})$	0%	0/100%

$C_{Yes_O}$  refers to those cells containing C in “Yes” observed columns in Table 1, while  $B_{Yes_F}$  indicates the cells containing B in “Yes” forecasted rows.

### 3. Results and Discussion

In this section, we discuss the main results obtained through the comparison between the performances of the single-valued MOLOCH forecasts and the ST ensemble forecasts. First of all, how do these two approaches exactly predict a non-event (green code: no alert)? In Table 4, we report the observed frequency related to the MOLOCH green code prediction, CNR, and the one related to a 95–100% predicted shift probability of the same green code. A good reliability is found: the frequency is always higher than 92% for both the MOLOCH and ST forecasts at every gauge station: this is proof that the two procedures are able to correctly predict non-events with a slight improvement in the ST.

**Table 4.** Correct Negatives Ratio (CNR) for the MOLOCH deterministic forecast compared with the observed frequency related to the non-event probability higher than 95% for the ST forecasts.

Basin	Section	Moloch (%)	Shift (%)
Seveso	Cantù	96.12	96.89
Olona	Castellanza	97.29	98.27
	Castiglione	99.16	99.46
	Lambrugo	95.76	96.89
Lambro	Milano F.	92.98	93.66
	Peregallo	93.99	94.86

To evaluate the performance of the ST in comparison with the deterministic MOLOCH, we calculate contingency tables for MOLOCH vs. observations, and ST vs. observations (Figures 4 and 5, respectively) in every gauge section. To build these contingency tables for the ST, a categorical forecast has to be assigned from the probabilities of the four alert codes. Our strategy is to choose, as representative of ensembles, the worst critical warning level from red to green, issued with a probability level equal or higher than a given percentage. However, in order to assess a suitable significant percentage to be applied to our instances, we experimented many alternatives. We started with the 33% threshold exceedance probability (at least 14 ensembles out of 40) derived from the Map D-Phase project outcomes [40,41], then we tried with 20% (8 out of 40) and 10% (4 out of 40). Results obtained for the 33% and 20%, for the sake of brevity not shown here, reveal that the unperturbed MOLOCH forecast is slightly preferable: most of the verification scores are similar but better, compared to those of the ST. This can be interpreted as a high skill reached by the deterministic model: i.e., it is not necessary to shift the precipitation domain since its accuracy is itself satisfactory. Maybe, this is not true with other deterministic weather models and this could be an issue for further investigations.

Nevertheless, given the nature of this “non-conventional” ensemble approach, we focus on the contingency scores based on the 10% probability level, since it is not so significant to have a high percentage of exceeding thresholds as to identify that four members out of 40 (equal to 10%) can at least cause dangerous flood scenarios. In Figures 4 and 5, all the contingency tables for the MOLOCH and ST model, respectively, are reported; one for every gauge station analyzed.

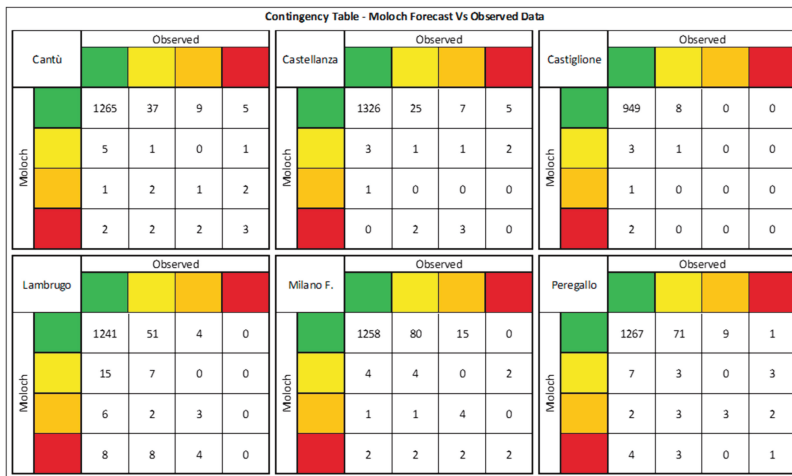


**Figure 4.** 4 × 4 contingency tables for the gauge section of Cantù, Castellanza, Castiglione, Lambrugo, Milano via Feltre, and Peregallo evaluating the “unperturbed” Moloch forecast vs. the observed data.

Contingency Table - Shift Forecast (33%, discriminating percentage) Vs Observed Data																	
Cantù		Observed				Castellanza		Observed				Castiglione		Observed			
		Green	Yellow	Orange	Red			Green	Yellow	Orange	Red			Green	Yellow	Orange	Red
Shift	Green	1268	40	9	7	Green	1328	24	6	6	Green	951	9	0	0		
	Yellow	3	0	1	0	Yellow	1	2	1	1	Yellow	1	0	0	0		
	Orange	0	0	1	2	Orange	0	0	0	0	Orange	0	0	0	0		
	Red	1	2	1	2	Red	1	2	4	0	Red	1	0	0	0		
Lambrugo		Observed				Milano F.		Observed				Peregallo		Observed			
		Green	Yellow	Orange	Red			Green	Yellow	Orange	Red			Green	Yellow	Orange	Red
Shift	Green	1254	56	6	0	Green	1262	84	16	1	Green	1273	72	9	4		
	Yellow	8	2	0	0	Yellow	1	2	2	1	Yellow	5	2	1	1		
	Orange	1	3	1	0	Orange	0	1	1	0	Orange	0	1	2	1		
	Red	6	7	4	0	Red	0	0	2	2	Red	2	5	0	1		

**Figure 5.**  $4 \times 4$  Contingency tables for the section of Cantù, Castellanza, Castiglione, Lambrugo, Milano via Feltre, and Peregallo evaluating the ST forecast vs. observed data.

Starting from all these data, we have calculated many verification scores reported in Table 5 for MOLOCH and Table 6 for ST. First of all, the Bias Score shows a tendency of the MOLOCH model to underforecast, while the ST underforecasts or overforecasts, depending on the investigated section; in general, this latter marks better values.

In Figures 4 and 5, the high number of Correct Negatives (D in Table 1) that lead to a high Accuracy score in every section for both approaches is evident. In addition, the Percent False Alarm and Percent Missed Alarm scores, which have a percentage lower than 8%, are very favorable since these scores consider both the events and non-events. Unfortunately, the small number of False Alarm and Missed Alarm values is not relevant compared to the one of Correct Negatives, and therefore, these scores are not consistent when we refer to only those cases that have exceeded the thresholds.

Hence, to compare the two approaches in-depth, we take into account FAR, POMA, and POD, since they do not consider the Correct Negatives and they fully highlight the performance differences. The ST has a POD higher in four out of the six gauge sections, equal at Lambrugo, and lower at Milano via Feltre: therefore, this shows the MOLOCH's main tendency to underforecast, as already shown by the Bias Score.

With regard to the FAR, MOLOCH prevails on ST in all sections. The opposite comment can be made for POMA, which is lower for the ST than for MOLOCH. Therefore, the MOLOCH is more suitable to reduce False Alarm (FA), while the ST minimizes Missed Alarm (MA) better, which is more important for civil protection purposes, because flood damages for a missed alarm have a higher economic cost in comparison with counteractions to activate a false alarm; hence this can be considered a plus for the ST approach.

**Table 5.** Statistical indexes calculated from the MOLOCH “unperturbed” contingency tables.

MOLOCH	Cantù	Castellanza	Castiglione	Lambrugo	Milano F.	Peregallo
Accuracy	94.92%	96.44%	98.55%	92.74%	92.08%	92.39%
Bias Score	0.34	0.28	0.78	0.67	0.21	0.31
PFA	1.05%	0.65%	0.62%	3.19%	0.87%	1.38%
PMA	4.04%	2.91%	0.83%	4.08%	7.04%	6.24%
FAR	63.64%	69.23%	85.71%	81.13%	50.00%	61.29%
POMA	83.08%	86.96%	88.89%	69.62%	86.61%	86.87%
POD	7.69%	2.17%	11.11%	12.66%	8.93%	7.07%

**Table 6.** Statistical indexes calculated from the Shift-Target contingency tables.

Shift-Target	Cantù	Castellanza	Castiglione	Lambrugo	Milano F.	Peregallo
Accuracy	94.47%	96.00%	96.89%	90.59%	91.50%	91.88%
Bias Score	0.58	0.67	2.78	1.19	0.34	0.56
PFA	2.17%	1.82%	2.39%	6.00%	1.96%	2.83%
PMA	3.36%	2.18%	0.73%	3.41%	6.54%	5.29%
FAR	76.32%	80.65%	92.00%	86.17%	71.05%	70.91%
POMA	69.23%	65.22%	77.78%	58.23%	80.36%	73.74%
POD	12.31%	8.70%	22.22%	12.66%	6.25%	12.12%

By definition, in a  $4 \times 4$  contingency table, the obtained skill scores are less satisfactory than a traditional  $2 \times 2$ , since the same events, which should be considered as Hits in the  $2 \times 2$ , can also be Hits, but even Missed or False Alarms in a  $4 \times 4$  instead, due to the discretization of warning levels. Hence, in Tables 7 and 8, we calculate the same indexes shown in Tables 5 and 6 regarding False Alarms and Missed Alarms, but weighted in order to distinguish the level in the error prediction.

**Table 7.** Weighted statistical indexes calculated from the MOLOCH “unperturbed” contingency tables.

MOLOCH	Cantù (%)	Castellanza (%)	Castiglione (%)	Lambrugo (%)	Milano F. (%)	Peregallo (%)
PFA <sub>W</sub>	0.52	0.29	0.38	1.80	0.46	0.77
PMA <sub>W</sub>	1.84	1.43	0.28	1.46	2.76	2.42
FAR <sub>W</sub>	31.82	30.77	52.38	45.91	26.39	34.41
POMA <sub>W</sub>	37.95	42.75	29.63	24.89	33.93	33.67

**Table 8.** Weighted statistical indexes calculated from the Shift contingency tables.

Shift-Target	Cantù (%)	Castellanza (%)	Castiglione (%)	Lambrugo (%)	Milano F. (%)	Peregallo (%)
PFA <sub>W</sub>	1.37	1.14	1.63	3.41	1.14	1.72
PMA <sub>W</sub>	1.47	1.07	0.24	1.16	2.49	2.05
FAR <sub>W</sub>	48.25	50.54	62.67	48.94	41.23	43.03
POMA <sub>W</sub>	30.26	31.88	25.93	19.83	30.65	28.62

Here, these new indexes improve the percentage by about 30–50% for the two methods. In particular, the FAR decreases an average of 32% for MOLOCH and 30% for ST, while the POMA is 50% for MOLOCH and 43% for ST. This means that when a warning is wrongly issued, the code error is generally not so far from the observed one. Nevertheless, we are not interested in the absolute scores, but in the comparison between the two approaches.

#### 4. Conclusions

Hydro-meteorological systems are nowadays set up with multi-models or multi-analysis approaches gathering deterministic and ensemble forecasts, with the latter being widespread in the scientific community, in order to provide probabilistic information. However, even when using different weather models, a large uncertainty still remains, especially for small river catchments, concerning the location of forecast precipitation. Hence, the proposed study shows the implementation of a different approach using the deterministic high-resolution MOLOCH meteorological model coupled with the FEST-WB hydrological model to obtain probabilistic forecasts. It consists of shifting the precipitation field at in eight directions from 10 to 50 km a step of 10 km, so that the results are 40 discharge forecasts over each analyzed gauge section. The performance of the Shift-Target approach is compared with the “unperturbed” MOLOCH forecast over a period of four years from 10 February 2012 till 31 December 2015. The results show how the ST does not worsen the quality of the forecast in comparison with the one by MOLOCH, and in some cases, it is even better.

The potentiality of the ST can be seen as an a-priori rainfall generator that can be used in real-time, above all, during convective events when precise thunderstorm cell forecasting is difficult over small river basins, but probable flood scenarios, obtained by spatial shift forecasts, can already be forecasted. Notwithstanding this, the ST approach is conditioned by the unperturbed MOLOCH forecast in terms of QPF (Quantitative Precipitation Forecasts): if the MOLOCH totally misses the precipitation intensity, e.g., underestimating over the entire area, no shift will improve the forecast. Nevertheless, this approach, obtained with a low computation method, has demonstrated that it is able to provide useful information with respect to the deterministic MOLOCH run, in case of a misplacement of precipitation field.

Future developments will concentrate on enlarging our dataset to investigate more flood episodes and to verify with a more robust stochastic approach, which is the probability distribution of spatial, timing, and intensity of precipitation error.

**Author Contributions:** G.L., A.C., G.R., and M.M. conceived and designed the experiments; G.L. performed the experiments; G.L. and A.C. analyzed the data; S.D. provided meteorological forecasts; G.L., A.C., G.R., and S.D. wrote the paper.

**Acknowledgments:** This work represents a contribution to the HyMeX international program and it has been developed under a research scientific agreement between Politecnico di Milano and ISAC-CNR.

#### References

1. Munich Reinsurance Company (Munich Re). *Topics Geo Natural Catastrophes 2016: Analyses, Assessments, Positions*; Munich Re: München, Germany, 2017; p. 80.
2. Demargne, J.; Brown, J.D.; Liu, Y.; Seo, D.-J.; Wu, L.; Toth, Z.; Zhu, Y. Diagnostic verification of hydrometeorological and hydrologic ensembles. *Atmos. Sci. Lett.* **2010**, *11*, 114–122. [CrossRef]
3. Demargne, J.; Mullusky, M.; Werner, K.; Adams, T.; Lindsey, S.; Schwein, N.; Marosi, W.; Welles, E. Application of Forecast Verification Science to Operational River Forecasting in the U.S. National Weather Service. *Bull. Am. Meteorol. Soc.* **2009**, *90*, 779–784. [CrossRef]
4. Murphy, A. What is a good forecast? An essay on the nature of goodness in weather forecasting. *Weather Forecast.* **1993**, *8*, 281–293. [CrossRef]
5. Persson, A. Abstract: The ultimate criterion of a “good” forecast is always the decisions made from it. In Proceedings of the 9th HEPeX Webinar: Five Points to Remember in Risk Forecasting, 24 October 2013.
6. Alfieri, L.; Pappenberger, F.; Wetterhall, F.; Haiden, T.; Richardson, D.; Salamon, P. Evaluation of ensemble streamflow predictions in Europe. *J. Hydrol.* **2014**, *517*, 913–922. [CrossRef]
7. Ramos, M.H.; van Andel, S.J.; Pappenberger, F. Do probabilistic forecasts lead to better decisions? *Hydrol. Earth Syst. Sci.* **2013**, *17*, 2219–2232. [CrossRef]

8. Harrigan, S.; Arnal, L. HEPEX Logo Competition: Reveal Your Inner Artist! Available online: <https://hepex.irstea.fr/hepex-logo-competition-reveal-your-inner-artist/> (accessed on 28 March 2018).
9. Ramos, M.H.; Mathevet, T.; Thielen, T.; Pappenberger, F. Communicating uncertainty in hydro-meteorological forecasts: Mission impossible? *Meteorol. Appl.* **2010**, *17*, 223–235. [CrossRef]
10. Zalachori, I.; Ramos, M.H.; Garçon, R.; Mathevet, T.; Gailhard, J. Statistical processing of forecasts for hydrological ensemble prediction: A comparative study of different bias correction strategies. *Adv. Sci. Res.* **2012**, *8*, 135–141. [CrossRef]
11. WMO (World Meteorological Organization). *Guidelines on Communicating Forecast Uncertainty*; Technical Document PWS-18 WMO/TD 1422; WMO: Geneva, Switzerland, 2008; p. 25.
12. Houdant, B. Contribution à l'amélioration de la Prévision Hydrométéorologique opérationnelle. Pour l'usage des Probabilités dans la Communication Entre Acteurs [Contribution to the Improvement of Operational Hydrometeorological Forecasting. For the Use of Probability in the Communication between Actors]. Ph.D. Thesis, ENGREF, EDF, Grenoble, France, 2004; p. 209. (In French)
13. Jaun, S.; Ahrens, B. Evaluation of a probabilistic hydrometeorological forecast system. *Hydrol. Earth Syst. Sci.* **2009**, *13*, 1031–1043. [CrossRef]
14. Ravazzani, G.; Amengual, A.; Ceppi, A.; Homar, V.; Romero, R.; Lombardi, G.; Mancini, M. Potentialities of ensemble strategies for flood forecasting over the Milano urban area. *J. Hydrol.* **2016**, *539*, 237–253. [CrossRef]
15. Davolio, S.; Miglietta, M.M.; Diomede, T.; Marsigli, C.; Montani, A. A flood episode in northern Italy: Multi-model and single-model mesoscale meteorological ensembles for hydrological predictions. *Hydrol. Earth Syst. Sci.* **2013**, *17*, 2107–2120. [CrossRef]
16. Thies, S.E.; Hense, A.; Damrath, U. Probabilistic precipitation forecasts from a deterministic model: A pragmatic approach. *Meteorol. Appl.* **2005**, *12*, 257–268. [CrossRef]
17. Nemeč, J. Global Runoff Data Sets and Use of Geographic Information Systems. In Proceedings of the ISLSCP Conference, Rome, Italy, 2–6 December 1985. ESA SP-248.
18. Yang, T.-H.; Yang, S.-C.; Ho, J.-Y.; Lin, G.-F.; Hwang, G.-D.; Lee, C.-S. Flash flood warnings using the ensemble precipitation forecasting technique: A case study on forecasting floods in Taiwan caused by typhoons. *J. Hydrol.* **2015**, *520*, 367–378. [CrossRef]
19. Malguzzi, P.; Grossi, G.; Buzzi, A.; Ranzi, R.; Buizza, R. The 1966 “century” flood in Italy: A meteorological and hydrological revisit. *J. Geophys. Res.* **2006**, *111*, D24106. [CrossRef]
20. Buzzi, A.; Davolio, S.; Malguzzi, P.; Drofa, O.; Mastrangelo, D. Heavy rainfall episodes over Liguria of autumn 2011: Numerical forecasting experiments. *Nat. Hazard Earth Syst. Sci.* **2014**, *14*, 1325–1340. [CrossRef]
21. Davolio, S.; Silvestro, F.; Gastaldo, T. Impact of rainfall assimilation on high-resolution hydro-meteorological forecasts over Liguria (Italy). *J. Hydrometeorol.* **2017**, *18*, 2659–2680. [CrossRef]
22. Davolio, S.; Silvestro, F.; Malguzzi, P. Effects of increasing horizontal resolution in a convection permitting model on flood forecasting: The 2011 dramatic events in Liguria (Italy). *J. Hydrometeorol.* **2015**, *16*, 1843–1856. [CrossRef]
23. Godunov, S.K. A difference method for numerical calculation of discontinuous solutions of the equations of hydrodynamics. *Matematicheskii Sbornik* **1959**, *47*, 271–306.
24. Toro, E.F. The weighted average flux method applied to the Euler equations. *Philos. Trans. R. Soc. Lond. A* **1992**, *341*, 499–530. [CrossRef]
25. Ritter, B.; Geleyn, J.F. A comprehensive radiation scheme for numerical weather prediction models with potential applications in climate simulations. *Mon. Weather Rev.* **1992**, *120*, 303–325. [CrossRef]
26. Morcrette, J.-J.; Barker, H.W.; Cole, J.N.S.; Iacono, M.J.; Pincus, R. Impact of a new radiation package, McRad, in the ECMWF Integrated Forecasting System. *Mon. Weather Rev.* **2008**, *136*, 4773–4798. [CrossRef]
27. Zampieri, M.; Malguzzi, P.; Buzzi, A. Sensitivity of quantitative precipitation forecasts to boundary layer parameterization: A flash flood case study in the western Mediterranean. *Nat. Hazards Earth Syst. Sci.* **2005**, *5*, 603–612. [CrossRef]
28. Drofa, O.V.; Malguzzi, P. Parameterization of microphysical processes in a non-hydrostatic prediction model. In Proceedings of the 14th International Conference on Clouds and Precipitation (ICCP), Bologna, Italy, 19–23 July 2004; pp. 1297–3000.
29. Rabuffetti, D.; Ravazzani, G.; Corbari, C.; Mancini, M. Verification of operational Quantitative Discharge Forecast (QDF) for a regional warning system—The AMPHORE case studies in the upper Po River. *Nat. Hazard Earth Syst. Sci.* **2008**, *8*, 161–173. [CrossRef]

30. Ravazzani, G. MOSAICO, a library for raster based hydrological applications. *Comput. Geosci.* **2013**, *51*, 1–6. [CrossRef]
31. Feki, M.; Ravazzani, G.; Ceppi, A.; Mancini, M. Influence of soil hydraulic variability on soil moisture simulations and irrigation scheduling in a maize field. *Agric. Water Manag.* **2018**, *202*, 183–194. [CrossRef]
32. Ceppi, A.; Ravazzani, G.; Corbari, C.; Salerno, R.; Meucci, S.; Mancini, M. Real time drought forecasting system for irrigation management. *Hydrol. Earth Syst. Sci.* **2014**, *18*, 3353–3366. [CrossRef]
33. Ceppi, A.; Ravazzani, G.; Salandin, A.; Rabuffetti, D.; Montani, A.; Borgonovo, E.; Mancini, M. Effects of temperature on flood forecasting: Analysis of an operative case study in Alpine basins. *Nat. Hazards Earth Syst. Sci.* **2013**, *13*, 1051–1062. [CrossRef]
34. Ravazzani, G.; Barbero, S.; Salandin, A.; Senatore, A.; Mancini, M. An integrated hydrological model for assessing climate change impacts on water resources of the Upper Po river basin. *Water Resour. Manag.* **2015**, *29*, 1193–1215. [CrossRef]
35. Diomede, T.; Marsigli, C.; Nerozzi, F.; Papetti, P.; Paccagnella, T. Coupling high-resolution precipitation forecasts and discharge predictions to evaluate the impact of spatial uncertainties in numerical weather prediction model outputs. *J. Meteorol. Atmos. Phys.* **2008**, *102*, 37–62. [CrossRef]
36. Zappa, M.; Fundel, F.; Jaun, S. A ‘peak-box’ approach for supporting interpretation and verification of operational ensemble peak-flow forecast. *Hydrol. Process.* **2013**, *27*, 117–131. [CrossRef]
37. WWRP/WGNE Joint Working Group on Verification cited 2013: Forecast Verification—Issue, Methods and FAQ. Available online: <http://www.cawcr.gov.au/projects/verification> (accessed on 26 January 2015).
38. Jolliffe, I.T.; Stephenson, D.B. (Eds.) *Forecast. Verification: A Practitioner’s Guide*; John Wiley & Sons: Hoboken, NJ, USA, 2012; p. 240.
39. Wilks, D.S. *Statistical Methods in the Atmospheric Sciences*, 2nd ed.; Academic Press: Cambridge, MA, USA, 2006.
40. Zappa, M.; Rotach, M.W.; Arpagaus, M.; Dorninger, M.; Hegg, C.; Montani, A.; Ranzi, R.; Ament, F.; Germann, U.; Grossi, G.; et al. *MAP D-PHASE: Real-Time Demonstration of Hydrological Ensemble Prediction Systems*; Special Issue Article; HEPEX Workshop: Stresa, Italy, June 2007.
41. Rotach, M.W.; Ambrosetti, P.; Ament, F.; Appenzeller, C.; Arpagaus, M.; Bauer, H.-S.; Zappa, M. Supplement to MAP D-PHASE: Real-Time Demonstration of Weather Forecast Quality in the Alpine region: Additional Applications of the D-PHASE Datasets. *Bull. Am. Meteorol. Soc.* **2009**, *90*, s28–s32. [CrossRef]

# Impact of the Rainfall Duration and Temporal Rainfall Distribution Defined Using the Huff Curves on the Hydraulic Flood Modelling Results

Nejc Bezak \*, Mojca Šraj, Simon Rusjan and Matjaž Mikoš

Faculty of Civil and Geodetic Engineering, University of Ljubljana, 1000 Ljubljana, Slovenia; mojca.sraj@fgg.uni-lj.si (M.Š.); simon.rusjan@fgg.uni-lj.si (S.R.); matjaz.mikos@fgg.uni-lj.si (M.M.)

\* Correspondence: nejc.bezak@fgg.uni-lj.si

**Abstract:** In the case of ungauged catchments, different procedures can be used to derive the design hydrograph and design peak discharge, which are crucial input data for the design of different hydrotechnical engineering structures, or the production of flood hazard maps. One of the possible approaches involves using a hydrological model where one can calculate the design hydrograph through the design of a rainfall event. This study investigates the impact of the design rainfall on the combined one-dimensional/two-dimensional (1D/2D) hydraulic modelling results. The Glinščica Stream catchment located in Slovenia (central Europe) is used as a case study. Ten different design rainfall events were compared for 10 and 100-year return periods, where we used Huff curves for the design rainfall event definition. The results indicate that the selection of the design rainfall event should be regarded as an important step, since the hydraulic modelling results for different scenarios differ significantly. In the presented experimental case study, the maximum flooded area extent was twice as large as the minimum one, and the maximum water velocity over flooded areas was more than 10 times larger than the minimum one. This can lead to the production of very different flood hazard maps, and consequently planning very different flood protection schemes.

**Keywords:** design storm; hydraulic modelling; flood hazards; Glinščica catchment; hydrological modelling; Huff curves; HEC-RAS

---

## 1. Introduction

Floods are one of the natural disasters that cause a large amount of economic damage and endanger human lives all over the world [1]. Moreover, a warming climate may cause more frequent and more extreme river flooding in the future, although a consistent trend over the past 50 years in Europe has not been detected [2]. However, Blöschl et al. [2] showed substantial changes in flood timing of rivers in Europe. Similar conclusions can also be made for Slovenia [3]. Altogether, floods are still one of the natural disasters that cause large amounts of economic damage and have significant direct and indirect consequences for the environment and society; by properly designing different flood protection schemes, one can manage flood risk, and consequently reduce the casualties due to flooding [4].

In order to design either green or grey infrastructure measures to reduce flood risk, the information about the design discharge or design hydrograph is needed. If discharge data is available, one can perform either univariate [5] or multivariate [6] flood frequency analysis in order to define design variables. When no discharge data is available, other approaches can be used to define the design variables. Blöschl et al. [7] made a comprehensive overview of methods that can be used for predictions of different hydrological variables in cases of the so-called ungauged catchments. One of the methods that can be used to estimate design variables in such cases is also the application of a hydrological model

to define the design peak discharge or the complete design hydrograph [8,9]. Besides hydrological model parameters that have to be estimated during the calibration of the selected model, a design hyetograph definition has a significant impact on the model results [10–16]. In order to construct a design rainfall event for flood risk assessment, several methods can be applied (e.g., constant intensity method, triangular hyetograph, Natural Resources Conservation Service (NRCS) design storm, frequency-based or alternating block method, and Huff method), most of which are based on intensity–duration–frequency (IDF) relationships, namely on a single point or the entire IDF curve. Using the IDF relationship, we can estimate the frequency or return period of specific rainfall intensity or rainfall amount that can be expected for certain rainfall duration.

However, the same discharge value can be derived from different combinations of storm duration and its return period [13]. In addition to the amount of rainfall with the selected magnitude, the two most important factors related to the design hyetograph selection are the design rainfall duration, and rainfall distribution within the rainfall event (which is also called internal storm structure or temporal rainfall distribution) [15,16]. Šraj et al. [14] have shown that a combination of rainfall duration that is significantly longer than the catchment time of concentration, and constant rainfall intensity within the design rainfall event can yield significantly different (more than 50% smaller) design peak discharges than design hyetographs with a rainfall duration that is approximately equal to the catchment time of concentration and the application of non-uniform (i.e., actual/real) rainfall intensity distribution. The essential differences in the time-to-peak of the resulted hydrographs of the hydrological model and differences in peak discharge can also be the consequence of the maximum rainfall intensity position within the design hyetograph [10,13,14,17].

However, to obtain a typical rainfall distribution within the rainfall event for a region, Huff curves [18] can be used that connect the dimensionless rainfall depth with the dimensionless rainfall duration of an individual rainfall station or region, based upon locally gauged historical data. As such, Huff curves represent typical rainfall characteristics of a region [19,20]. These curves were recently derived for several Slovenian rainfall stations [21]. Dolšak et al. [21] demonstrated that the variability in the Huff curves using different probability levels generally decreases with increasing rainfall duration. The median Huff curve (50%) can be regarded as the most representative, and ought to be used for constructing the design hyetographs [22]. Thus, it appears that a definition of a design hyetograph is one of the most important parts of the hydrograph definition, in cases when hydrological models are used.

In practical engineering applications, design hydrographs are often used as inputs to the hydraulic models in order to determine flooded areas, the impact of the proposed flood protection measures on the flood risk, and similar practical applications. Input hydrographs are one of the most important parameters that can have a significant impact on the hydraulic flood modelling results [23]. Savage et al. [23] have shown that input hydrographs have a significant influence on modelling results, especially during rising limb of the hydrograph. During peak discharge, the channel friction parameter has the largest impact, whereas during the recession part of the hydrograph, the floodplain friction parameter plays an important role. For the predictions of the flood extent, it has been observed that the dominant hydraulic model input factors shift during the flood event. Hall et al. [24], who performed a global sensitivity analysis using flood inundation models, also made similar conclusions. It was found that the Manning roughness coefficient has the dominant impact on uncertainty in the hydraulic model calibration and prediction [24]. The same finding was also reported by Pestotnik et al. [25], who analysed the possibility of using the two-dimensional (2D) model Flo-2D for hydrological modelling for the case of the Glinščica River catchment in Slovenia. Additionally, boundary conditions are also one of the factors that can have a significant impact on hydraulic modelling results [26].

However, the relationship between the design hyetograph selection and hydraulic modelling results remains unclear. Examples of modelling results include the flood extent or flow velocities over floodplains, which can have a significant impact on the stability of a human body or a vehicle in floodwaters [27–30]. Even though some researchers doubt the usefulness of the flood water flow velocities as the appropriate parameter to model flood damages [31], the implementation of the 2007 European Union (EU) Flood Directive governs the determination and zonation of hazards areas using a combination of flood water depths and flow velocities. Different flood hazard zones are then used for the planning of preventive measures, such as the restriction of construction in areas with high flood hazards [32]. Knowing the uncertainty in the assessment of flood hazard and flood risk areas is an important task in flood risk reduction, as the uncertainty in the decision-making process for natural hazards in mountains has been recognised [33,34].

Therefore, the main aim of this study is to explore the relationship between the design hyetograph definition, and hydraulic modelling results. For this purpose, the Glinščica Stream catchment in central Slovenia was selected as the case study. The specific aims are as follows:

- (i) to quantify the effect of rainfall duration on hydraulic modelling results (e.g., flood extent, floodwater velocities);
- (ii) to quantify the impact of temporal rainfall distribution within a rainfall event on hydraulic modelling results, and
- (iii) to compare the differences between flood modelling results (floodplain extents, velocities, volumes, and water depths) for the events with 10 and 100-year return periods.

## 2. Data and Methods

### 2.1. Catchment Description

The Glinščica Stream catchment was selected as the case study in order to investigate the impact of the design rainfall on the hydraulic modelling results. The Glinščica Stream catchment is part of the Gradaščica River catchment that drains into the Ljubljanica River. This river is part of the Sava River catchment; the Glinščica Stream catchment is situated in the central part of Slovenia, and reaches into the eastern part of the urban area of the capital city of Ljubljana (Figure 1). The stream has its source under the southeastern slopes of the hills of Polhograjsko hribovje, and at the village of Podutik, it passes into the flat area of the Ljubljana plain. The topography of the catchment is comprised of hilly areas to the east and west, and a flat plain area in the south. The relief of the Glinščica Stream catchment is diverse, comprising hilly headwater areas, as well as flat plains. The Glinščica Stream catchment is one of the hydrologic experimental catchments in Slovenia [35,36]. Table 1 shows some basic properties of the Glinščica Stream catchment. It has already been studied in some of the previous studies, and a more detailed description of the catchment is provided by Bezak et al., Šraj et al. and Brilly et al. [8,14,37]. The lowland areas of the Gradaščica River, once natural floodplain areas, were partly urbanised in the last couple of decades, which resulted in an elevated flood risk for the area. The last major flood occurred in October 2014, when extensive urbanised areas and more than 1000 houses were flooded.

**Table 1.** Basic characteristics of the Glinščica Stream catchment.

Catchment Area (km <sup>2</sup> )	Elevation (m a.s.l.)	Land-Cover	Soil Characteristics (According to Soil Conservation Service (SCS) Classification)	Mean Annual Precipitation (mm)	Time of Concentration (h)
16.85	from 209 to 590	49% forest, 23% agriculture land, 19% urbanised areas	C and D types with generally low infiltration rates	about 1400	about 6

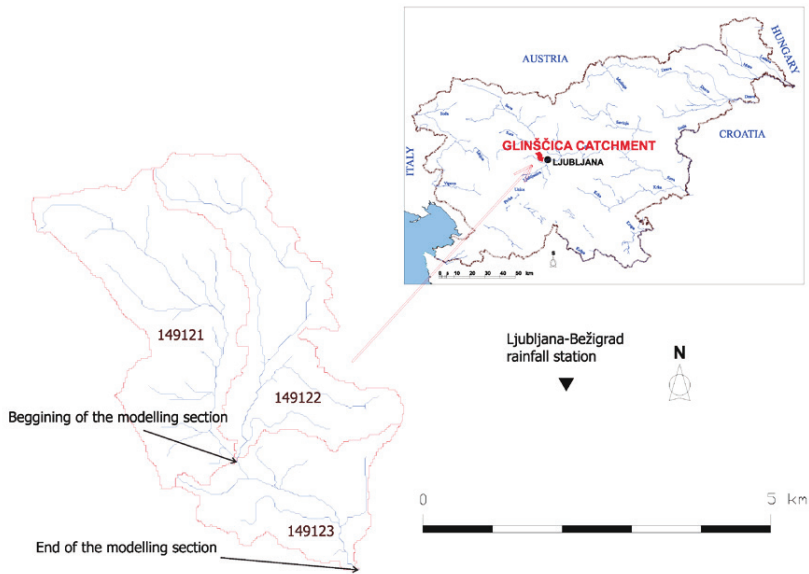


**Figure 1.** Location of the Glinščica Stream catchment on a map of Slovenia, and the Glinščica River catchment divided into three sub-catchments. The hydraulic modelling was performed in the 149123 sub-catchment from the beginning (confluence of sub-catchments 149121 and 149122) to the end (confluence of the Glinščica Stream and the Gradaščica River) of the river network in this sub-catchment.

The official water level and discharge measurements in Slovenia are performed by the Slovenian Environment Agency (ARSO). However, in the Glinščica Stream catchment, there is currently no discharge gauging station (there is about 15 years of data available before 1970, but catchment has significantly changed during the past 50 years [38]; therefore, this data was omitted in this study). For the purpose of the research projects and investigation of hydrological processes in the experimental catchment, the water station, which was equipped with an ultrasonic Doppler instrument (Starflow Unidata 6526 model), was placed in the channel of the Glinščica Stream. However, it was only placed there for the limited period of time [14,37]. This means that design discharges cannot be determined using the frequency analysis approach [5], the use of a different approach is required in order to derive the design values for this catchment.

## 2.2. Hydrological Model

The hydrological model HEC-HMS [39], with a combination of the design hyetographs [21], was used in the study in order to compute design hydrographs that were further used as inputs to the hydraulic model. Three different methods were applied in order to construct the design hyetograph: namely, the Huff method, the constant intensity method, and the frequency storm method. Descriptions of the applied methods can be found, for example, in Ball, Alfieri et al., Azli and Rao, Dolšak et al. [11,17,20,21]. Calibration and validation of the hydrological model of the Glinščica Stream catchment was performed by Šraj et al. [14] using measured discharge data obtained as part of the work that has been done in order to investigate the impact of changed land use (urbanisation) on the hydrological and biogeochemical processes in the experimental catchment [14,37]. For modelling purposes, the Glinščica Stream catchment was divided into three sub-catchments that are shown in Figure 1. A detailed description of the calibration and validation of the hydrological model is provided by Šraj et al. [14].

### 2.3. Hydraulic Model

Results of the hydrological modelling were used as inputs to the hydraulic model. Hydraulic modelling was performed from the begging (confluence of sub-catchments 149121 and 149122) to the end of the sub-catchment 149123 (confluence of the Glinščica Stream and the Gradaščica River) (Figure 1). The Glinščica Stream catchment was modelled with hydraulic model HEC-RAS 5.0.3, which enables one-dimensional (1D) and two-dimensional (2D) unsteady and steady flow simulations [40]. The basic characteristics of the Glinščica Stream catchment hydraulic model are shown in Table 2. Figure 2 shows a graphical representation of the hydraulic model extent. The connection between the river channel (1D) and the 2D flow area was defined as a lateral structure, which is one of the options that can be used to connect 1D flow in a river channel with 2D flow on 2D flow areas [40]. The average cell size on 2D flow areas was  $25.2 \text{ m}^2$  and  $25.3 \text{ m}^2$  for the right bank and left bank 2D flow areas, respectively (Figure 2). The 2D flow areas were represented by the underlying digital terrain model with a cell size of  $1 \text{ m} \times 1 \text{ m}$ , which is available for all of Slovenia. The HEC-RAS preprocessor computes several geometric and hydraulic characteristics of each cell face that are important for the hydraulic modelling [40]. The model also includes five bridges that are located in the modelled area [38]. Inflows to the modelled area are indicated with black lines on Figure 2. The upstream boundary condition was the flow hydrograph from catchment 149121 (shown in Figure 1), and the downstream boundary condition was the normal depth and discharge contributions from sub-catchments 149122 and 149123 (shown in Figure 1) were modelled as lateral inflows. Unsteady flow simulations with full momentum equations [40] were used in this study. The computation interval was 20 s, and a 36-h period was considered in simulations. Most of the simulations were computed in less than 10 min. All of the hydraulic parameters in the hydraulic model were kept constant during the simulations of the selected scenarios that are presented in the next sub-section.

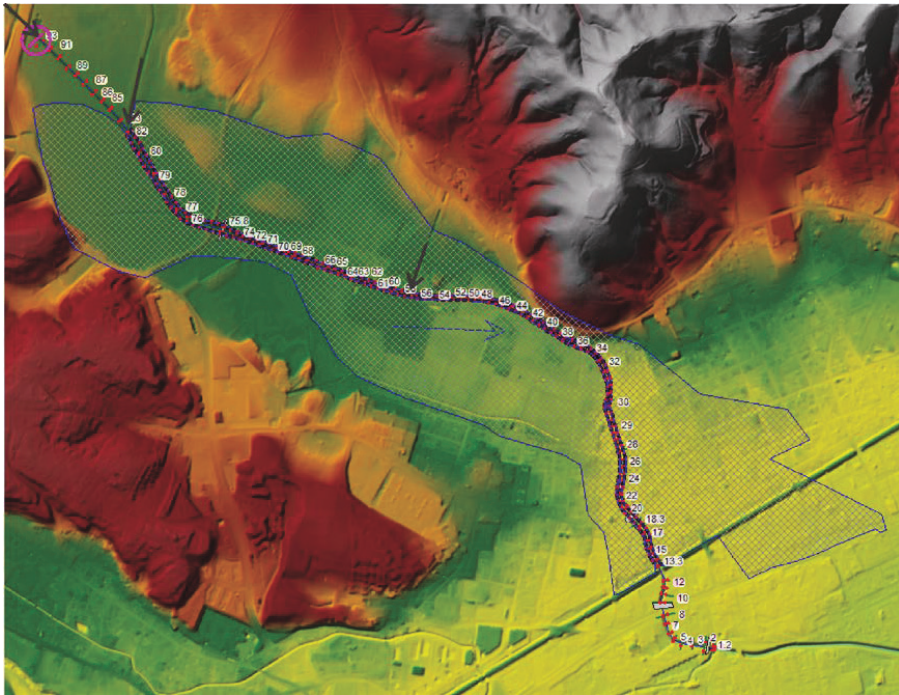


Figure 2. Hydraulic model of the Glinščica Stream catchment with two large 2D flow areas.

**Table 2.** Basic characteristics of the hydraulic model of the Glinščica Stream catchment. 2D: two-dimensional.

River Length (m)	Number of Cross-Sections	Number of 2D Flow Areas	Size of 2D Flow Areas	Manning's Roughness Coefficients
about 3000	93	2	0.64 km <sup>2</sup> (left) and 0.50 km <sup>2</sup> (right)	Between 0.02 to 0.033 for the river channel, 0.04 for the flood area within the cross-section, and between 0.06 and 0.1 for the 2D flood area

#### 2.4. Scenarios (Design Rainfall Events)

In order to evaluate impact of the design rainfall on the hydraulic modelling results, the following 10 scenarios (design rainfall events) were determined and applied as inputs to the hydrological model that was used to compute the flow hydrographs at outflows from individual sub-catchments:

- Design rainfall was defined based on the 50% (Huff 50%, 6 h), 10% (Huff 10%, 6 h), and 90% (Huff 90%, 6 h) Huff curves with a rainfall duration of 6 h (this duration is approximately equal to the catchment time of concentration);
- Design rainfall was defined based on the 50% Huff curve with a rainfall duration of 2 h (Huff 50%, 2 h), 12 h (Huff 50%, 12 h), and 24 h (Huff 50%, 24 h);
- Design rainfall was defined as constant rainfall intensity and rainfall duration of 6 h (Const., 6 h);
- Design rainfall was defined based on the frequency storm method and peak intensity position at 25% (FreqStorm, peak 25%), 50% (FreqStorm, peak 50%), and 75% (FreqStorm, peak 75%) of rainfall duration.

All 10 scenarios were conducted for rainfall with 10 and 100-year return periods. Thus, in total, 20 different combinations were evaluated and analysed. More information about the methodology used to define the Huff curves [21] and intensity–duration–frequency (IDF) curves that were used in this study is available in Bezak et al. [8]. The Huff and IDF curves from the closest Ljubljana-Bežigrad station (shown in Figure 1) were used. Moreover, also additional information about the frequency storm method that was applied in this study is available in Bezak et al. [8]. This method defines the synthetic design hyetograph using the information from the IDF curves, where for different rainfall durations (e.g., 5 min, 15 min, 1 h, 2 h, 3 h, 6 h) the rainfall amount defined by the IDF curve is used. This approach uses the maximum rainfall amounts of different durations as part of one rainfall event, which is usually not the case in the nature (i.e., there is very low probability that the annual maxima of different rainfall durations occur in the same event). Consequently, application of the frequency storm method often results in higher peak discharge values compared to some other design rainfall definitions (from the engineering perspective, this can be regarded as conservative). The main idea of comparison of different scenarios was to explore the impact of the rainfall duration and temporal rainfall distribution within a rainfall event that was defined using Huff curves that were constructed based on the historical rainfall data for different rainfall durations for several Slovenian stations [21] on the hydraulic modelling results.

For the 10 and 100-year return period events, we compared the maximum floodplain extent area, volume of water flowing on the floodplain areas (selected cross-sections are shown in Figure 3), maximum velocities on floodplains, and outflow hydrographs and maximum water depths for all 10 scenarios.

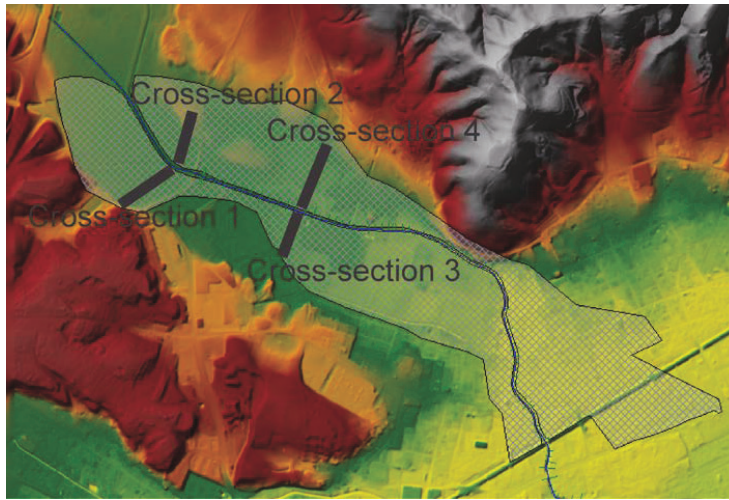


**Figure 3.** Selected cross-sections (1–4) on the floodplain areas that were used to compare volumes flowing on the floodplains, maximum water velocities on the floodplains, and maximum water depths.

### 3. Results and Discussion

#### 3.1. 10-Year Return Period Event

In the first step of the study, we obtained hydraulic modelling results for the 10-year return period. Cases for the selected 10 scenarios were computed, and the results were compared. Figure 4 shows a comparison among the outflow hydrographs for the applied scenarios considering the 10-year return period. It can be seen that rainfall duration has a significant influence on the outflow hydrograph. The scenario that represents the 50% Huff curve with a short rainfall duration of 2 h yields smaller peak discharge values than the scenario applying the same Huff curve with a rainfall duration of 6 h. Also, scenarios with longer rainfall durations and the same Huff curve result in smaller peak discharge values compared to the first scenario (Huff 50%, 6 h), where the rainfall duration is approximately equal to the catchment time of the concentration. This finding is consistent with the results from the previous studies, as Šraj et al. [14] documented, which showed that extending the rainfall duration caused increases in the difference in peak discharge and time-to-peak. Furthermore, also, temporal rainfall distribution within a rainfall event has an important impact on the outflow hydrograph, when comparing rainfall events with the same rainfall duration (6 h) (50%, 10%, and 90% Huff curves, constant rainfall intensity and frequency storm method (25%, 50%, and 75% peak position)). It can be seen that the application of the frequency storm method yields larger peak discharge values than the scenario with 6 h of rainfall duration and the 50% Huff curve and the use of constant rainfall intensity within a rainfall event results in smaller peak discharges than the rainfall duration scenario with the Huff 50% curve over 6 h, which has also been reported by other authors [11,13,14,17]. Alfieri et al. [17] argued that the adoption of any rectangular hyetograph significantly underestimates design hydrograph results. Furthermore, Singh [12] concluded that rainfall patterns with temporal variability result in higher peak discharges than one with constant rainfall intensity. For the same return period, different definitions of the temporal rainfall distribution yield different peak discharge values. Some of these methods that are used to define the temporal rainfall distribution can, from an engineering point of view, be regarded as conservative or not so conservative. For example, using the frequency storm method, one can obtain a design discharge that can be regarded as on the safe side (from the design perspective). On the other hand, the constant intensity method yields smaller peak

discharge values. Different results can also be obtained using different Huff curves (e.g., 10%, 50%, or 90%). Moreover, if we do not fix the return period variable, numerous combinations are possible to define the design hyetograph. Thus, there are alternative approaches possible, such as the so-called optional design hyetograph [41]. However, this approach was not tested in this study.

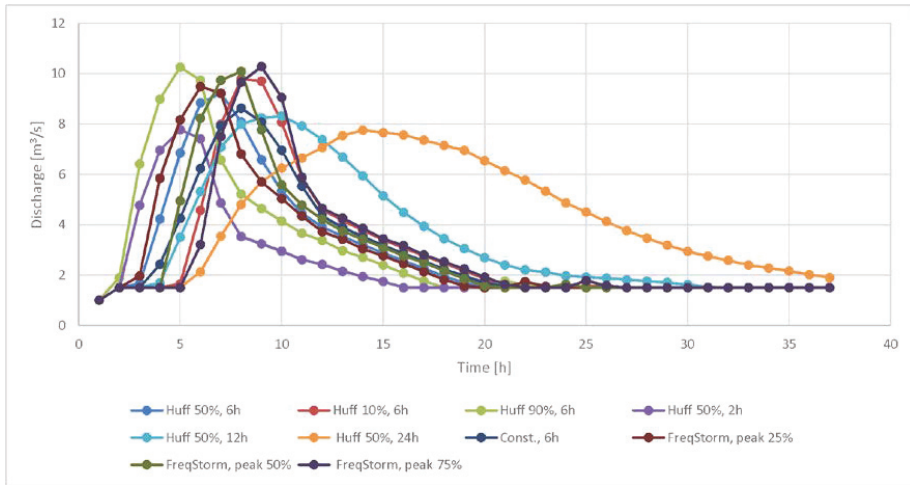


**Figure 4.** Comparison of outflow hydrographs for 10 selected scenarios for a 10-year return period.

In the next step, we compared maximum flood extents, maximum floodplain velocities, and floodplain volumes calculated from the hydraulic model simulations. Table 3 shows a comparison of these values for the 10 selected scenarios for the 10-year return period. One can notice that design rainfall selection yields more than a 35% difference in the maximum floodplain extent values (Table 3). The minimum extent of the flood was obtained using a scenario with a short rainfall duration of 2 h, and a 50% Huff curve, resulting in minimum hydrograph peak discharge. The maximum flood extent was obtained with the application of a scenario that represents a 90% Huff curve and a rainfall duration of 6 h, resulting in maximum hydrograph peak discharge. We also analysed which land-use types were flooded for these 10 scenarios, because flood damage depends on the flooded land-use types and property values (Table 4). For this purpose, a land use map of Slovenia was used [42]. The results show that the largest changes were associated with meadowland use type, which also covers the largest percent of the flooded area (Table 4). In the case of built areas, the largest extension of flooded areas ( $6.2 \times 10^3 \text{ m}^2$ ) was calculated for the 90% Huff curve (6-h rainfall duration) scenario, whereas the smallest flooding extent on the built areas ( $3.5 \times 10^3 \text{ m}^2$ ) was calculated for the 50% Huff curve (2 h rainfall duration) scenario. This also means that flood damage would be the largest for the previously mentioned scenario (Huff 90%, 6 h). For the 10-year return period, no flow was obtained for cross-sections 3 and 4, which are located on the 2D flow areas that are shown in Figure 3. This means that these areas were not flooded. Four times higher maximum water velocities were obtained for the scenario with a constant rainfall intensity of 6 h than for the scenario with a short rainfall duration of 2 h and the 50% Huff curve for cross-section 1 on the right bank of the flooded area. The water velocity has an important impact both on the stability of human body, and vehicles in the floodwater [27–30]. Similarly, also, floodplain volumes for different scenarios differ for an order of magnitude (more than 10 times) (Table 3), which indicates that the design rainfall definition has a significant impact on the simulated floodwater dynamics. Moreover, we have also compared the maximum water depths for defined scenarios for the 10-year return period (Table 5). It can be seen that the 90% Huff curve (6 h of rainfall duration) scenario yielded maximum water depth on the right and left floodplain areas

(cross-sections 1 and 2) and the 50% Huff curve (2 h of rainfall duration) scenario resulted in minimum water depths (Table 5).

**Table 3.** Comparison among maximum floodplain extents, maximum floodplain velocities, and floodplain volumes for 10 selected scenarios for the 10-year return period. Bold values indicate maximum values in each column.

Scenario	Maximum Flood Water Extent (10 <sup>3</sup> m <sup>2</sup> )	Volume of Water Flowing through Cross-Section 1 (10 <sup>3</sup> m <sup>3</sup> )	Maximum Velocities at Cross-Section 1 (m/s)	Volume of Water Flowing through Cross-Section 2 (10 <sup>3</sup> m <sup>3</sup> )	Maximum Velocities at Cross-Section 2 (m/s)
Huff 50%, 6 h	89.3	4.2	0.21	2.4	0.17
Huff 10%, 6 h	97.1	4.7	0.34	3.1	0.19
Huff 90%, 6 h	<b>101.1</b>	<b>6.7</b>	0.20	2.5	0.19
Huff 50%, 2 h	65.4	0.5	0.09	1.1	0.15
Huff 50%, 12 h	80.7	3.1	0.14	2.5	0.15
Huff 50%, 24 h	72.9	2.3	0.18	2.0	0.14
Const., 6 h	79.8	1.9	<b>0.46</b>	2.1	0.16
FreqStorm, peak 25%	92.9	4.0	0.20	2.4	<b>0.20</b>
FreqStorm, peak 50%	99.5	5.5	0.41	2.8	0.19
FreqStorm, peak 75%	100.7	5.8	0.45	3.5	0.19

**Table 4.** Area (10<sup>3</sup> m<sup>2</sup>) of flooded land use types for 10 scenarios for the 10-year return period.

Land Use/Scenario	Huff 50%, 6 h	Huff 10%, 6 h	Huff 90%, 6 h	Huff 50%, 2 h	Huff 50%, 12 h	Huff 50%, 24 h	Const., 6 h	FreqStorm, Peak 25%	FreqStorm, Peak 50%	FreqStorm, Peak 75%
Field	15.7	17.1	17.6	11.2	13.9	12.5	14.0	16.4	17.4	17.5
Meadow	55.2	60.6	63.4	38.3	49.3	43.8	48.5	57.7	62.3	63.3
Trees and bushes	1.4	1.5	1.6	1.0	1.3	1.2	1.3	1.4	1.6	1.6
Uncultivated agriculture land	0.0	0.0	0.0	0.0	0.0	0.0	0.0	0.0	0.0	0.0
Forest	0.6	0.8	0.9	0.0	0.6	0.4	0.4	0.7	0.9	0.9
Built areas	5.2	5.8	6.2	3.5	4.3	3.7	4.4	5.4	6.0	6.1
Water	11.3	11.3	11.3	11.3	11.3	11.3	11.3	11.3	11.3	11.3

**Table 5.** Comparison of maximum water depths for cross-sections 1 and 2 for different scenarios for the 10-year return period.

Scenario	Maximum Water Depth at Cross-Section 1 (m)	Maximum Water Depth at Cross-Section 2 (m)
Huff 50%, 6 h	0.25	0.49
Huff 10%, 6 h	0.30	0.56
Huff 90%, 6 h	0.33	0.59
Huff 50%, 2 h	0.11	0.26
Huff 50%, 12 h	0.22	0.47
Huff 50%, 24 h	0.18	0.39
Const., 6 h	0.20	0.41
FreqStorm, peak 25%	0.28	0.51
FreqStorm, peak 50%	0.32	0.57
FreqStorm, peak 75%	0.33	0.59

### 3.2. 100-Year Return Period Event

We have also applied all 10 scenarios for the 100-year return period. Figure 5 shows a comparison of outflow hydrographs for the considered scenarios for the 100-year return period. Compared to the 10-year event (Figure 4), higher peak discharge values were obtained for all of the scenarios, as expected (Figure 5). Similarly, as for the 10-year return period, the maximum peak discharge value was obtained for the scenario using the frequency storm method, with a peak intensity position at 75% of the rainfall duration. On the other hand, the smallest peak discharge value was calculated for scenario based on the 50% Huff curve and 24 h of rainfall duration. Table 6 shows a comparison among the maximum floodplain water extents for investigated cases. The scenario based on the frequency

storm method and a peak position at 75% yielded a floodplain extent that was about twice as large as the scenario that used the 50% Huff curve and 24 h of rainfall duration (Table 6). This means that the difference in the peak discharge value for a factor of 1.4 can result in a floodplain water extent that is more than twice as large (Figure 5 and Table 6). Figure 6 shows a comparison between the scenarios that caused the minimum and maximum floodplain extent for the 100-year return period. We also compared the volume of water flowing through cross-sections 1–4 (Figure 3), and the maximum water velocities through these cross-sections (Tables 6 and 7). The maximum floodplain water velocities exceed 1.2 m/s, and the differences among the maximum water velocities were more than 10 times for some of the scenarios (Table 7). Similar conclusions can also be made for the volume of water flowing through the different floodplain cross-sections (Tables 6 and 7). Table 8 shows which land use types were flooded during all of the considered scenarios for the 100-year return period. Similarly, as for the 10-year return period, the largest percentage of the flooded area was meadows. For the built areas, the largest extension of flooded areas ( $22.4 \times 10^3 \text{ m}^2$ ) was calculated for the FreqStorm, peak 75% scenario, whereas the smallest flooding extent over the built areas ( $8.1 \times 10^3 \text{ m}^2$ ) was calculated for the Huff 50%, 24-h scenario. Differences in the design rainfall resulted in a changed extension of the flooded built areas by a factor of 2.8. This poses huge uncertainty in predictions of the maximum flood extent (e.g., for a decision-maker). Further, the uncertainty in flood extent makes it difficult to assess potential flood damages (e.g., by using depth–damage curves), or plan future changes in land use in the flood hazard areas. Moreover, Table 9 shows a comparison between the maximum water depths for different scenarios for the 100-year return period. While the difference between the maximum and minimum water levels at the selected cross-sections seems small (in the range of 6–8 cm), it is well known that small changes in the shallow overflowing depth in urban areas can considerably increase the direct and indirect damage on buildings and urban infrastructure [43]. A review of flood damage studies revealed that that the variation in flood damage to properties could not be explained by inundation depth alone, and should be combined with other factors [44], such as water flow velocity. However, the results of our study show that the water velocities at the selected flood plain cross-sections can vary by a factor of 10.

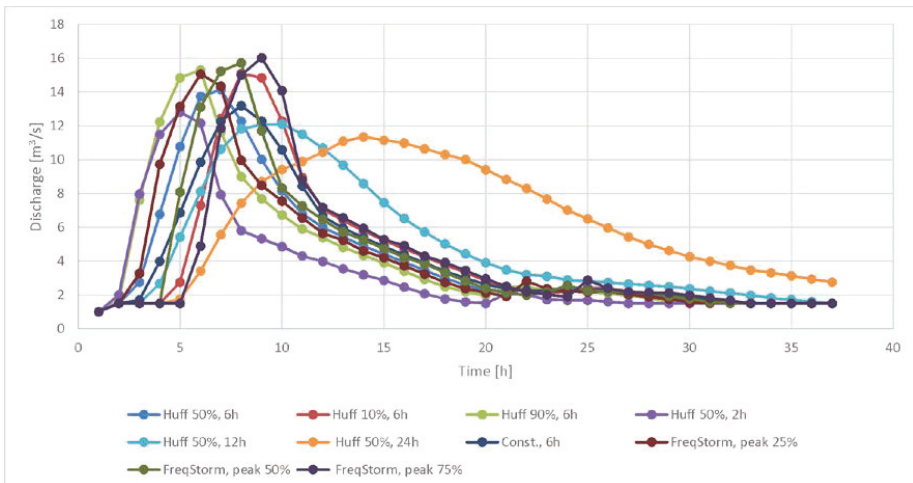


**Figure 5.** Comparison of outflow hydrographs for the 10 selected scenarios for the 100-year return period.



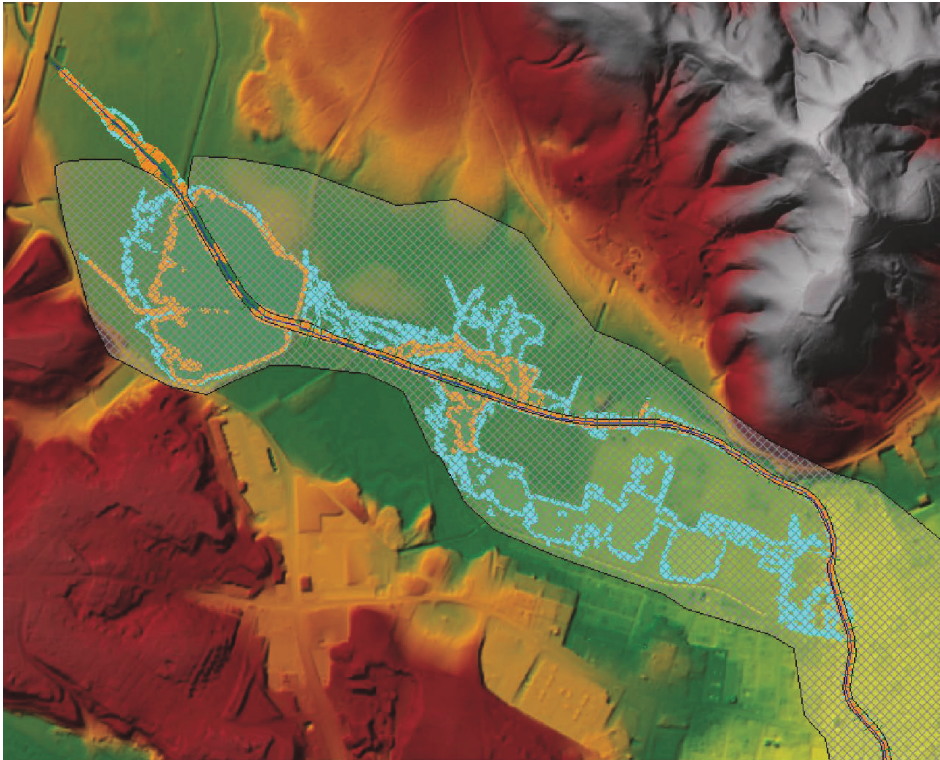


**Figure 6.** Comparison between the maximum floodplain extent for scenarios (vi) and (x) indicated with orange and light blue, respectively, for the 100-year return period.

**Table 9.** Comparison of maximum water depths for cross-sections 1 and 2 for different scenarios for the 100-year return period.

Scenario	Maximum Water Depth at Cross-Section 1 (m)	Maximum Water Depth at Cross-Section 2 (m)
Huff 50%, 6 h	0.52	0.80
Huff 10%, 6 h	0.57	0.84
Huff 90%, 6 h	0.57	0.85
Huff 50%, 2 h	0.46	0.75
Huff 50%, 12 h	0.47	0.75
Huff 50%, 24 h	0.45	0.73
Const., 6 h	0.49	0.77
FreqStorm, peak 25%	0.57	0.84
FreqStorm, peak 50%	0.60	0.86
FreqStorm, peak 75%	0.60	0.86

#### 4. Conclusions

This study presents combined hydrological and hydraulic modelling results for the Glinščica Stream catchment in Slovenia, which can be regarded as a small-scale catchment (less than 20 km<sup>2</sup>) that is ungauged in terms of discharges. This means that approaches suitable for ungauged catchments are the only option in order to derive design hydrographs, and more specifically design peak discharge values. This study evaluates 10 different design rainfall events (scenarios) that were used as input to the

hydrological model. Both 10 and 100-year return period events were analysed. By using calibrated and validated hydrological models, the inputs for the hydraulic model were determined. Thus, the main aim was to evaluate the influence of the design rainfall selection in terms of the rainfall duration and temporal rainfall distribution defined using Huff curves on the hydraulic modelling results (e.g., shape of the outflow hydrograph, peak discharge values, floodplain water extents, maximum floodplain water velocities, and maximum water depths).

The 10 selected and considered scenarios in the study show that the maximum peak discharge value using different design hyetographs and rainfall durations can be 1.4 times larger than the minimum peak discharge value. At the same time, the maximum floodplain extent can be two times larger than the minimum flood extent, and the maximum floodplain water velocity can be 10 times larger than the minimum floodplain velocity scenarios. This means that design rainfall definition can significantly influence the hydraulic modelling results.

Thus, we recommend that the selection of the design rainfall event should be selected with care, and with the consideration of the typical temporal rainfall distribution of the region, which can be described using the Huff curves. Moreover, in order to select the crucial rainfall duration, an analysis of the past flood events could be useful, with the aim of identifying rainfall characteristics that can result in an extreme flood event, such as duration. In combination with the catchment time of concentration, this could be used to select the rainfall duration.

**Acknowledgments:** The results of the study are part of the Slovenian national research project J2-7322: "Modelling hydrologic response of nonhomogeneous catchments" and research Programme P2-0180: "Water Science and Technology, and Geotechnical Engineering: Tools and Methods for Process Analyses and Simulations, and Development of Technologies" that are financed by the Slovenian Research Agency (ARRS). We wish to thank the Slovenian Environment Agency (ARSO) for data provision.

**Author Contributions:** All authors drafted the manuscript and determined the aims of the research; N. Bezak carried out the hydrological and hydraulic calculations; All authors contributed to the manuscript writing and revision.

## References

1. Zorn, M.; Komac, B. Damage caused by natural disasters in Slovenia and globally between 1995 and 2010. *Acta Geogr. Slov.* **2011**, *51*, 7–30. [CrossRef]
2. Blöschl, G.; Hall, J.; Parajka, J.; Perdigao, R.A.P.; Merz, B.; Arheimer, B.; Aronica, G.T.; Bilibashi, A.; Bonacci, O.; Borga, M.; et al. Changing climate shifts timing of European floods. *Science* **2017**, *357*, 588–590. [CrossRef] [PubMed]
3. Šraj, M.; Menih, M.; Bezak, N. Climate variability impact assessment on the flood risk in Slovenia. *Phys. Geogr.* **2016**, *37*, 73–87. [CrossRef]
4. Blöschl, G. Recent advances in flood hydrology—Contributions to implementing the Flood Directive. *Acta Hydrotech.* **2016**, *29*, 13–22.
5. Bezak, N.; Brilly, M.; Šraj, M. Comparison between the peaks-over-threshold method and the annual maximum method for flood frequency analysis. *Hydrol. Sci. J.* **2014**, *59*, 959–977. [CrossRef]
6. Šraj, M.; Bezak, N.; Brilly, M. Bivariate flood frequency analysis using the copula function: A case study of the Litija station on the Sava River. *Hydrol. Process.* **2015**, *29*, 225–238. [CrossRef]
7. Blöschl, G.; Sivapalan, M.; Wagener, T.; Viglione, A.; Savenije, H. *Runoff Prediction in Ungauged Basins: Synthesis across Processes, Places and Scales*, 1st ed.; Cambridge University Press: Cambridge, UK, 2013; 490p.
8. Bezak, N.; Šraj, M.; Mikoš, M. Design rainfall in engineering applications with focus on the design discharge. In *Engineering and Mathematical Topics in Rainfall*; InTech Press: London, UK, 2018; ISBN 978-953-51-5562-1.
9. Grimaldi, S.; Petroselli, A.; Serinaldi, F. A continuous simulation model for design-hydrograph estimation in small and ungauged watersheds. *Hydrol. Sci. J.* **2012**, *57*, 1035–1051. [CrossRef]
10. El-Jabi, N.; Sarraf, S. Effect of maximum rainfall position on rainfall-runoff relationship. *J. Hydraul. Eng.* **1991**, *117*, 681–685. [CrossRef]

11. Ball, J.E. The influence of storm temporal patterns on catchment response. *J. Hydrol.* **1994**, *158*, 285–303. [CrossRef]
12. Singh, V.P. Effect of spatial and temporal variability in rainfall and watershed characteristics on stream flow hydrograph. *Hydrol. Process.* **1997**, *11*, 1649–1669. [CrossRef]
13. Danil, E.I.; Michas, S.N.; Lazaridis, L.S. Hydrologic modeling for the determination of design discharges in ungauged basins. *Glob. NEST J.* **2005**, *7*, 296–305.
14. Šraj, M.; Dirnbek, L.; Brilly, M. The influence of effective rainfall on modeled runoff hydrograph. *J. Hydrol. Hydromech.* **2010**, *58*, 3–14. [CrossRef]
15. Sikoroska, A.E.; Seibert, J. Appropriate temporal resolution of precipitation data for discharge modelling in pre-alpine catchments. *Hydrol. Sci. J.* **2017**, *63*. [CrossRef]
16. Sikoroska, A.E.; Viviroli, D.; Seibert, J. Effective precipitation duration for runoff peaks based on catchment modelling. *J. Hydrol.* **2017**, *556*, 510–522. [CrossRef]
17. Alfieri, L.; Laio, F.; Claps, P. A simulation experiment for optimal design hyetograph selection. *Hydrol. Process.* **2008**, *22*, 813–820. [CrossRef]
18. Huff, F.A. Time distribution of rainfall in heavy storms. *Water Resour. Res.* **1967**, *3*, 1007–1019. [CrossRef]
19. Bonta, J.V. Development and utility of Huff curves for disaggregating precipitation amounts. *Appl. Eng. Agric.* **2004**, *20*, 641–653. [CrossRef]
20. Azli, M.; Rao, R. Development of Huff curves for Peninsular Malaysia. *J. Hydrol.* **2010**, *388*, 77–84. [CrossRef]
21. Dolšak, D.; Bezak, N.; Šraj, M. Temporal characteristics of rainfall events under three climate types in Slovenia. *J. Hydrol.* **2016**, *541*, 1395–1405. [CrossRef]
22. Huff, F. *Time Distributions of Heavy Rainstorms in Illinois*; Illinois State Water Survey, State of Illinois Department of Energy and Natural Resources: Champaign, IL, USA, 1990; Circular 173.
23. Savage, J.T.S.; Pianosi, F.; Bates, P.; Freer, J.; Wagener, T. Quantifying the importance of spatial resolution and other factors through global sensitivity analysis of a flood inundation model. *Water Resour. Res.* **2016**, *52*, 9146–9163. [CrossRef]
24. Hall, J.W.; Tarantola, S.; Bates, P.D.; Horritt, M.S. Distributed sensitivity analysis of flood inundation model calibration. *J. Hydraul. Eng.* **2005**, *131*, 117–126. [CrossRef]
25. Pestotnik, S.; Hojnik, T.; Šraj, M. Analysis of the possibility of using the distributed two-dimensional model Flo-2D for hydrological modeling. *Acta Hydrotech.* **2012**, *25*, 85–103.
26. Pappenberger, F.; Matgen, P.; Beven, K.J.; Henry, J.B.; Pfister, L.; de Fraipont, P. Influence of uncertain boundary conditions and model structure on flood inundation predictions. *Adv. Water Resour.* **2006**, *29*, 1430–1449. [CrossRef]
27. Shu, C.W.; Xia, J.Q.; Falconer, R.A.; Lin, B.L. Incipient velocity for partially submerged vehicles in floodwaters. *J. Hydraul. Res.* **2011**, *49*, 709–717. [CrossRef]
28. Xia, J.Q.; Falconer, R.A.; Wang, Y.J.; Xiao, X.W. New criterion for the stability of a human body in floodwaters. *J. Hydraul. Res.* **2014**, *52*, 93–104. [CrossRef]
29. Milanesi, L.; Pilotti, M.; Ranzi, R. A conceptual model of people's vulnerability to floods. *Water Resour. Res.* **2015**, *51*, 182–197. [CrossRef]
30. Milanesi, L.; Pilotti, M.; Bacchi, B. Using web-based observations to identify thresholds of a person's stability in a flow. *Water Resour. Res.* **2016**, *52*, 7793–7805. [CrossRef]
31. Kreibich, H.; Piroth, K.; Seifert, I.; Maiwald, H.; Kunert, U.; Schwarz, J.; Merz, B.; Thieken, A.H. Is flow velocity a significant parameter in flood damage modelling? *Nat. Hazards Earth Syst. Sci.* **2009**, *9*, 1679–1692. [CrossRef]
32. Hagemeyer-Klose, M.; Wagner, K. Evaluation of flood hazard maps in print and web mapping services as information tools in flood risk communication. *Nat. Hazards Earth Syst. Sci.* **2009**, *9*, 563–574. [CrossRef]
33. Tacnet, J.-M.; Batton-Hubert, M.; Dezert, J. Information fusion for natural hazards in mountains. In *Advances and Applications of DSMT for Information Fusion*; Smarandache, F., Dezert, J., Eds.; American Research Press: Rehoboth, DE, USA, 2009; Chapter 23, Volume III, pp. 565–659.
34. Tacnet, J.-M.; Batton-Hubert, M.; Dezert, J.; Richard, D. Decision Support Tools for Natural Hazards Management under Uncertainty. In Proceedings of the 12th Congress Interpraevent, Grenoble, France, 23–26 April 2012; pp. 597–608. Available online: [http://www.interpraevent.at/palm-cms/upload\\_files/Publikationen/Tagungsbeitraege/2012\\_1\\_597.pdf](http://www.interpraevent.at/palm-cms/upload_files/Publikationen/Tagungsbeitraege/2012_1_597.pdf) (accessed on 11 February 2018).

35. Bezak, N.; Šraj, M.; Rusjan, S.; Kogoj, M.; Vidmar, A.; Sečnik, M.; Brilly, M.; Mikoš, M. Comparison between two adjacent experimental torrential watersheds: Kuzlovec and Mačkov graben. *Acta Hydrotech.* **2013**, *26*, 85–97.
36. Šraj, M.; Bezak, N.; Rusjan, S.; Mikoš, M. Review of hydrological studies contributing to the advancement of hydrological sciences in Slovenia. *Acta Hydrotech.* **2016**, *29*, 47–71.
37. Brilly, M.; Rusjan, S.; Vidmar, A. Monitoring the impact of urbanisation on the Glinscica stream. *Phys. Chem. Earth Part A/B/C* **2006**, *31*, 1089–1096. [CrossRef]
38. Rusjan, S.; Fazarinc, R.; Mikoš, M. River rehabilitation of urban watercourses on the example of the Glinščica River in Ljubljana. *Acta Hydrotech.* **2003**, *21*, 1–22.
39. HEC-HMS 3.4. Reference Manual. Available online: [http://www.hec.usace.army.mil/software/hec-hms/documentation/HEC-HMS\\_Users\\_Manual\\_3.4.pdf](http://www.hec.usace.army.mil/software/hec-hms/documentation/HEC-HMS_Users_Manual_3.4.pdf) (accessed on 11 February 2018).
40. HEC-RAS 5.0. Reference Manual. Available online: <http://www.hec.usace.army.mil/software/hec-ras/documentation/HEC-RAS%205.0%20Reference%20Manual.pdf> (accessed on 11 February 2018).
41. Nguyen, T.A.; Grossi, G.; Ranzi, R. Design Storm for Mixed Urban and Agricultural Drainage Systems in the Northern Delta in Vietnam. *J. Irrig. Drain. Eng.* **2016**, *142*, 4015051. [CrossRef]
42. GERK. Land Use Map of Slovenia. Available online: <http://rkg.gov.si/GERK/> (accessed on 11 February 2018).
43. Penning-Rowsell, E.; Johnson, C.; Tunstall, S.; Tapsell, S.; Morris, J.; Chatterton, J.B.; Green, C. *The Benefits of Flood and Coastal Risk Management: A Manual of Assessment Techniques*; Middlesex University Press: London, UK, 2005.
44. Hammond, M.J.; Chen, A.S.; Djordjević, S.; Butler, D.; Mark, O. Urban flood impact assessment: A state-of-the-art review. *Urban Water J.* **2015**, *12*, 14–29. [CrossRef]

# Modelling the Present and Future Water Level and Discharge of the Tidal Betna River

M. M. Majedul Islam <sup>1,\*</sup>, Nynke Hofstra <sup>1</sup> and Ekaterina Sokolova <sup>2</sup>

<sup>1</sup> Environmental Systems Analysis Group, Wageningen University and Research, 6708 PB Wageningen, The Netherlands; nynke.hofstra@wur.nl

<sup>2</sup> Department of Architecture and Civil Engineering, Chalmers University of Technology, 412 58 Gothenburg, Sweden; ekaterina.sokolova@chalmers.se

\* Correspondence: majed25bd@gmail.com

**Abstract:** Climate change, comprising of changes in precipitation patterns, higher temperatures and sea level rises, increases the likelihood of future flooding in the Betna River basin, Bangladesh. Hydrodynamic modelling was performed to simulate the present and future water level and discharge for different scenarios using bias-corrected, downscaled data from two general circulation models. The modelling results indicated that, compared to the baseline year (2014–2015), the water level is expected to increase by 11–16% by the 2040s and 14–23% by the 2090s, and the monsoon daily maximum discharge is expected to increase by up to 13% by the 2040s and 21% by the 2090s. Sea level rise is mostly responsible for the increase in water level. The duration of water level exceedance of the established danger threshold and extreme discharge events can increase by up to half a month by the 2040s and above one month by the 2090s. The combined influence of the increased water level and discharge has the potential to cause major floods in the Betna River basin. The results of our study increase the knowledge base on climate change influence on water level and discharge at a local scale. This is valuable for water managers in flood-risk mitigation and water management.

**Keywords:** flood; precipitation; water level; discharge; General Circulation Models (GCM); MIKE 21 FM model

---

## 1. Introduction

Floods often cause devastating effects on human life and properties worldwide. Climate change increases floods because of change in precipitation patterns and sea level rise (SLR) [1]. Bangladesh is extremely vulnerable to the impacts of climate change because of its low and flat terrain, high population density, high poverty levels, and the reliance of many livelihoods on climate-sensitive sectors [2]. The Betna River basin in the southwest of Bangladesh has been experiencing both fluvial flooding due to extreme precipitation during the monsoon and storm surge flooding due to cyclones originating from the Bay of Bengal. Floods hit this area almost every year of the last decade, causing loss of life and economic damage [3].

Increased precipitation and flooding cause increased runoff that brings pollution from the land into the river. Outbreaks of waterborne diseases, such as diarrhoea, are very common after flooding events [3] and cause serious public health risks in this area [4]. More frequent and intense flooding is likely to occur in this area in the future due to climate change and SLR [5]. Therefore, the impact of flooding could well become more severe, particularly due to the low lying areas, high population density, inadequate flood protection infrastructure, low level of social development, and high dependence on agriculture [4].

The fifth assessment report (AR5) of the Intergovernmental Panel on Climate Change [6] concluded that the projected adverse impacts of climate change on deltas would be mainly due to floods

associated with extreme precipitation, increases in temperature and SLR. The future precipitation in Bangladesh is expected to increase between 5 and 20%, and average temperature is expected to increase between 2 and 4 °C by 2100 [7]. Trend analysis of SLR along the southwest coast of Bangladesh shows an annual increase of 5.5 mm based on tidal gauge record during 1977–1998 [8]. Although the impact of extreme precipitation and SLR on flood risks is substantial, current water management practices are not robust enough to cope with climate change consequences. The information about present climate variability and future climate scenarios needs to be better incorporated into planning and management of water bodies [8].

Process-based modelling is often performed to understand hydrodynamics of a basin and to assess the effectiveness of future flood protection infrastructure [9,10]. Several modelling and climate change studies were performed for South-Asian river basins [11–14]. These studies were mainly based on two climate change variables (temperature and precipitation) and reported that increases in future floods are very likely in this region, since increased temperatures and monsoon precipitation will likely impact river flows. However, in-depth studies on assessing combined impact of climate change and SLR on river hydrodynamics are lacking. Moreover, most of the climate change studies have been conducted in large or regional river basins like the Ganges, Brahmaputra and Meghna (GBM) River systems of India and Bangladesh [9,11–13]. No such studies have been performed for a relatively small basin; thus, the influence of climate change on water levels and discharge at the local scale remains unclear. Our study on the Betna River basin reduces this knowledge gap. The Betna River basin was selected for this study since it floods almost every year due to combined effects of extreme precipitation, storm surges and SLR. Moreover, the diversified water uses in the area (e.g., domestic, irrigation, shellfish growing, and bathing) require adequate water management.

The aim of the study was to assess the present and future water level and discharge in the Betna River. This was achieved by applying a process-based hydrodynamic model (MIKE 21 FM) to simulate water level and discharge under different future climate conditions. The MIKE 21 FM model for the Betna River was set up, calibrated and validated using the observed water level and discharge data. The model was then used to project the future (2040s and 2090s) water level and discharge. The output of this study is likely helpful in addressing frequent and intense flooding induced by climate change in the study area. The findings and model can be transformed to other basins of the world with similar characteristics.

## 2. Materials and Methods

### 2.1. Study Area

The study area covers an area of 10,706 hectares in the Betna River basin, located in the Satkhira district of southwest Bangladesh. The river has a total length of about 192 km with an average width of 125 m. The study focused on approximately 30 km of the downstream part of the river (Figure 1); the upper part of the river was not included in the model, since it becomes almost dry during dry months. The river is hydrologically connected with the Bhairab River near the Jessore district in the north and the Kholpetua River near Assasuni of the Satkhira district in the south. The Betna River has tidal influence, which is the predominant factor for its sustainability, because during the dry season the fresh water inflow from upstream areas becomes very limited. The tide generates from the Bay of Bengal and propagates to the north until the upstream boundary of the study area. Like most coastal areas in Bangladesh, this study area is governed by the semidiurnal tide. The usual range of fluctuation of the water level is 0.7 m during neap tide and 3.0 m during spring tide [15].

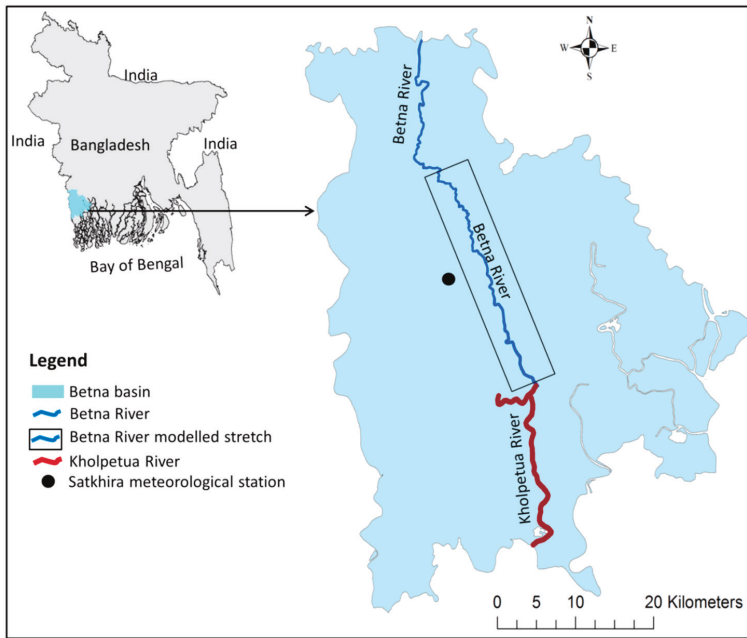


Figure 1. Study area, the Betna River basin in the southwest of Bangladesh.

The study area has a rainy season (monsoon) during June–September, followed by a cool and dry period during October–February and a hot season with frequent cyclones (pre-monsoon) during March–May. Mean annual rainfall in the area is about 1800 mm, of which approximately 70% occurs during the monsoon season [15]. This area is affected by inland flooding due to heavy incessant rainfall during the monsoon in August–September and by storm surge flooding during cyclone season in April–May [3,16]. Relative humidity of the area varies from about 70% in March to 90% in July. Mean annual air temperature is 26 °C with peaks of around 35 °C in May–June. Temperature in winter may fall to 10 °C in January [15]. Wind in the region shows two dominant patterns, i.e., south-westerly monsoon wind during June–September and north-easterly wind during November–February. Other months show no distinct wind direction pattern.

The study area is mainly a flat terrain with some low-lying depressions and many tidal channels and creeks that crisscross the area. The soils are mostly clay and loam. Land use is dominated by paddy cultivation and shrimp culture. About 8% of the total area is homesteads and settlements, about 10% is water bodies, 61% is agriculture and the remainder is wetlands used for aquaculture or integrated paddy shrimp culture [3,17].

## 2.2. Hydrodynamic Model Set Up

The two dimensional (2D) hydrodynamic model MIKE 21 FM [18] was applied to simulate future water level and discharge in the Betna River. This model was selected because it can simulate the hydrodynamic situation in a tidal river and generate outputs of high temporal and spatial resolution. The 2D model was used because the river is not very deep (maximum depth 9 m), and vertical mixing happens fast. The model simulates unsteady 2D flows in one vertically homogenous (depth averaged) layer and assumes that large flow gradients are absent in the vertical direction of the water column [1].

The hydrodynamic (HD) module of MIKE 21 FM simulates variations of water level and flows in response to several forcing functions on a rectangular or triangular grid of the study area when provided

with the bathymetry, bed resistance coefficients, forcings and boundary conditions [19]. The model is based on a 2D numerical solution of Reynolds averaged Navier–Stokes equations. In the model, the Boussinesq simplifying approximation is used, and hydrostatic pressure is assumed [18]. The 2D model consists of vertically integrated momentum equations, continuity equation, advection-diffusion equations for temperature and salinity, and equation of state. The water density depends on temperature and salinity only [18]. The input and validation data required for the modelling process are river bathymetry, hydrodynamic and meteorological data. The detailed description of the model and the governing equations are presented in Danish Hydraulic Institute (DHI) [18] and Uddin et al. [19].

2.3. Bathymetric Survey and Mesh Generation

Modelling Bangladeshi river basins, including the Betna River, is difficult due to the scarcity of data. However, a comprehensive data collection survey was carried out in the Betna River system by the Institute of Water Modelling (IWM), Bangladesh, in 2012 to collect primary data, such as river bathymetry, water level and discharge. The distance between the surveyed river cross-sections varied from 400 to 500 m. The depth data were referred to meter Public Works Datum (mPWD) of Bangladesh (which is 0.46 m below mean sea level) using water level observed at the gauges within the survey area [15].

Mesh generation was done using the MIKE Zero mesh generator (Figure 2). A flexible mesh size with triangular elements was used, and the triangulation was performed with delaunay triangulation [18]. The mesh size was decreased and resolution increased where the river is narrow. The mesh consists of 4089 nodes and 6628 elements. The smallest element area is 42.5 m<sup>2</sup> and the largest area is approximately 498 m<sup>2</sup>. In the modelling domain, intertidal zones were flooded and dried during every tidal phase to mimic natural conditions. The river is connected with some small drains, which have no water flow during dry weather and were thus considered as the land boundary in the model. However, during wet weather, stormwater runoff through the drains were included as a source in the model: four main drains were considered in the model. The runoff volume was estimated applying the runoff curve number method developed by the US Department of Agriculture [20].

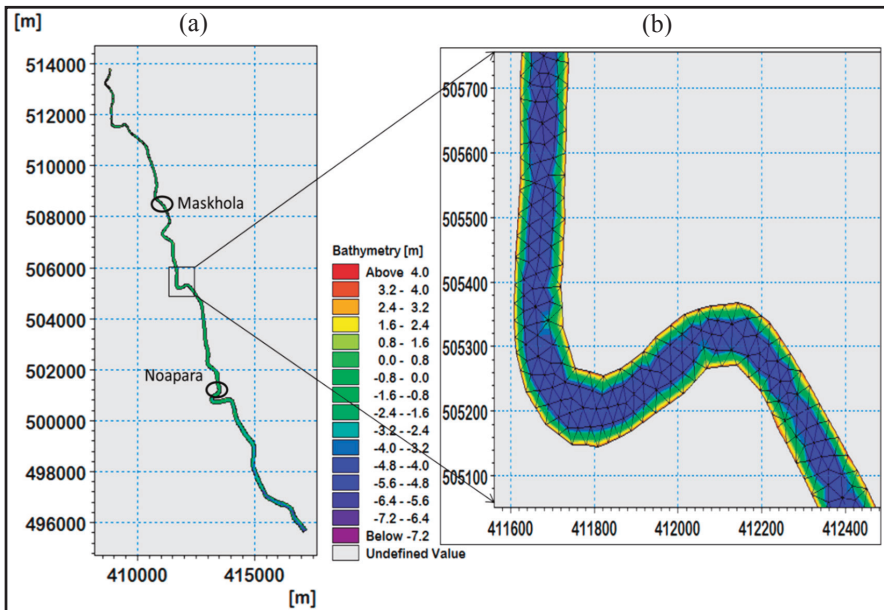


Figure 2. Bathymetry (a) and mesh (b) for the hydrodynamic model of the Betna River.

#### 2.4. Meteorological and Hydrodynamic Data

Precipitation, wind speed and direction, air temperature (maximum and minimum) and relative humidity data were collected from the Satkhira meteorological station (Figure 1, Table 1). To calibrate the hydrodynamic model, water level and river discharge data were collected from IWM (Table 1). Water level data were collected with 0.5 h interval at three locations (Maskhola, Noapara and the downstream boundary, (Figure 2) along the Betna River from 1 August to 10 October 2012. The observed minimum and maximum water levels at Maskhola and Noapara in the Betna River were 1.55 and 3.48 mPWD, and  $-2.10$  and  $3.50$  mPWD, respectively. Discharge measurements were carried out near Noapara (Figure 2) and the upper boundary by IWM in September 2012 for 13 h with 0.5 h interval both in spring and neap tide. The observed maximum discharge at Noapara during spring tide was  $277$  and  $392$  m<sup>3</sup>/s at the time of ebbing and flooding, respectively. For the baseline simulation, water level and discharge data were gathered from the Bangladesh Water Development Board (BWDB) for the period 2014–2015 (Table 1).

**Table 1.** Input data used for the hydrodynamic model.

Data Type	Resolution	Period	Location	Source
River bathymetry	Cross-section 400–500 m	2012	Modelled stretch	IWM <sup>a</sup>
Water level for calibration period	0.5 h	2012	Maskhola, Noapara and lower boundary	IWM <sup>a</sup>
Water level for validation period	3 h	2014–2015	Near Noapara and lower boundary	BWDB <sup>b</sup>
Discharge for calibration period	0.5 h	2012	Near Noapara and upper boundary	IWM <sup>a</sup>
Discharge for validation period	1 week	2014–2015	Near upper boundary	BWDB <sup>b</sup>
Precipitation	1 day	2012–2015	BMD Satkhira	BMD <sup>c</sup>
Air temperature	1 day	2012–2015	BMD Satkhira	BMD <sup>c</sup>
Wind speed and direction	3 h	2012–2015	BMD Satkhira	BMD <sup>c</sup>
Relative humidity	1 day	2012–2015	BMD Satkhira	BMD <sup>c</sup>

<sup>a</sup> Institute of Water Modelling, Bangladesh; <sup>b</sup> Bangladesh Water Development Board; <sup>c</sup> Bangladesh Meteorological Department.

The boundary conditions were described using time-series for discharge and water level at the upstream and downstream boundaries, respectively. The initial conditions were specified using the measured data for water level, and initial water velocity was set to zero. The flooding depth 0.05 m, drying depth 0.005 m and wetting depth 0.1 m were set in the model. In the model, a constant horizontal eddy viscosity (0.28 m<sup>2</sup>/s), a constant clearness coefficient (70%), and default parameterisation (Table 2) for heat exchange were used. The model by default calculates evapotranspiration using air and water temperature data.

**Table 2.** Parameter values used in the hydrodynamic modeling.

Parameter Type	Formulation	Calibrated Value	Note
Horizontal eddy viscosity	Smagorinsky formulation		Selected after multiple simulations where different values were tested.
	Constant value	0.28 m <sup>2</sup> /s	
	Range	$1.8 \times 10^{-06}$ – $1.0 \times 10^8$ m <sup>2</sup> /s	
Vertical eddy viscosity	<i>k</i> -epsilon formulation		
	Range	$1.0 \times 10^{-07}$ – $2.0 \times 10^{-04}$ m <sup>2</sup> /s	
Bed roughness	Roughness height		
	Constant value	60 m <sup>1/3</sup> /s	
Wind friction	Constant value	0.001255	
Heat exchange	Constant in Dalton's law	0.5	
	Wind coefficient in Dalton's law	0.9	
	Sun constant, "a" in Ångström's law	0.176	
	Sun constant, "b" in Ångström's law	0.37	
Light intensity	Light extinction coefficient	0.5	

### 2.5. Calibration, Validation and Sensitivity Analysis

The model was calibrated by adjusting the parameter values (Table 2) to obtain output results that match measured data. After calibration the modeled and measured values of water level and discharge were compared at Maskhola and Noapara. The calibration period from 26 August to 15 September 2012 was selected because the bathymetric survey and measurements of hydrodynamics were conducted in that period. The calibration period covers the important monsoon period, when floods occur, and hydrodynamic variability is higher. A sensitivity analysis was also performed to estimate the rate of change in model output with respect to change in model inputs. The sensitivity analysis was performed by changing the following model inputs and parameters: water level and discharge at the model boundaries, water velocity, river bed roughness, wind speed, eddy viscosity, clearness coefficient, and heat exchange rate. The calibrated model was then applied to simulate water level and discharge for a typical year October 2014 to September 2015 to represent the baseline conditions.

The model output for the baseline year was validated using the measured water level. The model performance was assessed using two statistical parameters: coefficient of determination ( $R^2$ ) and the Nash-Sutcliffe efficiency (NSE). Generally, model performances are called satisfactory if  $R^2 > 0.60$  and  $NSE > 0.50$ ; the closer the model efficiency is to 1, the more accurate the model is [21]. After validation, the model was applied to predict future water level and discharge under climate change situation.

### 2.6. Future Scenario Development

There are many General Circulation Models (GCMs) that describe past, present and future changes in climate on a global scale. With the help of GCMs, variations in surface air temperature, precipitation and sea level were computed; and the output from individual GCMs and averages of future climate conditions can be applied in climate change impact analysis [22]. In the current study, outputs from GCMs used in the fifth phase of the Climate Model Intercomparison Project (CMIP5) were used. CMIP5 was utilised by the IPCC in AR5 [23]. In IPCC AR5, four Representative Concentration Pathways (RCPs) were used for climate change projections [6]. In the current study, a relatively low emission pathway (RCP 4.5) and a high emission pathway (RCP 8.5) were used. Two GCMs, MPI-ESM-LR (Max Planck Institute for Meteorology) and IPSL-CM5A-LR (Institute Pierre-Simon Laplace), were used. These models were selected, since they have been used widely in this region and best represent precipitation and surface air temperature for this study area [8].

At first, the CMIP5 daily climatic data for both GCMs and RCPs were downloaded from the Earth System Grid Federation Portal (<http://cmip-pcmdi.llnl.gov/cmip5/>; <https://esgf-data.dkrz.de/search/cmip5/>). Then, the daily GCM data were downscaled and bias corrected using the "Delta method" with "quantile-quantile" correction, as described by Liu, Hofstra [24]. This is a relative change method, which is widely used in bias correction and downscaling GCM data with different grid size. The GCM's gridded data have less variability and less local characteristics than the point input required for the model. Taking into account local variability is important for climate change impact studies, specifically in the case of a small river basin. This requires a downscaling method that generates point data from gridded data. The delta change method can efficiently produce point data [24]. The method includes quantile-quantile correction to ensure that extreme events become more extreme in the future climate data. In this study, daily observed air temperature and precipitation data from 1986 to 2005 were used as a basis for this downscaling. Two future time periods, 2031–2050 (2040s) and 2081–2100 (2090s), were considered for the two RCPs.

To project future precipitation, a 20-year average total monthly precipitation was computed for the observed and future downscaled data. Then, the percentage change between future and observed data was calculated for each month. The daily observed precipitation data for the baseline year 2014–2015 were modified by this percentage change and subsequently used as model input for the simulation of future hydrodynamic conditions. Fresh water inflow from upstream Gorai River basin areas were on average projected to increase during the monsoon period (driven primarily by increased

basin precipitation) by 9% [25] and decrease during dry periods by 6% [4] by the 2050s. Similar change was assumed for the 2090s. These changes in discharge values along with the precipitation percentage changes were used to modify the observed current discharge data. The resulting discharge data were used to define the upstream boundary conditions in simulations for future prediction. The future stormwater runoff was estimated by the curve number method [20] using future precipitation data. For air temperature, daily average values were used.

SLR combined with the RCP scenarios was used to investigate the impact of climate change on the hydrodynamic characteristics of the Betna River. For RCP 4.5, the estimated global mean SLR is 0.24 and 0.4 m for the time horizons 2040s and 2090s respectively, relative to the average sea level for 1986–2005. For RCP 8.5, the estimated global mean SLR is 0.3 and 0.63 m for the time horizons 2040s and 2090s respectively [26]. Recent projections from the IPCC AR5 suggest that sea level in the northern Bay of Bengal (close to the study area) may rise between 0.1 and 0.3 m by 2050 and between 0.3 and 0.6 m by 2100, relative to the baseline period 1991–2010, without including local effects, such as land subsidence [27]. Based on these studies, the annual SLR for the study area was estimated. This estimated SLR and the annual land subsidence of 2.5 mm [27,28] together lead to the estimated relative mean SLR of 0.26 and 0.42 m for RCP 4.5, and of 0.44 and 0.76 m for RCP 8.5 for the 2040s and 2090s, respectively. These SLR values were added to the observed water level data to define the downstream boundary conditions in simulations for future prediction. Finally, the model was applied to simulate future (for the 2040s and 2090s) water level and discharge, and the results were compared with the modelling results for the baseline year (2014–2015) (Table 3).

**Table 3.** Projected change (%) in seasonal mean water level and discharge at Noapara in the Betna River: Comparison of the two Representative Concentration Pathway (RCP) scenarios for the near (2040s) and far (2090s) future with the baseline year. The monsoon season occurs during June–September and the dry season during November–February.

GCMs	Near Future (2040s)								Far Future (2090s)							
	RCP 4.5				RCP 8.5				RCP 4.5				RCP 8.5			
	Monsoon		Dry		Monsoon		Dry		Monsoon		Dry		Monsoon		Dry	
	Flood Tide	Ebb Tide	Flood Tide	Ebb Tide	Flood Tide	Ebb Tide	Flood Tide	Ebb Tide	Flood Tide	Ebb Tide	Flood Tide	Ebb Tide	Flood Tide	Ebb Tide	Flood Tide	Ebb Tide
<b>Water level (% change)</b>																
IPSL-CM5A	11.1	11.3	10.6	10.7	15.5	15.1	14.2	13.9	15.6	15.4	14.5	14.4	21.4	21.7	19.7	19.9
MPI-ESM	11.4	11.7	11.1	11.3	15.8	15.4	14.5	14.1	16.1	15.9	14.8	14.9	22.1	22.7	20.3	20.5
<b>Discharge (% change)</b>																
IPSL-CM5A	7.6	7.2	1.2	1.3	11.6	11.4	0.8	0.6	14.7	14.9	0.4	0.5	20.2	20.5	-1.8	-1.6
MPI-ESM	8.2	8.1	0.8	0.9	12.4	12.7	0.7	0.7	16.1	16.2	-1.3	-1.2	21.3	21.1	-2.2	-2.3

### 3. Results

#### 3.1. Model Calibration, Validation and Sensitivity Analysis

Through calibration, a very good agreement with the measured data for both water level and discharge was achieved (Figure 3), with  $R^2$  0.92 and 0.83, and NSE 0.81 and 0.66, respectively. Bed roughness (i.e., Manning's number) is a calibration parameter which has the largest impact on water level; after calibration, a constant Manning's number of  $60 \text{ m}^{1/3}/\text{s}$  was used. The agreement between the modelled and measured water level for the baseline year (validation) was very good ( $R^2 = 0.89$ , NSE = 0.76); the comparison for the discharge was not possible due to the lack of measured data. The model calibration and validation showed that the timing of the peaks was captured well, but the model slightly overestimated water level at low tides and underestimated discharge at high tides (Figures 3 and 4).

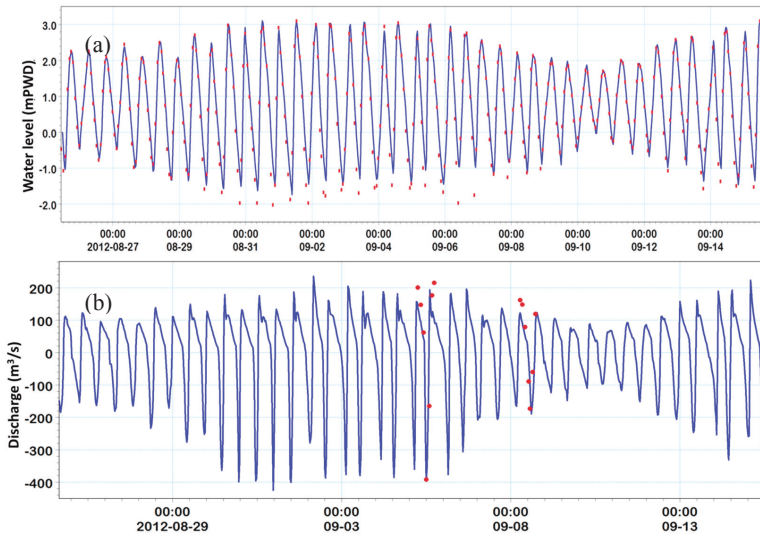


**Figure 3.** Model calibration: simulated and measured tidal water level (a) and discharge (b) at Noapara in the Betna River. The lines and dots represent the modelled values and measured values, respectively. The negative discharge values mean that during flood tide the flow is from the opposite direction.

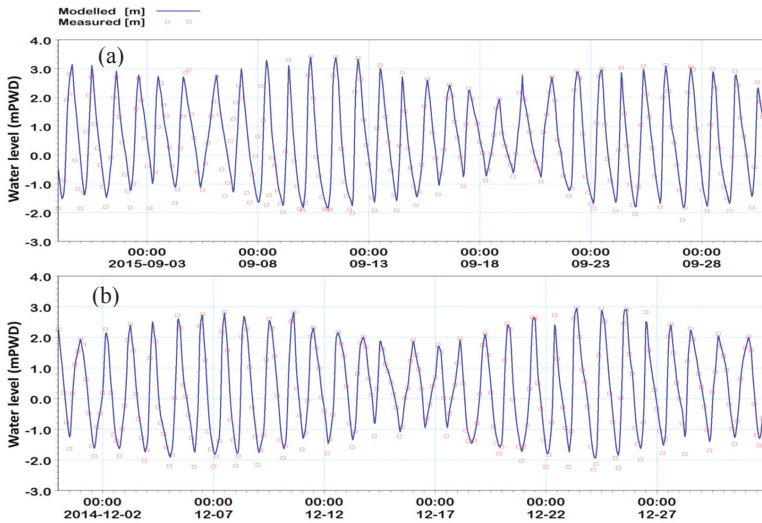


**Figure 4.** An example of comparison of modelled and measured tidal water level at Noapara in the Betna River. (a) represents a wet month (September 2015), and (b) represents a dry month (December 2014).

The sensitivity analysis showed that the model output was mostly influenced by the water level and discharge at the model boundaries. The increase in water level at the downstream boundary due to SLR greatly influenced the model output. The model output was also sensitive to wind, which influenced the water level. The average wind speed of 3 m/s had no strong influence on the water level, while the wind speed of 15 m/s (the strongest observed) caused decreased water level in the upstream parts of the river.

### 3.2. Future Projections

Future air temperature, precipitation and discharge projections show substantial variation between the two scenarios (RCP 4.5 and RCP 8.5) and two GCMs (Figure 5). Average air temperatures are expected to increase by 2 °C to 4 °C by the 2040s and 2090s respectively, compared to the observed baseline condition; the temperatures were consistently increased throughout the year, with greater increases by the 2090s compared to the 2040s. Precipitation is projected to increase during the monsoon season (June–September) by 3–28% and 5–32% by the 2040s and 2090s, respectively. Monthly average discharge shows increases in the near and far future compared to the observed discharge for both GCMs and both scenarios (Figure 5); the discharge is expected to increase in the monsoon periods and slightly decrease in dry periods (November–February).

The seasonal changes (percentage) in the mean water level and daily maximum discharge for the two GCMs and different scenarios are presented in Table 3. The mean change in water level at Noapara relative to the baseline year would be about 11% for the RCP 4.5 scenario and near future (2040s) and 23% for the RCP 8.5 scenario and far future (2090s), with increases being slightly larger in the monsoon than in the dry season. For the future discharge, the largest increase is expected in the monsoon period (June–September), with the data for the dry season showing no noticeable changes. The increase in the daily maximum discharge during the monsoon compared to the baseline year would be up to 8 and 16% in the near and far future respectively for RCP 4.5, and up to 21% by the end of century for RCP 8.5 (Table 3). The mean seasonal water level and discharge values for the two GCMs were not very different during the flood and ebb tide periods. The MPI-ESM GCM showed slightly higher water level and more extreme discharge in the Betna River compared to the IPSL-CM5A GCM.

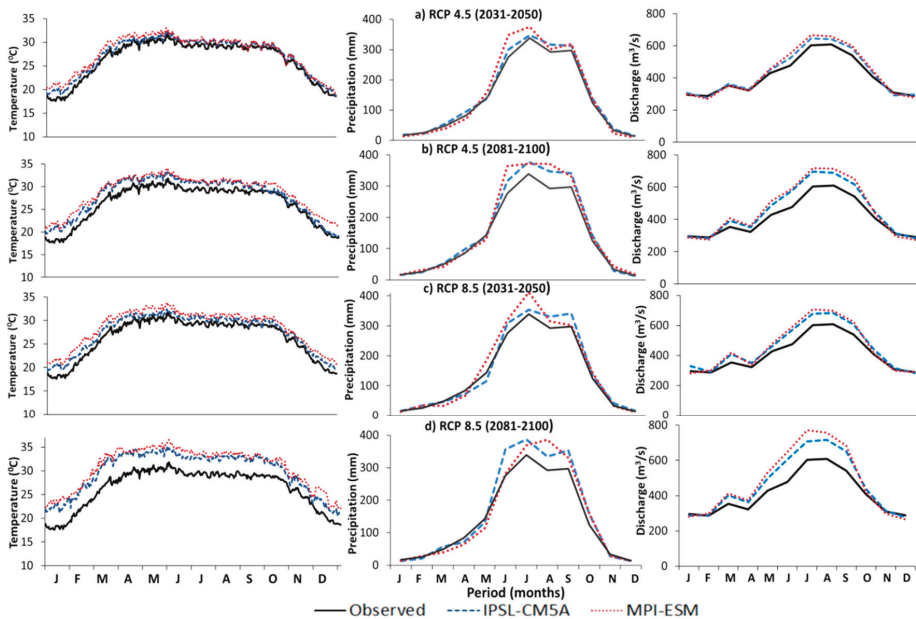


**Figure 5.** Daily average air temperature (left), monthly average precipitation (middle), and monthly average discharge (right) projections for the Betna River basin for two RCPs, RCP 4.5 (a,b) and RCP 8.5 (c,d) and two future periods, near future (2031–2050; a,c) and far future (2081–2100; b,d).

The impact of climate change and SLR was also assessed by comparing probability density functions (PDFs) developed for the baseline year and for the future conditions. Fitting the data to PDFs allowed identification of the trends and tendencies in changes of the river water level and discharge caused by climate change. Modelling results regarding hourly water level and daily maximum discharge for all studied scenarios were fitted to a non-parametric probability distribution (Figure 6). Compared to the baseline year, the frequencies of high water level and daily maximum discharge are expected to increase in the future. The comparison of the RCP 4.5 scenarios with the baseline year showed a little increase in water level and daily maximum discharge in the near future (2040s), while in the far future (2090s), comparatively higher water level and daily maximum discharge can be expected. The comparison of the RCP 8.5 scenarios with the baseline year showed that a comparatively higher (than the RCP 4.5) water level and discharge would be expected for both the near and far future. Larger change was projected for the results from the MPI-ESM model compared to the IPSL-CM5A model.

To understand the individual impacts of SLR and the increase in upstream discharge on the water level in the Betna River, the model was run with and without SLR and the increase in upstream discharge during the monsoon. With the increase in upstream discharge, but without SLR, the future water level was found to be almost the same as in the baseline period (water level increased overall by around 1%). On the other hand, with SLR but without the increase in upstream discharge, the future water level was found to increase by 10–15% in the 2040s and 14–21% in the 2090s. Thus, for this tidal river, SLR had a stronger impact on the water level compared to the impact of the increase in upstream discharge, because the direction of the flow in the river is dominated by the tide. However, when the increased upstream discharge during the monsoon season coincides with high tide, the impact on the water level is greater.

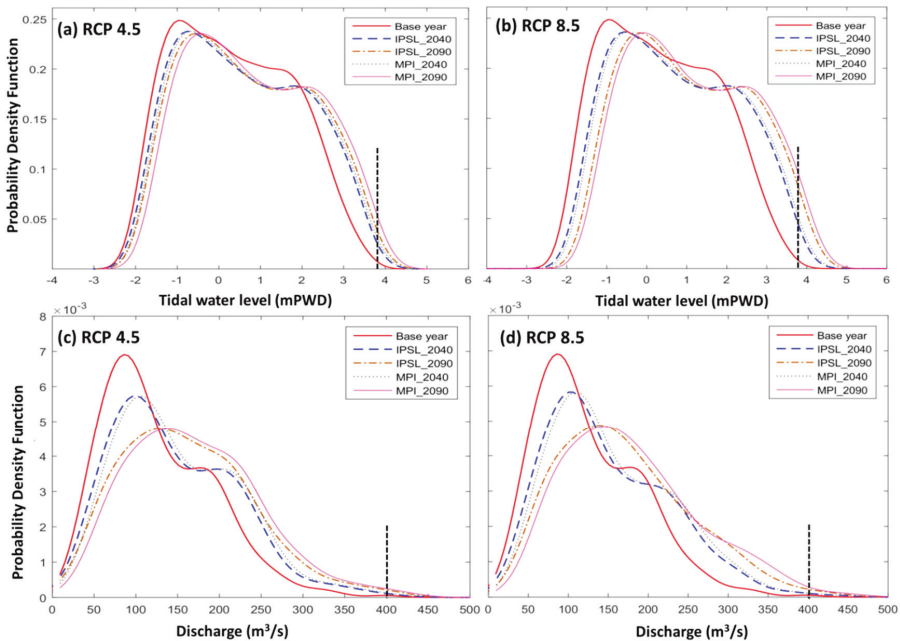


**Figure 6.** Probability density functions (PDFs) of hourly water levels (a,b) and daily maximum discharges (c,d) in the Betna River at Noapara for the baseline year (2014–2015) and in the near (2040s) and far (2090s) future under RCP 4.5 (a,c) and RCP 8.5 (b,d) for the two General Circulation Models (GCMs). The vertical dotted lines represent flood danger water levels (a,b) and extreme discharge levels (c,d).

The highest water level of the last 25 years in the Betna River at Benarpota (near Noapara) was 4.05 mPWD, and the flood danger level for 2014 was 3.84 mPWD [15]. The modelling results revealed that duration above the current flood danger level will increase up to 15 days by the 2040s and 34 days by the 2090s (Table 4). The duration of extreme discharge,  $>400 \text{ m}^3/\text{s}$  (defined as an extreme based on modelled and measured data) will increase up to 14 days by the 2040s and 33 days by the 2090s.

**Table 4.** Change in duration above the current (2014–2015) flood danger level and extreme discharge at Noapara in the Betna River for two RCPs, two GCMs and two future periods.

GCMs	Scenarios	Duration above Flood Danger Level	Duration above Discharge of $400 \text{ m}^3/\text{s}$
	Baseline (2014–2015)	13 days	11 days
IPSL-CM5A	RCP 4.5 (2040s)	25 days	21 days
	RCP 8.5 (2040s)	27 days	24 days
	RCP 4.5 (2090s)	41 days	35 days
	RCP 8.5 (2090s)	45 days	46 days
MPI-ESM	RCP 4.5 (2040s)	25 days	22 days
	RCP 8.5 (2040s)	28 days	25 days
	RCP 4.5 (2090s)	43 days	36 days
	RCP 8.5 (2090s)	47 days	46 days

#### 4. Discussion

The results revealed an increase in air temperature, and increased monsoon precipitation and discharge, which are in good agreement with other studies of this region [9,12,13,29]. The increased monsoon precipitation and discharge indicate a wetter monsoon season in the future. However, during the dry season, precipitation and discharge are mostly expected to decrease in the future. This means that less water will be available during the dry season. The decreased precipitation and discharge during the dry season are unlikely to lead to droughts in the study area, because of the continuous tidal water inflow from the bay. This could exacerbate the existing salinity intrusion problem [28]. However, the decreased dry weather precipitation and associated salinization were not the focus of this study.

The future scenario analysis reveals that the mean change in water level and discharge relative to the baseline year would be up to 23% and 21% respectively, by the end of century. This increased discharge combined with the high water level would likely worsen the flooding situation in southwest Bangladesh and cause major flooding problems in the Betna River basin. Whitehead and Barbour [11] also indicated in their study that a 15% increase of discharge in the GBM River systems by the 2050s would have the potential to increase flood risk within Bangladesh. The increased river discharge in the monsoon season in the future is consistent with the future projected increased precipitation. The increase in monsoon discharge can also be attributed to the increased monsoon discharge in the upstream rivers of the Betna River. The increasing trend of monsoon precipitation and river discharge in South Asia is also evident from other studies [9,12,13,25,30,31].

The dry season data shows no noticeable change in the future discharge (Table 3) due to lack of connectivity with upstream rivers during the dry months. This is in agreement with Zaman, Molla [29] in their study in the GBM River systems of Bangladesh. Zaman and Molla [29] also found increased monsoon discharge and little change in the dry season discharge due to siltation at the upstream river mouth. The dry season discharge is expected to reduce by maximum 2% in the far future and this is unlikely to substantially change the present situation of the Betna River because of the tidal influence.

The results also revealed that SLR had a stronger impact on the water level compared to the impact of upstream discharge change. The upstream discharge is dependent on precipitation; during the monsoon, fresh water inflow from upstream areas increases. In a tidal river like the Betna River, the impact of discharge on the water level is limited, because the direction of the flow in the river is dominated by the tide. However, when the increased upstream discharge coincides with high tide, the impact on the water level is greater. The increased duration of the water danger level combined with

increased frequency of extreme discharge (Table 4 and Figure 6) can severely affect the surrounding agricultural land by prolonged inundation during the monsoon and cause losses in terms of lives and livelihoods. When the water danger level coincides with the extreme discharge event, it would cause disastrous floods in the Betna River basin.

The MIKE 21 FM model was chosen to study the Betna River, because this model is suitable for tidal rivers and produces results at high temporal and spatial resolution. However, this choice comes at a cost of high computational requirements, which limited the opportunities to run the model for many years and many different GCM outputs. However, using several GCMs is recommended for further studies, since using a full ensemble of climate models would provide a better understanding of uncertainty.

The model was successfully calibrated for a monsoon season and validated for a full year, as has been done in other studies [4,25,26,28]. A possible reason for the slight overestimation of the water level at low tides can be the simplification of the river cross-section during mesh generation; thus better bathymetric data would be beneficial for further improvement of the model. This overestimation may also be the case for the results of future scenarios. However, as the impact is likely to be the same for the baseline period and future scenarios, and the future scenarios are compared with the baseline period, this slight overestimation should not affect the outcomes of this study. The slight underestimation of the discharge at high tides, which occurs in many hydrological models [32] and can possibly be explained by the lack of an extreme flood during the calibration period, could result in a stronger underestimation for a more extreme year. This may also mean that for the future, the peaks could be more underestimated than for the present.

To simulate the future scenarios, the discharge projections for the upstream Gorai River [25] were considered representative for the Betna River, due to the lack of local future discharge projections. Even though the modelling results were sensitive to the discharge at the upstream boundary, for the future conditions, the SLR proved much more important than the increase in the upstream boundary discharge. Therefore, the choice for the future discharge projections is relatively unimportant.

Identifying the trends and future scenarios for hydrodynamic characteristics triggered by climate change is required for the effective management of water bodies. This information on present and future hydrodynamic conditions can assist policy makers and water managers in planning flood risk mitigation and designing adequate flood protection structures. This information can be used to formulate a project for strengthening climate resilience. Although some other factors such as, changes in water use upstream, land-use change, population growth, socio-economic development and river dredging activities could significantly influence future impacts, focus should not be on climate change only; other changes that could have major impacts on the sustainability of water management infrastructure should not be overlooked [4]. Flood forecasting, i.e., early warning system should be developed to inform local farmers about their roles in an adverse weather condition. Construction of reservoirs near the river bank to store excess flood water for uses in the dry season can be another effective adaptation measure. The developed model, climate change scenario analysis approach and results of this study can potentially be useful for other river basins with similar geographic settings.

## 5. Conclusions

This study assessed the present situation and the future climate change impacts on the water level and discharge in the Betna River by applying a hydrodynamic model MIKE 21 FM. Based on the obtained modelling results, we conclude that:

- increased precipitation and SLR are expected in the Betna River basin in the near and far future under both RCP 4.5 and RCP 8.5;
- in RCP 8.5, water level and discharge in the Betna River are expected to increase up to 16 and 13% for the 2040s, and up to 23 and 21% for the 2090s, respectively;

- in RCP 4.5, although the expected increase in river discharge is relatively low (i.e., between 7 and 16%), the increased discharge combined with an increased water level is likely to cause major floods in the Betna River basin;
- the modelling results suggest that during the dry season, a small decrease in discharge (up to 2%) is expected for the 2090s;
- SLR explains a larger part of the future increase in water level than increasing upstream discharge; and
- in the future, the duration above the current flood danger level and of the extreme discharge events is expected to increase by half a month (per year) in the 2040s and by more than one month in the 2090s, causing prolonged inundation in the river basin, particularly during the monsoon.

**Author Contributions:** M.M.M.I.; Data curation, M.M.M.I. and E.S.; Formal analysis, M.M.M.I., N.H. and E.S.; Investigation, M.M.M.I.; Methodology, M.M.M.I., N.H. and E.S.; Project administration, M.M.M.I.; Resources, N.H.; Software, E.S.; Supervision, N.H.; Writing-original draft, M.M.M.I.

**Acknowledgments:** We thank the Ministry of Science and Technology of the Government of Bangladesh for providing a fellowship to pursue this study. We thank the Bangladesh Water Development Board, Meteorological Department and the Institute of Water Modelling for kindly providing river bathymetric and hydro-meteorological data and giving permission to use the data in the modelling work. We especially thank the DHI for providing the licence for the MIKE Powered by DHI software. Furthermore, we thank Rik Leemans (Wageningen University) for his help in critical review of the manuscript.

## References

1. Webster, T.; McGuigan, K.; Collins, K.; MacDonald, C. Integrated river and coastal hydrodynamic flood risk mapping of the lahav river estuary and town of Bridgewater, Nova Scotia, Canada. *Water* **2014**, *6*, 517–546. [CrossRef]
2. Ahmed, A.U. Bangladesh Climate Change Impacts and Vulnerability: A Synthesis, Climate Change Cell Department of Environment, Govt. of Bangladesh. 2006. Available online: [https://www.Preventionweb.Net/files/574\\_10370.Pdf](https://www.Preventionweb.Net/files/574_10370.Pdf) (accessed on 25 March 2017).
3. CEGIS. *Environmental Impact Assessment of Re-Excavation of Betna River in Satkhira District for Removal of Drainage Congestion*; Bangladesh Water Development Board: Dhaka, Bangladesh, 2013; pp. 1–182.
4. Asian Development Bank (ADB). *Adapting to Climate Change: Strengthening the Climate Resilience of the Water Sector Infrastructure in Khulna, Bangladesh*; Asian Development Bank: Mandaluyong City, Philippines, 2011; pp. 1–40.
5. Karim, M.F.; Mimura, N. Impacts of climate change and sea-level rise on cyclonic storm surge floods in bangladesh. *Glob. Environ. Chang.* **2008**, *18*, 490–500. [CrossRef]
6. IPCC. Summary for policymakers. In *Climate Change 2014: Impacts, Adaptation, and Vulnerability. Part A: Global and Sectoral Aspects*; Field, C.B., Barros, V.R., Dokken, D.J., Mach, K.J., Mastrandrea, M.D., Bilir, T.E., Chatterjee, M., Ebi, K.L., Estrada, Y.O., Genova, R.C., et al., Eds.; Contribution of Working Group II to the Fifth Assessment Report of the Intergovernmental Panel on Climate Change; Cambridge University Press: Cambridge, UK; New York, NY, USA, 2014; pp. 1–32.
7. Mohammed, K.; Islam, A.S.; Islam, G.T.; Alfieri, L.; Bala, S.K.; Khan, M.J.U. Extreme flows and water availability of the brahmaputra river under 1.5 and 2 °C global warming scenarios. *Clim. Chang.* **2017**, *145*, 159–175. [CrossRef]
8. Bandudeltas. *Baseline Study on Climate Change in Bangladesh Delta Plan 2100 Project: Coast and Polder Issues, Planning Commision, Government of Bangladesh*; Bandudeltas: Dhaka, Bangladesh, 2015.

9. Jin, L.; Whitehead, P.; Sarkar, S.; Sinha, R.; Futter, M.; Butterfield, D.; Caesar, J.; Crossman, J. Assessing the impacts of climate change and socio-economic changes on flow and phosphorus flux in the ganga river system. *Environ. Sci. Process. Impacts* **2015**, *17*, 1098–1110. [CrossRef] [PubMed]
10. Kuchar, L.; Iwański, S. A modeling framework to assess the impact of climate change on river runoff. *Meteorol. Hydrol. Water Manag.* **2014**, *2*, 49–63. [CrossRef]
11. Whitehead, P.; Barbour, E.; Futter, M.; Sarkar, S.; Rodda, H.; Caesar, J.; Butterfield, D.; Jin, L.; Sinha, R.; Nicholls, R. Impacts of climate change and socio-economic scenarios on flow and water quality of the ganges, brahmaputra and meghna (GBM) river systems: Low flow and flood statistics. *Environ. Sci. Process. Impacts* **2015**, *17*, 1057–1069. [CrossRef] [PubMed]
12. Ghosh, S.; Dutta, S. Impact of climate change on flood characteristics in brahmaputra basin using a macro-scale distributed hydrological model. *J. Earth Syst. Sci.* **2012**, *121*, 637–657. [CrossRef]
13. Apurv, T.; Mehrotra, R.; Sharma, A.; Goyal, M.K.; Dutta, S. Impact of climate change on floods in the brahmaputra basin using CMIP5 decadal predictions. *J. Hydrol.* **2015**, *527*, 281–291. [CrossRef]
14. Alam, R.; Islam, M.S.; Hasib, M.R.; Khan, M.Z.H. Characteristics of hydrodynamic processes in the meghna estuary due to dynamic whirl action. *IOSR/JEN* **2014**. [CrossRef]
15. IWM. *Feasibility Study for Drainage Improvement of Polder 1, 2, 6–8 by Mathematical Modelling under the Satkhira District*; Institute of Water Modelling: Dhaka, Bangladesh, 2014; pp. 1–184.
16. Hossain, A.N.H.A. *Integrated Flood Management: Case Study Bangladesh*; Bangladesh Water Development Board (BWDB): Dhaka, Bangladesh, 2003; pp. 1–14.
17. Islam, M.M.M.; Hofstra, N.; Islam, M.A. The impact of environmental variables on faecal indicator bacteria in the betna river basin, Bangladesh. *Environ. Process.* **2017**, *4*, 319–332. [CrossRef]
18. DHI. *Mike 21 and Mike 3 Flow Model FM*; MIKE by DHI: Horsholm, Denmark, 2011.
19. Uddin, M.; Alam, J.B.; Khan, Z.H.; Hasan, G.J.; Rahman, T. Two dimensional hydrodynamic modelling of northern bay of bengal coastal waters. *Comput. Water Energy Environ. Eng.* **2014**, *3*, 140–151. [CrossRef]
20. Cronshey, R.G.; Roberts, R.T.; Miller, M. Urban Hydrology for Small Watersheds. In *Proceeding of the Specialty Conference, Hydraulics and Hydrology in the Small Computer Age. Hydrology Division/ASCE, Lake Buena Vista, FL, USA, 12–17 August 1985*; Waldrop, W.R., Ed.; American Society of Civil Engineers: New York, NY, USA, 1985.
21. Moriasi, D.N.; Arnold, J.G.; Van Liew, M.W.; Bingner, R.L.; Harmel, R.D.; Veith, T.L. Model evaluation guidelines for systematic quantification of accuracy in watershed simulations. *Trans. ASABE* **2007**, *50*, 885–900. [CrossRef]
22. Christensen, N.S.; Lettenmaier, D.P. A multimodel ensemble approach to assessment of climate change impacts on the hydrology and water resources of the colorado river basin. *Hydrol. Earth Syst. Sci. Discuss.* **2007**, *11*, 1417–1434. [CrossRef]
23. Taylor, K.E.; Stouffer, R.J.; Meeh, G.A. An overview of CMIP5 and the experiment design. *Bull. Am. Meteorol. Soc.* **2012**, *93*, 485–498. [CrossRef]
24. Liu, C.; Hofstra, N.; Leemans, R. Preparing suitable climate scenario data to assess impacts on local food safety. *Food Res. Int.* **2015**, *68*, 31–40. [CrossRef]
25. Billah, M.; Rahman, M.M.; Islam, A.K.M.S.; Islam, G.M.T.; Bala, S.K.; Paul, S.; Hasan, M.A. Impact of climate change on river flows in the Southwest region of Bangladesh. In *Proceedings of the 5th International Conference on Water & Flood Management (ICWFM-2015)*, Dhaka, Bangladesh, 6–8 March 2015.
26. Elshemy, M.; Khadr, M. Hydrodynamic impacts of egyptian coastal lakes due to climate change-example Manzala Lake. *Int. Water Technol. J.* **2015**, *5*, 235–246.
27. Kay, S.; Caesar, J.; Wolf, J.; Bricheno, L.; Nicholls, R.; Islam, A.S.; Haque, A.; Pardaens, A.; Lowe, J. Modelling the increased frequency of extreme sea levels in the ganges–brahmaputra–meghna delta due to sea level rise and other effects of climate change. *Environ. Sci. Process. Impacts* **2015**, *17*, 1311–1322. [CrossRef] [PubMed]
28. Dasgupta, S.; Kamal, F.A.; Khan, Z.H.; Choudhury, S.; Nishat, A. *River Salinity and Climate Change: Evidence from Coastal Bangladesh*; World Bank Policy Research Working Paper; World Bank Group: Washington, DC, USA, 2014.
29. Zaman, A.; Molla, M.; Pervin, I.; Rahman, S.M.; Haider, A.; Ludwig, F.; Franssen, W. Impacts on river systems under 2 °C warming: Bangladesh case study. *Clim. Serv.* **2017**, *7*, 96–114. [CrossRef]
30. Kirby, J.; Mainuddin, M.; Mpelasoka, F.; Ahmad, M.; Palash, W.; Quadir, M.; Shah-Newaz, S.; Hossain, M. The impact of climate change on regional water balances in Bangladesh. *Clim. Chang.* **2016**, *135*, 481–491. [CrossRef]

31. Mirza, M.M.Q.; Warrick, R.; Ericksen, N. The implications of climate change on floods of the ganges, brahmaputra and meghna rivers in Bangladesh. *Clim. Chang.* **2003**, *57*, 287–318. [CrossRef]
32. Kan, G.; He, X.; Ding, L.; Li, J.; Liang, K.; Hong, Y. Study on applicability of conceptual hydrological models for flood forecasting in humid, semi-humid semi-arid and arid basins in China. *Water* **2017**, *9*, 719. [CrossRef]

# A Novel Method for Evaluation of Flood Risk Reduction Strategies: Explanation of ICPR FloRiAn GIS-Tool and Its First Application to the Rhine River Basin

Adrian Schmid-Breton<sup>1,\*</sup>, Gesa Kutschera<sup>2</sup>, Ton Botterhuis<sup>3</sup> and  
The ICPR Expert Group 'Flood Risk Analysis' (EG HIRI)<sup>4,†</sup>

<sup>1</sup> International Commission for the Protection of the Rhine, 56068 Koblenz, Germany

<sup>2</sup> Research Institute for Water and Waste Management at RWTH Aachen (FiW) e. V,  
Department of Innovation and Knowledge Transfer (Project coordination Africa), 52056 Aachen, Germany;  
kutschera@fiw.rwth-aachen.de

<sup>3</sup> HKV Lijn in Water, Security and crisis management, 8203 Lelystad, The Netherlands; ton.botterhuis@hkv.nl

<sup>4</sup> Expert Group, "Flood Risks" (EG HIRI) of the International Commission for the Protection of the  
Rhine (ICPR), Germany; sekretariat@iksr.de

\* Correspondence: adrian.schmid-breton@iksr.de

† The members of this expert group are listed by name at the end of the paper under "Acknowledgments".

**Abstract:** To determine the effects of measures on flood risk, the International Commission for the Protection of the Rhine (ICPR), supported by the engineering consultant HKV has developed a method and a GIS-tool named "ICPR FloRiAn (Flood Risk Analysis)", which enables the broad-scale assessment of the effectiveness of flood risk management measures on the Rhine, but could be also applied to other rivers. The tool uses flood hazard maps and associated recurrence periods for an overall damage and risk assessment for four receptors: human health, environment, culture heritage, and economic activity. For each receptor, a method is designed to calculate the impact of flooding and the effect of measures. The tool consists of three interacting modules: damage assessment, risk assessment, and measures. Calculations using this tool show that the flood risk reduction target defined in the Action Plan on Floods of the ICPR in 1998 could be achieved with the measures already taken and those planned until 2030. Upon request, the ICPR will provide this tool and the method to other river basin organizations, national authorities, or scientific institutions. This article presents the method and GIS-tool developed by the ICPR as well as first calculation results.

**Keywords:** GIS; tool; flood risk analysis; transboundary flood risk assessment; flood risk management; effects of measures; effectiveness of measures; Rhine; ICPR; International Commission for the Protection of the Rhine; ICPR FloRiAn

---

## 1. Introduction

In the past, several important flood events occurred in the Rhine river basin (cf. Figure 1) and are the reason for why the nine countries of the basin are working together within the International Commission for the Protection of the Rhine (ICPR) [1] on the topic of transboundary flood risk management. The first results of this cooperation are the Action Plan on Floods (APF) [2,3] in 1998 and the first Flood Risk Management Plan (FRMP) for the international river basin district Rhine (IRBD) according to the "Floods Directive" of the European Union (Directive 2007/60/EC) in 2015 [4,5]. In the APF of 1998, one of the four objectives set out by the Rhine bordering states was to reduce the risk of flood damage by 10% by 2005, and by 25% by 2020, in comparison to the 1995 figures.

On the other hand, the most important objective of the Floods Directive (FD) in force since 2007 is the reduction of the adverse consequences of flooding upon human health, the environment, cultural heritage and economic activity. To help assess and monitor the effects and effectiveness of implemented flood risk management measures to verify and determine the risk and damage reduction resulting from the implementation of the APF and FRMP, the ICPR—supported by the engineering consultant HKV—developed a specific tool running in a geographic information system (GIS) named “ICPR FloRiAn (Flood Risk Analysis)” [6]. The tool is the result of a cooperation of several authorities of different nationality within the Rhine River Basin. The Technical report (ICPR report no. 237) [7] describes the method and calculations and the Synthesis report (ICPR report no. 236) [8] contains a summary of the method and describes the results of calculations undertaken using the tool.

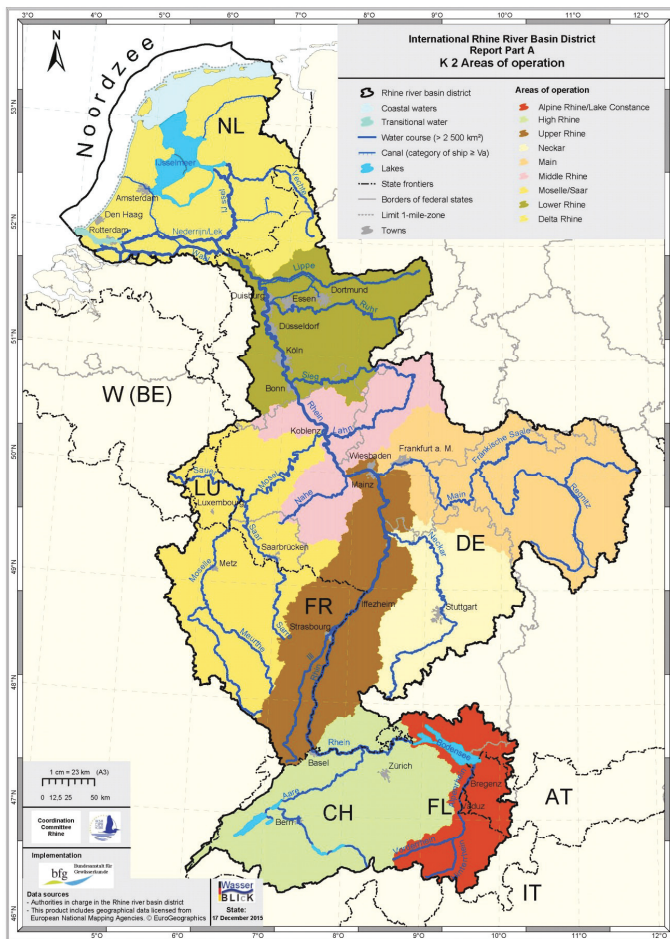


Figure 1. Rhine river basin [1].

Although other useful methods and tools exist [9–20], ICPR FloRiAn was specially tailored to the ICPR’s wishes. As a result, the tool meets the needs and requirements of the Rhine bordering states, which had an impact on various parameters. For example, the tool is based on data available in the

Rhine bordering countries and, during the development of the tool, great importance was attached to create a link with the FD. This is also reflected in the type of measures and the data used.

As stated above, in addition to ICPR FloRiAn, there are several other methods, models and (GIS) tools that deal with the simulation of flood events and their consequences as well as the assessment of flood risks [9–15]. The specificity of ICPR FloRiAn is, however, to extend flood risk analysis to the effects or effectiveness of flood risk management measures on the development or reduction of damages or risks. The quantification of non-structural measures and their combination with each other is particularly innovative. For example, flood forecasting and sensitization measures have positive influence on one another and can also have an effect on the proportion of taking precaution for building protection. Another novelty is the consideration of other receptors as solely the economic activities: people, environment, and cultural heritage. Special reflections have been made to create appropriate methods for these receptors. Moreover, contrary to other methods or GIS-based applications, the aim of ICPR FloRiAn is not a cost-benefit analysis (only the economic damage is monetarized and costs of measures are not considered), but to identify a general damage or risk reduction (with or without the impacts of measures). Like many other models, the tool is able to carry out theoretical calculations (sensitivity analysis) at different (administrative) levels. Finally, ICPR FloRiAn differs significantly from instruments for crisis management [16–20], the focus being here on prevention measures.

Within the GIS toolbox ICPR FloRiAn (see Section 3 for an extract of the tool), flood hazard and risk maps (e.g., developed under the FD, see explanation in Section 2.1) [21] are input for the calculation. The tool consists of three interacting modules resulting in an overall damage or risk assessment for four receptors (or types of adverse consequences of floods) defined by the FD: human health, environment, culture heritage and economic activity. The ICPR has used this tool to assess the risk evolution along the Rhine from 1995 up to now (results are presented in Section 4) and has planned to use the tool to carry out regular reviews of the impacts of measures on flood risk reduction for the FRMP.

The tool ICPR FloRiAn, as well as the methods it is based on and a user guide, are available on simple demand at the ICPR (basic contract) and can be applied to other river basins by river organizations or national institutions [6], provided that basic GIS knowledge, GIS technical features (see Section 3), and the following required input data for the area under study are available in ESRI ArcGIS format: flood hazard (water depth grid), data related to receptors in flood prone areas (land uses, number of affected people, potentially polluting industries, nature protection areas, cultural heritage objects), damage functions, and various information on the implementation of measures. The instrument can also be used partially (for one or more modules or receptors), with less data or by using some ICPR data (such as damage functions) or even by using theoretical/dummy data. Although it was developed for a macroscopic level (the Rhine basin), tests were undertaken by extern users on a more local or regional level (City of Cologne, City of Rosenheim in Bavaria, German part of the Danube; not published) and gave interesting and logical results. Thus, the limit of applications to other areas is only given by available data, GIS system, and knowledge.

## 2. Description of the Method

### 2.1. Definitions and Basic Information

Mathematically, flood risk is defined as a product of probability of occurrence and the potential damage. The ICPR has developed specific methods, some of which are new, for determining the damage potential and the risk for the four receptors human health, environment, cultural heritage, and economic activities (cf. Sections 2.2–2.5) [7,8]. Furthermore, the effect of various measures can lead to changes in flood risk, which can be affected in two ways: by changing the flood probability and by influencing the potential damage (cf. Section 2.6). The modification of flood probability due to water level reduction measures such as retention measures and riverbed enlargement is described in

the ICPR report no. 229 (cf. Section 2.6) [22]. The economic flood risk is calculated using the following formula [7,8,10]:

$$\text{Flood risk [€/year]} = \text{Potential damage [€]} \times \text{flood probability [1/year]}$$

The damage potential of the receptors human health, environment, and cultural heritage is not calculated in monetary terms, so that the potential damage in € will be replaced by the number of persons or protected properties concerned (here as an example for the protection of human health [7,8,22]):

$$\text{Flood risk [probability of being affected in inhabitants/year]} = \text{number of affected inhabitants} \times (1 - \text{safeguarding rate [inhabitants potentially evacuated or placed in safety in \% of total affected inhabitants]}) \times \text{probability [1/year]}. \text{ (see also Section 2.3)}$$

The calculations of the flood risk are carried out using a GIS at the level of raster cells. During the evaluation, the results of individual raster cells are aggregated at the desired level in a table: e.g., stretches of the Rhine, municipality, district, region/federal state, or the whole Rhine catchment. The execution of calculations at different time horizons allows us to draw conclusions regarding the change of risk or the reduction of risk as a result of theoretically or actually implemented measures (cf. Section 4).

Figure 2 gives a general overview of the procedure for damage and risk calculation.

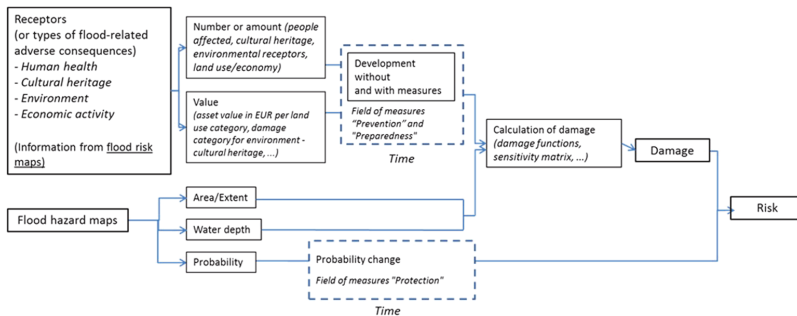


Figure 2. Overall risk analysis procedure [7,8].

Explanation of the calculation procedure and the data used presented in Figure 2 (see also sections hereafter):

- Flood risk maps: these maps are required by the FD and provide all the necessary information on receptors located in flood-prone areas (affected people, land use, etc.). A value or an amount (sum, number) is associated with these receptors. For economic damages, a damage function is associated with each type of land use (see Figure 3).
- Flood hazard maps: also required by the FD these maps provide all necessary information on the hazard (grid with inundation depth and flooding areas, flood probability in form of three scenarios: frequent, medium, and extreme floods). Hence, flood probability can be also entered separately in the tool.

The calculation of the damage (using special functions or sensitivity matrixes) and then the risks (combination with probability) (see Figure 2) can already be calculated with only input data from both types of maps mentioned above without including the influence of measures. To estimate the impacts of measures, one has to fill in the tool with information on their effects (entered and modifiable in the tool itself) and the level/number/percentage of measures implementation/realization (entered in

specific shapefiles). An information on the realization would be; e.g., % of a municipality covered by risk-based urban plans or the number of sensitization campaigns in a certain period (see Table 1 in Section 2.6.1). The integration of the impacts of measures are explained in Section 2.6. For economic damages, for example, the damage function associated with each type of land use is modified where certain measures are being achieved (reduction of water levels or inundation depth, see Figure 3 and Section 2.6.1). The results of the calculations are given in the form of a GIS file and are given in euro/year or in number of people or objects affected/year.

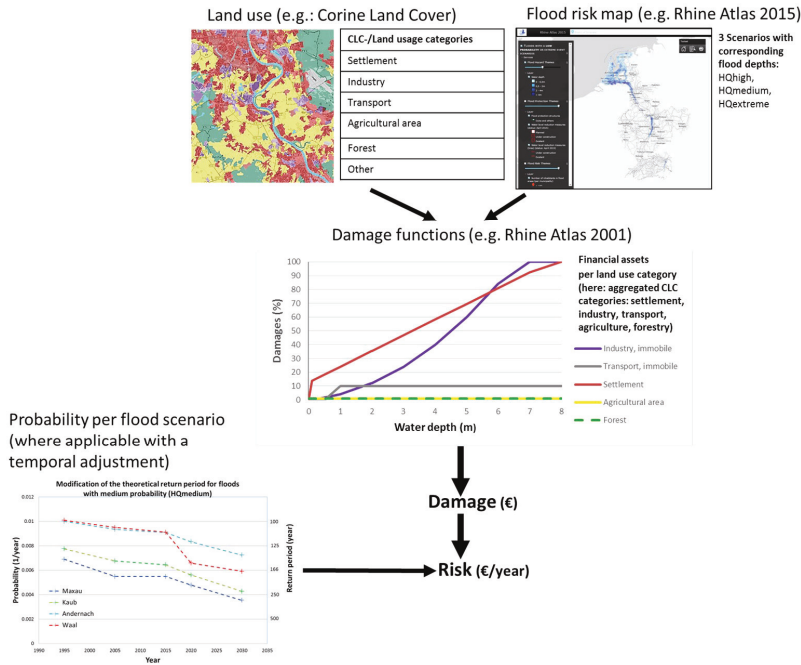


Figure 3. Approach for the analysis of the flood risk upon economic activity [7,8].

2.2. Receptor “Economic Activity”

The determination of the potential economic damage is based on the knowledge of the correlation between water depth and the resulting (relative) damage, the so-called damage functions. The direct economic damage potential is calculated in accordance with the methodology of the ICPR-Rhine Atlas 2001 [23]. Consequently, the damage potential is calculated on the basis of land use maps (Corine Land Cover 2006 in the case of the ICPR) included in flood risk maps (for the ICPR the ones of the Rhine Atlas 2015 [21]) for the three flood scenarios (frequent—HQhigh, medium—HQmedium and extreme floods—HQxtreme) by means of damage functions and specific asset values for the 6 categories: settlement, industry, transport, agricultural areas, forest, and other (cf. Figure 3). Each cell in the map is reclassified to one of the 6 categories using the value of the land use as input. With this reclassification one of the 6 damage functions is coupled to a cell. Value of each cell in the flood map is reclassified with the damage function to a potential damage value (as a percentage of the asset value). The asset values (for property and immobile damage) are adjusted at a regional level on the base of economic growth or the consumer price index in order to adequately reflect the time horizon under consideration. As a result, the potential damage in €/m<sup>2</sup> per category and the integral/total damage are calculated.

2.3. Receptor "Human Health"

The damage to the receptor human health is defined as the number of people potentially affected in the flooded area (for the calculation formula, see Section 2.1).

The chosen method follows a two-staged approach (cf. Figure 4):

1. Determination of all people affected (per defined area, e.g., administrative district, municipality, . . . ) regardless of water depth or other parameters for each flood scenario in total. In addition, the number of people affected can be established for the water level classes defined by the maps or the user.
2. Determination of the number of people who cannot get to safe places or be evacuated, using the approach of a state or area-specific minimal and maximal "safeguarding rate". This is the proportion of persons per region/area that could be evacuated or put in safety in advance of a potential flood and are therefore no longer in danger. The input of the safeguarding rate is given in % of the area under consideration (e.g., at municipality level) and is provided by the relevant countries for a reference time horizon (e.g., for 1995, minimal safeguarding rate of 20%; for 2015, maximal safeguarding rate of 80%). For the other time horizons (e.g., 2005), the safeguarding rate is calculated using a specific flow chart with an associated point system that considers the weighted effect of different prevention and preparedness measures according to their significance. This means that the safeguarding rate can be increased (e.g., in 2005 compared to 1995) by measures such as awareness rising, forecasting, warning and crisis management (cf. Table 1 in Section 2.6.1). The whole calculation procedure is precisely described in the ICPR report no. 237 [7].

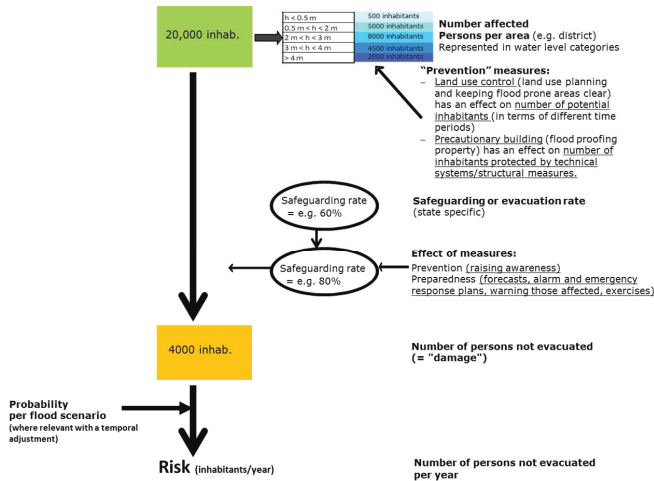


Figure 4. Approach for the analysis of damage to human health [7,8].

2.4. Receptor "Environment"

The method for assessing flood-related risks to the environment assumes that it is not the flood event itself, but rather the negative consequences triggered by the event that cause damage to surface water bodies that have a good or very good ecological status and to receptors/protected areas, in accordance with the FD. Negative consequences are understood to be the contamination of bodies of water via IPPC plants, SEVESO operation areas and waste water treatment plants due to flooding. The hazard or pollution potential resulting from the plant is defined in the tool on the basis of pollutant emission and transport models by means of an impact distance (distance between the source of danger

and the receptor). Possible damages caused by the direct effect of flooding on the environment are not included in the study.

The environmental impact assessment is carried out in two stages (cf. Figure 5):

1. In the first stage, the contamination potential of the plant is combined with the water level category. The greatest contamination potential and the highest water depth present the highest threat. For each plant and each flood scenario, the respective threat is determined and assigned to a qualitative scale (1 to 5).
2. The second stage combines the ecological significance of a protected area with its threat.

This evaluation results in the three damage classes “low”, “medium” and “high” and leads to an index per protected area. Within the framework of the calculations carried out, the damage indices per flood scenario and time horizon are summed (= aggregated damage index).

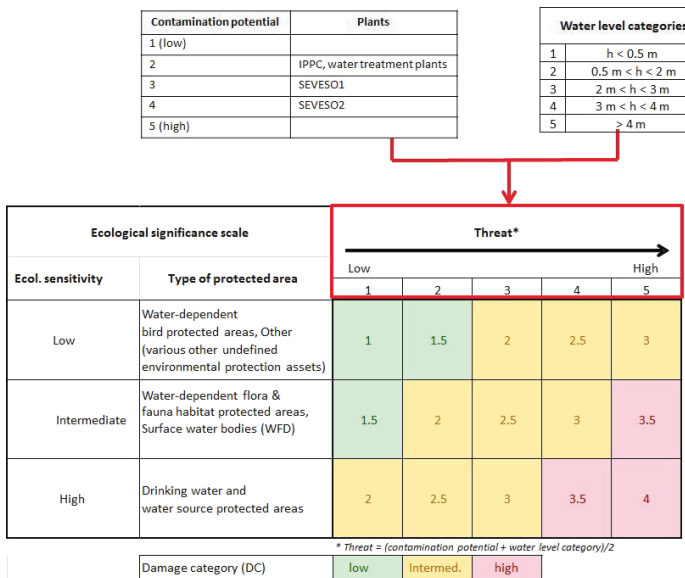


Figure 5. Approach for the analysis of damage to environment [7,8].

2.5. Receptor “Cultural Heritage”

Damage to cultural heritage can be approximated quantitatively by combining the significance of the cultural heritage (depending on the cultural heritage: UNESCO World Heritage Sites, protected urban areas, monuments) and water level.

By combining the defined value of a cultural asset with its water level, a specific matrix is created for assessing the damage to cultural assets. The matrix assessment results in a damage index for each object, to which one of the three damage categories is assigned, as in the case of the environmental damage. Cultural assets with low significance flooded by water levels of less than 2 m can expect a low level of damage, whereas water levels of 2 m or more lead to medium or high levels of damage.

2.6. Assessment of the Influence of Mitigation Measures—Elaboration of the Indicators

2.6.1. Change of Potential Damage

This section presents the measures in the areas of “prevention” and “preparedness” that impact the damage potential. Changes in the probability of flooding due to water level reduction measures,

such as retention measures and widening of the riverbed (category of measure “protection”), were taken into account through the modification of the probabilities (cf. Section 2.6.2).

For the quantification of the impact of measures on the development of floods, risk indicators have been defined for the different receptors. The indicators should be representative, reproducible, and quantifiable for a group of measures (cf. list of measures and indicators in Table 1).

**Table 1.** Overview of the measures and indicators integrated into the tool and the calculations [7,8].

Type of Measure	Indicator	Unit and Scale of Indicator
<b>Prevention</b>		
Spatial planning, regional planning, and land use planning	Building regulations and codes/building development plans including requirements for flood protection (flood-adapted construction)	Expanse (m <sup>2</sup> ) of area (municipality or higher level) in which flood-adapted construction is regulated by building development plans [m <sup>2</sup> ] and percentage (%) of the municipality area for which development plans with these types of regulations exist.
Keeping flood prone areas open/clear (preventing the location of new or additional receptors) and adapted usage of areas	Modification of land use data (e.g., CLC data) within and outside of the flooding areas of the flood hazard map under analysis.	Modification of land use [m <sup>2</sup> ]
Flood-adapted design, construction, renovation	Measures implemented regarding flood-adapted development/building	Measures implemented/realized in the municipality (or higher level) in %
Precautionary building/flood-proofing property for households/municipalities	Protected areas due to precautionary building/flood-proofing property and/or mobile systems	Polygon with the area (in the municipality or higher level) protected by the flood-proofing of property or mobile systems [m <sup>2</sup> ]
Precautionary building/flood-proofing property in hazardous installations (IPPC plants, SEVESO operation areas and waste water treatment plants)	Protected installations due to technical protection, precautionary building/flood-proofing property and/or mobile systems	List of installations (IPPC, SEVESO, waste water treatment plant) that are protected/not protected
Flood-proof storage of water-polluting/hazardous substances for households/municipalities	Securing oil tanks and/or safe storage in upper floors	Number of households (as proportion of affected households in %), that have secured oil tanks or stored water polluting substances in upper storeys (per municipality or higher level)
Flood-proof storage of water-polluting/hazardous substances for hazardous installations (IPPC plants, SEVESO operation areas and waste water treatment plants)	Securing oil tanks and/or safe storage in upper floors	List of installations (IPPC, SEVESO, waste water treatment plant) in which secured oil tanks are safeguarded or pollutants are stored in upper storeys (unit: yes/no)
Provision of flood hazard and risk maps/establishing awareness in relation to precautionary behavior, education and preparation/preparedness for flood events	Frequency/update intervals with regard to information campaigns (incl. provision/presence of flood hazard and risk maps)	Update frequency of information campaigns (years) (in a municipality or higher level)
<b>Protection</b>		
Retention measures	Modification of probability (ICPR Report No. 229) [22]	Modification of probability and localization (stretch of river/gauge)
Dykes, dams, flood walls, mobile flood protection, ...	For these measures, a probability is also indicated: Percentage evolution/change in flood probability between 1995 and present day due to improvements in protection.	Localization, renewals, modification of probability due to improvements in protection (%) (per measure or on a stretch of river)
Maintenance/renewal of technical flood protection structures	The information whether the area is protected/diked or non-protected/non-diked is relevant for the calculations.	
<b>Preparedness</b>		
Flood information and forecast	Improvement in flood forecasting within a defined time-period	Forecast period in hours/days as well as further aspects (on a national level or for river stretches)
Alarm and emergency response planning (incl. recovery/aftercare)/warnings for those affected/exercises/training	Presence and update frequency of alarm and emergency response plans; number of warning systems (warning methods/ways and communication means), details of civil protection/crisis management exercises including frequency	Number of systems and update frequencies (on a municipality or higher level)
Safety/safeguarding/evacuation of (potentially) affected persons	Details of minimum and maximum safeguarding rate for those affected in a particular area	Minimum and maximum safeguarding in % on a national level or for river stretches (e.g., 70% can be evacuated, max. safeguarding rate = 70)

Based on a literature survey (see references in the Literature list of the report no. 237 [7]) and partly on expert knowledge, the maximum damage reduction, also referred to as the “effect” of a measure, was determined and defined per indicator. The degree of realization; i.e., which and how many measures have already been implemented/realized or will be implemented in the future (the information was provided by the delegates of the Rhine bordering states), has been included into the calculations.

Depending on the type of measure or indicator (influence on the damage potential or probability) and the considered receptor of the FD (human health, environment, cultural heritage, and economic activities), the impact of measures is calculated differently in the tool:

- Modification of the damage functions resulting from measures (receptors: economic activity and cultural heritage), as shown in Figure 6.
- Changes in the number of people due to evacuation combined with organizational measures (receptor: human health) (see Section 2.3 and Figure 4).
- Changes in the distance (buffer) of possible consequences arising from potentially hazardous facilities (receptor: environment).
- In the case of various measures, the effect is differentiated if the area is protected/embanked or unprotected/non-embanked. In general, it is assumed that, in unprotected areas which are more frequently flooded, potential victims have more flood experience and thus the reduction effect of potential damage is greater.
- In addition to the effect of individual measures, there are interdependencies/correlations between measures that are described in a dependency matrix for both embankment and non-embankment areas. Explanation: if several measures for one area that have an impact on the receptors economic activity and cultural heritage are combined, as a rule, the effect of the measure cannot be summed up in a simple manner, as there is the possibility that the effect would exceed 100%. Secondly, it is assumed that individual measures only have an effect when supplemented or used in combination with other measures (see examples and matrix in the report no. 237 [7]). The combination of measures that have an impact on human health has also been described in Section 2.3.

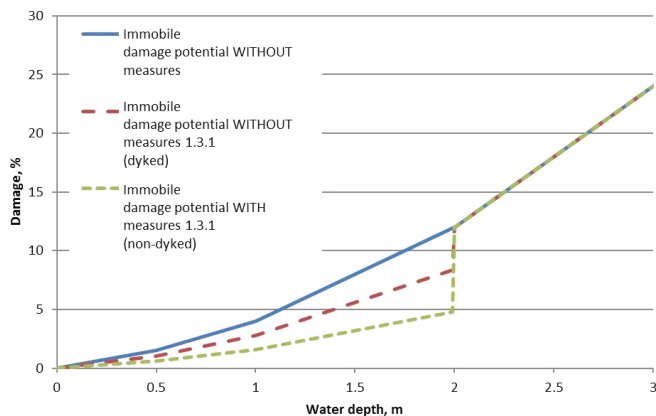


**Figure 6.** Modification of the damage function for immobile damage (industry) due to the measure “precautionary building” (= measure 1.3.1) for dyked and non-dyked areas [7].

## 2.6.2. Change of Flood Probabilities Due to Water Level Reducing Measures

Technical protection measures have an effect on the development of the flood risk, not only due to their influence on flood areas and depths, but also in the case of retention measures (e.g., retention

basin, dyke relocation, measures from “Room for the River” in the Netherlands) and in the context of the ICPR, theoretically by changing the probability of flooding. For the calculations in the Rhine catchment area, retention measures already implemented and planned in the future were taken into account by changing the probabilities (cf. Section 4).

The effectiveness of implemented and planned flood-reducing/water level lowering measures on the Rhine was evaluated by an ICPR expert group which developed a specific method for estimating the change of flood probabilities [22,24]. The results of this method are changed return periods for floods with high, medium, and low probability for different time horizons or Rhine development states (1995, 2005, 2010, 2020 and 2030).

Figure 7 shows an example of the change in probability and return period for an extreme flood event at four selected gauging stations. The Waal (red dotted line) can be used to show the temporal change in the return period of an approximately 1000-year event in 1995 to a 2000-year event in 2030 for an extreme flood. This means that an extreme flood becomes less frequent due to the increase in return period.

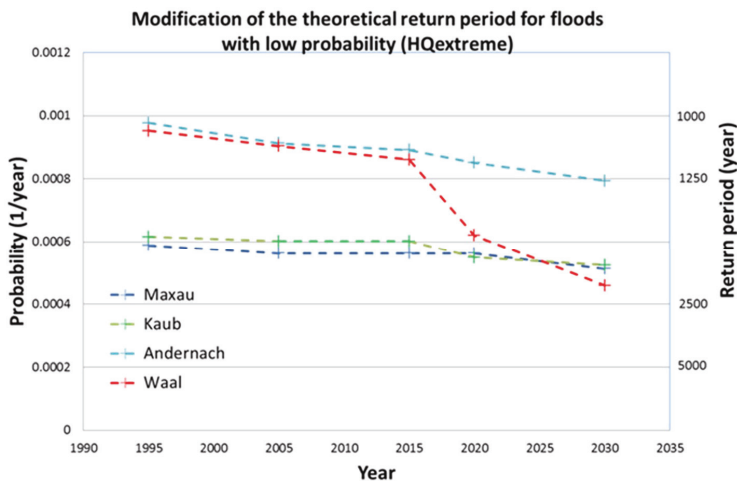


Figure 7. Change of probability (left hand  $y$ -axis) and return period (right  $y$ -axis) for the extreme flood event at four gauging stations [7,8,22].

### 3. Description of the Tool “ICPR FloRiAn”

ICPR FloRiAn was developed in English language and is running as a toolbox of custom tools (compiled C# code) under ESRI ArcGIS Desktop with the extension “ArcGIS Spatial Analyst”. The method described in Section 2 is fully implemented in the tool and represents its backbone. The implementation in the GIS is carried out as a toolbox with four categories along the lines of the four risk receptors of the FD (cf. Figure 8). Each category consists of the following three interacting modules resulting in an overall damage or risk evolution/reduction assessment:

1. Module “Damage assessment”: This module consists of one tool which calculates the damage using land use data, the extension of flood areas (maps), hydraulic data (water depth), asset values and damage functions. The output of this module is used in the next two modules.
2. Module “Measure summation” (this module is optional as the ICPR FloRiAn enables the calculation of flood damage or risk with or without measures): This module quantifies the impact of the different measures (which are introduced with a tool for each measure). Output is a damage reduction (on economic activity, human health, the environment, and cultural heritage) due to the implementation of measures. After the damage reduction for all measures is calculated,

a “summation” tool calculates the damage due to flooding after all measures are incorporated. This tool takes into account the interaction between different measures (the sum of the effect of two tools is not equal to the sum each individual effect) (see end of Section 2.6.1). The output can be used as an input for the next module.

3. Module “Risk assessment”: This module calculates the risk by combining/multiplying the damage potential (output of “damage assessment” or “measure summation”) with the flood probability.
4. The main outputs of the tool are maps with the damage values (actually grids with the damage values per pixel) and tables (\*.dbf files) containing aggregated data for each administrative area as defined in the input (cf. Figure 8). Running the tool for different time horizons (with different input data as well as measures) and comparing the outputs results in the information of damage or risk changes over time.

In addition to the ICPR report no. 237 [7], a technical user guide/manual and a help function in the tool are available [25]. They contain detailed descriptions on the installation and running of the tool, required input data, individual toolboxes (calculation process) as well as the data structure. Originally the tool was developed for ArcGis Desktop 10.0 (ESRI, Redlands, United States), different users have operated the tool under versions 10.2, 10.3, 10.4 and 10.5.

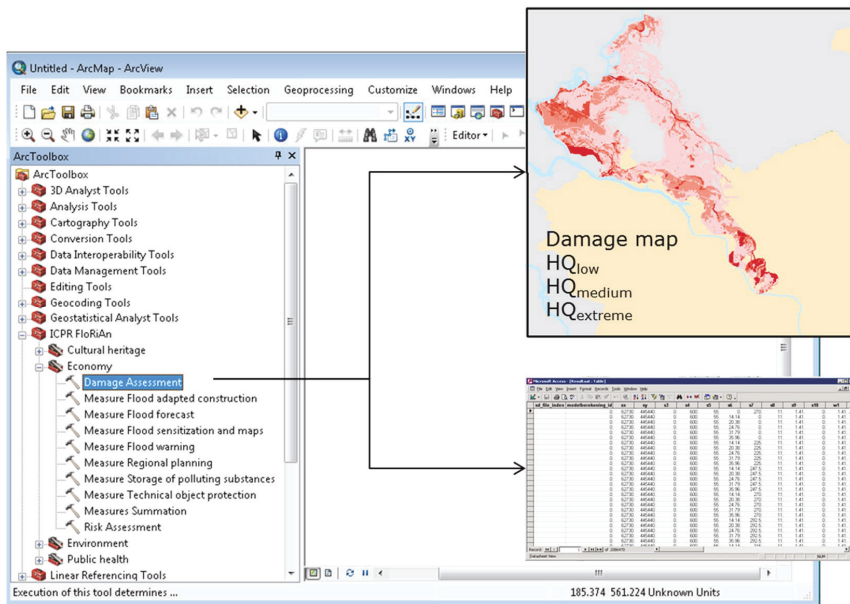


Figure 8. International Commission for the Protection of the Rhine (ICPR) FloRiAn as an ArcToolbox with the four receptors and different calculation modules as well as example of outputs (map and table).

#### 4. Application of ICPR FloRiAn to the Rhine

This section presents the results of the ICPR FloRiAn calculations ran by the ICPR within the assessment of the damage and risk reduction objectives of the ICPR Action Plan on Floods for the four risk receptors human health, environment, cultural heritage and economic activity for the time horizons 1995, 2005, 2015, 2020 and 2030 (with implementation of the respective measures, cf. Table 1) [8]. Realized (until 2015) and planned measures (until 2030) along the Rhine were compiled from the Rhine States and included in the calculations (cf. Table 1). Detailed results and figures can be found in the

ICPR report no. 236 [8]. The assessment and calculations to demonstrate the evolution of the flood risk on the main stream of the Rhine and possible reduction during the period 1995–2030 have revealed the following:

1. When considering the risks to human health, it is apparent that measures such as safeguarding/evacuation of those potentially affected, raising awareness, flood forecasting and warning and alarm plans as well as the modification of the probability of flooding all help to mitigate the flood risk. Across the three flood scenarios, the measures can lead to an average reduction in the risk for human health of approximately 70% to 80% (period 1995–2020) (cf. Figure 9) [8].
2. When assessing cultural heritage and the environment, based on the results of experimental methods (cf. Sections 2.4 and 2.5), the ICPR has found out that, due to the measures undertaken (for the environment: measures helping to mitigate damages of potentially polluting sites, and for cultural heritage: measures like the ones from economic activity, see below), over time, damage and risk to cultural heritage and the environment are reduced from 40% to 70% (period 1995–2020) across all damage categories and all flood scenarios (cf. Figures 10 and 11) [8].
3. In terms of economic activity it has been determined that the reduction by 25% before 2020 (target stated in the APF) compared to 1995 can be achieved. As in the case of the evaluation and calculation of the damage and risk for the other receptors, the ICPR has again performed a broad scale analysis. The latter showed that measures enabling water retention along the Rhine, such as the construction of flood retention areas, the relocation of dykes and measures that give more room to the river are most efficient with respect to changing the probability of flooding (cf. Section 2.6.2 and list of measures in Table 1). In addition, various other measures for prevention and preparedness, including flood forecasting, early warning systems and (pre-) crisis management have contributed to reduce the increase of damage in floodplain areas since 1995 (cf. Figure 12) [8].

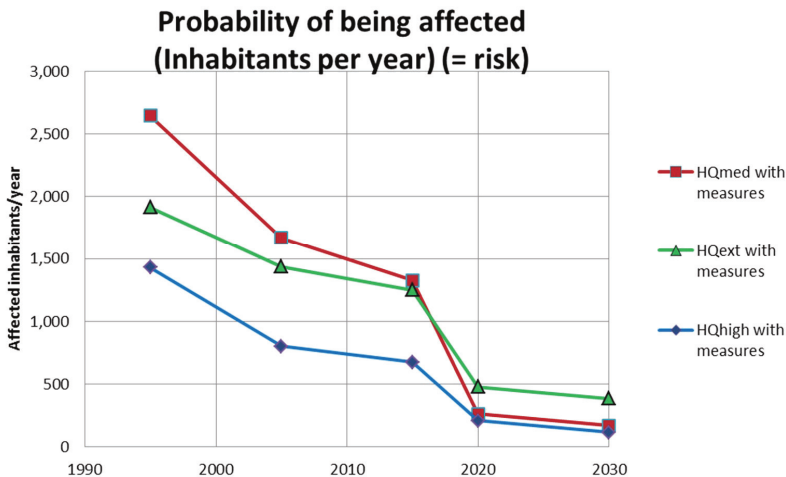


**Figure 9.** Probability of affected inhabitants with consideration of all measures (people affected/year) (= risk) [8].

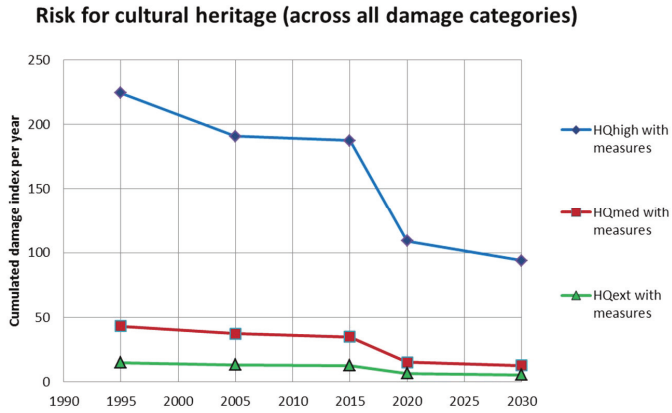


Figure 10. Risk evolution taking into account all measures (total damage index per year across all classes of damage) (Y-axis) [8].

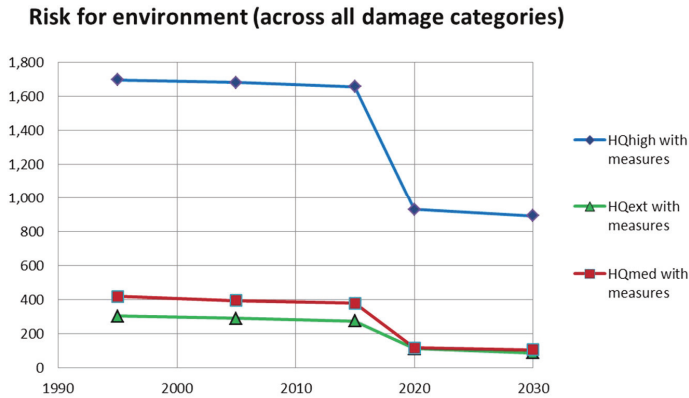


Figure 11. Risk evolution taking into account all measures (total damage index per year across all classes of damage) (Y-axis) [8].

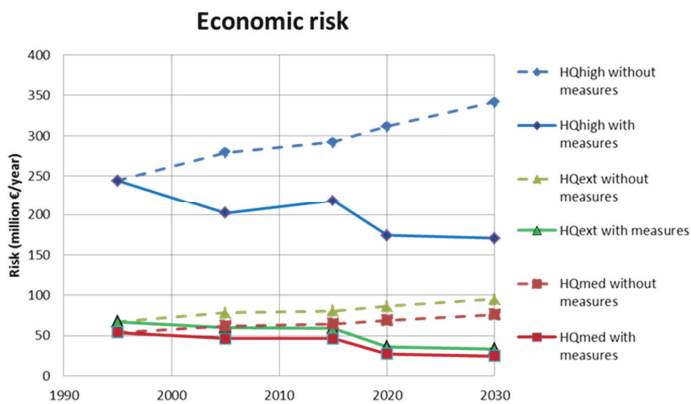


Figure 12. Development/Evolution of economic risk from 1995 to 2030 (€ million/a) [8].

## 5. Conclusions and Outlook

The ICPR has developed the GIS-toolbox ICPR FloRiAn that can be used to quantitatively assess and determine the impact of a set of realized or planned flood risk mitigation measures. Various assumptions were made and different methods were specified or newly developed, some of which are still strongly based on ICPR expert knowledge. In the future, the estimates and assumptions regarding the methods and measures underlying the tool should be optimized by gaining knowledge from the application of the tool by further users and improving input data. Nevertheless, the added value lies in the possibility of a macroscale (e.g., a river basin), temporally comparable and reproducible analysis. Calculations made by the ICPR identified—amongst other results—the reduction of flood risks by 25% between 1995 and 2020 for economic activities. On a broad scale, protection measures increasing water retention along the mainstream of the Rhine proved to be most efficient, but the computations also showed that over time, further non-structural prevention, and preparedness measures also contribute to reducing damage growth in the floodplain. In a nutshell, this means that the whole cycle of flood risk management with a range of preventive and protective actions should be addressed to reduce risks and damages.

The ICPR is planning to use the GIS tool “ICPR FloRiAn” in future to support the flood risk analysis and to determine the effectiveness of measures within the framework of the regular review of the FRMP of the Rhine river basin.

The developed tool can also be applied to other river basins. Upon request, the ICPR provides the tool ICPR FloRiAn and the methods it is based on to other river basin commissions, national authorities, or scientific institutions.

**Author Contributions:** All authors have worked on all parts of the manuscript.

**Acknowledgments:** The contribution is based on the methodology and tool developed together with the HKV consortium and the ICPR expert group HIRI as well as on the calculations carried out. The results of the work are set out in the two technical ICPR reports no. 236 and no. 237 [7,8]. Both reports also indicate which institutions and persons have participated in and contributed to this work. Once again the authors would like to thank all the members of the HIRI expert group: Hendrik Buiteveld (Rijkswaterstaat, NL), Max Schropp (Rijkswaterstaat, NL), Frank Alberts (Rijkswaterstaat, NL), Jean-Pierre Wagner (Direction Régionale de l’Environnement de l’Aménagement et du Logement „Grand Est“, FR), Régis Creusot (Direction Régionale de l’Environnement de l’Aménagement et du Logement „Grand Est“, FR), Anne Toussiro (Direction Régionale de l’Environnement de l’Aménagement et du Logement „Grand Est“, FR), Wolfgang Zwach (Regierungspräsidium Darmstadt, DE), Lennart Gosch (Ministerium für Umwelt, Klima und Energiewirtschaft Baden-Württemberg, DE), Jürgen Reich (Ministerium für Umwelt, Klima und Energiewirtschaft Baden-Württemberg, DE), Barbara Sailer (Ministerium für Umwelt, Klima und Energiewirtschaft Baden-Württemberg, DE), Holger Kugel (Struktur- und Genehmigungsdirektion Nord, Trier, DE), Reinhard Vogt (Stadtentwässerungsbetrieb Köln/Hochwassernotgemeinschaft Rhein, DE), Sabine Siegmund (Stadtentwässerungsbetrieb Köln/Hochwassernotgemeinschaft Rhein, DE), Urs Nigg (Bundesamt für Umwelt, CH), Markus Hostmann (Bundesamt für Umwelt, CH), Andreas Kaufmann (Bundesministerium für Land- und Forstwirtschaft, Umwelt und Wasserwirtschaft, AT), Clemens Neuhold (Bundesministerium für Land- und Forstwirtschaft, Umwelt und Wasserwirtschaft, AT), Gerard Huber (Abteilung Wasserwirtschaft Vorarlberg, AT), Dieter Vondrak (Abteilung Wasserwirtschaft Vorarlberg, AT), Emanuel Banzer (Amt für Bevölkerungsschutz—Landesverwaltung, LI), Catarina Proidl (Amt für Bau und Infrastruktur—Landesverwaltung, LI), Stephan Wohlwend (Amt für Bevölkerungsschutz—Landesverwaltung, LI).

## References

1. International Commission for the Protection of the Rhine. Webpage of the International Commission for the Protection of the Rhine. Available online: <https://www.iksr.org> (accessed on 14 August 2018).
2. International Commission for the Protection of the Rhine. Action Plan on Floods (APF). 1998. Available online: <https://www.iksr.org/en/international-cooperation/rhine-2020/action-plan-on-floods/> (accessed on 14 August 2018).

3. International Commission for the Protection of the Rhine. Brochure “The Rhine and its Catchment—A Survey” (Balance of the implementation of Rhine 2020 and the Action Plan on Floods 1995–2010). 2013. Available online: [https://www.iksr.org/fileadmin/user\\_upload/DKDM/Dokumente/Broschueren/EN/bro\\_En\\_2013\\_The\\_Rhine\\_and\\_its\\_catchment.pdf](https://www.iksr.org/fileadmin/user_upload/DKDM/Dokumente/Broschueren/EN/bro_En_2013_The_Rhine_and_its_catchment.pdf) (accessed on 4 October 2018).
4. International Commission for the Protection of the Rhine. Internationally Coordinated Flood Risk Management Plan for the International River Basin District of the Rhine ((Part A = Overriding Part). 2015. Available online: [https://www.iksr.org/fileadmin/user\\_upload/Dokumente\\_de/Hochwasser/FRMP\\_2015\\_002\\_.pdf](https://www.iksr.org/fileadmin/user_upload/Dokumente_de/Hochwasser/FRMP_2015_002_.pdf) (accessed on 4 October 2018).
5. Directive 2007/60/EC of the European Parliament and of the Council of 23 October 2007 on the Assessment and Management of Flood Risks. 2007. Available online: <https://eur-lex.europa.eu/LexUriServ/LexUriServ.do?uri=OJ:L:2007:288:0027:0034:en:PDF> (accessed on 4 October 2018).
6. Webpage about “ICPR FloRiAn”. Available online: <https://www.iksr.org/en/topics/floods/flood-risk-tool-florian/> (accessed on 14 August 2018).
7. International Commission for the Protection of the Rhine. Report 237: Technical Report “Tool and Assessment Method to Determine Flood Risk Evolution/Reduction”. 2016. Available online: <https://www.iksr.org/en/documentsarchive/technical-reports/synoptical-table/> (accessed on 4 October 2018).
8. International Commission for the Protection of the Rhine. Report 236: Synthesis Report “Assessment of Flood Risk Reduction (APF) According to the Types of Measures and Risk Objects Covered by the FD”. 2016. Available online: <https://www.iksr.org/en/documentsarchive/technical-reports/synoptical-table/> (accessed on 4 October 2018).
9. Albano, R.; Mancusi, L.; Sole, A.; Adamowski, J. FloodRisk: A collaborative, free and open-source software for flood risk analysis. *Geomat. Nat. Hazards Risk* **2017**, *8*, 1812–1832. [CrossRef]
10. Albano, R.; Mancusi, L.; Abbate, A. Improving flood risk analysis for effectively supporting the implementation of flood risk management plans: The case study of “Serio” Valley. *Environ. Sci. Policy* **2017**, *5*, 158–172. [CrossRef]
11. Deckers, P.; Kellens, W.; Reynolds, J.; Vanneuville, W.; De Maeyer, P. A GIS for flood risk management in Flanders. In *Geospatial Techniques in Urban Hazard and Disaster Analysis*; Springer: Dordrecht, The Netherlands, 2009; pp. 51–69.
12. Dottori, F.; Figueiredo, R.; Martina, M.L.V.; Molinari, D.; Scorzini, A.R. INSYDE: A synthetic, probabilistic flood damage model based on explicit cost analysis. *Nat. Hazards Earth Syst. Sci.* **2016**, *16*, 2577–2591. [CrossRef]
13. HAZUS Software (FEMA). Available online: <https://www.fema.gov/hazus>, <https://www.fema.gov/hazus-software> (accessed on 28 September 2018).
14. Moufar, M.M.M.; Edangodage, D.P.P. Floods and Countermeasures Impact Assessment for the Metro Colombo Canal System, Sri Lanka. *Hydrology* **2018**, *5*, 11. [CrossRef]
15. Samela, C.; Albano, R.; Sole, A.; Manfreda, S. A GIS tool for cost-effective delineation of flood-prone areas. *Comput. Environ. Urban Syst.* **2018**, *70*, 43–52. [CrossRef]
16. FLIWAS (Flutinformations- und Warnsystem). Available online: <https://www.hochwasser.baden-wuerttemberg.de/flutinformations-und-warnsystem> (accessed on 28 September 2018).
17. OSIRIS-Inondation. Available online: <http://www.osiris-inondation.fr/index.php?init=1> (accessed on 28 September 2018).
18. SD-KAMA (Smart Data-Katastrophenmanagement). Available online: [https://www.sd-kama.de/en/smart\\_data\\_disaster\\_management/](https://www.sd-kama.de/en/smart_data_disaster_management/) (accessed on 28 September 2018).
19. Peter, M. Dynamische Einsatzplanung—Big Data im Rettungsdienst. In *Herausforderung Notfallmedizin*; Springer: Berlin/Heidelberg, Germany, 2018; pp. 143–152.
20. Grossi, P.; Kunreuther, H.; Windeler, D. An introduction to catastrophe models and insurance. In *Catastrophe Modeling: A New Approach to Managing Risk*; Springer: Boston, MA, USA, 2005; pp. 23–42.
21. International Commission for the Protection of the Rhine. Rhine Atlas 2015 (Flood Hazard and Risk Maps of the International River Basin District ‘Rhine’). Available online: <https://www.iksr.org/en/documentsarchive/rhine-atlas/> and direct link [http://geportal.bafg.de/mapapps/resources/apps/ICPR\\_EN/index.html?lang=en](http://geportal.bafg.de/mapapps/resources/apps/ICPR_EN/index.html?lang=en) (both accessed on 14 August 2018).

22. International Commission for the Protection of the Rhine. Report 229: Assessment of the Modification of Probability Due to Flood Level Reduction Measures along the Rhine. 2015. Available online: <https://www.iksr.org/en/documentsarchive/technical-reports/synoptical-table/> (accessed on 4 October 2018).
23. International Commission for the Protection of the Rhine. Rhine Atlas 2001 (Methodology) and Key Document for the Creation of the Atlas “Übersichtskarten der Überschwemmungsgefährdung und der Möglichen Schäden bei Extremhochwasser am Rhein—Vorgehensweise zur Ermittlung der Überschwemmungsgefährdeten Flächen Sowie Vorgehensweise zur Ermittlung der Vermögenswerte”. Available online: [https://www.iksr.org/fileadmin/user\\_upload/Dokumente\\_de/Rhein-Atlas/german/welcome\\_german.pdf](https://www.iksr.org/fileadmin/user_upload/Dokumente_de/Rhein-Atlas/german/welcome_german.pdf) (accessed on 14 August 2018).
24. International Commission for the Protection of the Rhine. Report 199: Evidence of the Effectiveness of Measures Aimed at Reducing Flood Levels of the Rhine. 2012. Available online: <https://www.iksr.org/en/documentsarchive/technical-reports/synoptical-table/> (accessed on 4 October 2018).
25. International Commission for the Protection of the Rhine. User’s Guide to ICPR FloRiAn. (not published). 2016.

# Assessment of the Performance of Satellite-Based Precipitation Products for Flood Events across Diverse Spatial Scales Using GSSHA Modeling System

Chad Furl, Dawit Ghebreyesus and Hatim O. Sharif \*

Department of Civil and Environmental Engineering, University of Texas at San Antonio, 1 UTSA Circle, San Antonio, TX 78249, USA; chad.furl@gmail.com (C.F.); dawit.ghebreyesus@my.utsa.edu (D.G.)

\* Correspondence: hatim.sharif@utsa.edu

**Abstract:** Accurate precipitation measurements for high magnitude rainfall events are of great importance in hydrometeorology and climatology research. The focus of the study is to assess the performance of satellite-based precipitation products against a gauge adjusted Next-Generation Radar (NEXRAD) Stage IV product during high magnitude rainfall events. The assessment was categorized across three spatial scales using watershed ranging from  $\sim 200$ – $10,000$  km<sup>2</sup>. The propagation of the errors from rainfall estimates to runoff estimates was analyzed by forcing a hydrologic-model with the satellite-based precipitation products for nine storm events from 2004 to 2015. The National Oceanic and Atmospheric Administration (NOAA) Climate Prediction Center (CPC) Morphing Technique (CMORPH) products showed high correlation to the NEXRAD estimates in all spatial domains, and had an average Nash-Sutcliffe coefficient of 0.81. The Global Precipitation Measurement (GPM) Early product was inconsistent with a very high variance of Nash-Sutcliffe coefficient in all spatial domains (from  $-0.46$  to  $0.38$ ), however, the variance decreased as the watershed size increased. Surprisingly, Tropical Rainfall Measuring Mission (TRMM) also showed a very high variance in all the performance statistics. In contrast, the un-corrected product of the TRMM showed a relatively better performance. The errors of the precipitation estimates were amplified in the simulated hydrographs. Even though the products provide evenly distributed near-global spatiotemporal estimates, they significantly underestimate strong storm events in all spatial scales.

**Keywords:** hydrology; NEXRAD; remote sensing; GSSHA; flooding; GPM

---

## 1. Introduction

Accurate precipitation measurements for high magnitude events are of key importance to a number of areas in hydrometeorology and climatology research. In addition to research pursuits, these measurements have great value to public well-being by providing the backbone of rainfall-runoff prediction systems aimed at forecasting floods [1,2]. Over the past couple of decades in operational settings, these datasets have primarily been generated with radar and rain gauge networks [3]. Radar networks have the advantage of providing near real-time information over a continuous region at very fine scales, mostly unattainable with ground-based gauge networks. Numerous validation studies showed good performance of radar measurements, especially when combined with gauge networks for bias adjustments/quality control (e.g., Wang, Xie [4], Habib, Larson [5]). However, lack of even global distribution of radar network and problems such as beam blockage in complex terrain introduced significant gaps in radar coverage that pushed researchers to explore robust solution [6].

Satellite precipitation estimates provide a means for timely, near-global precipitation estimates, and much of the recent effort has been put into their validation and verification [7–13]. Several products, including those provided by the recently launched Global Precipitation Measurement (GPM)

mission, now provide the spatiotemporal resolution needed to forecast or conduct post-event analysis of flash floods. Even though the potential of satellite-based products was highly regarded, their poor performances were reported widely across the globe, especially, in their ability to accurately capture high magnitude precipitation events. Nikolopoulos, Anagnostou [14] demonstrated mean areal precipitation is consistently underestimated in their satellite ensemble analysis of a high magnitude precipitation event in Italy. AghaKouchak, Behrangi [15] examined several operational satellite precipitation products across the southern Great Plains with respect to precipitation thresholds and demonstrated the detection skill reduces as the choice of extreme threshold decreases. Mehran and AghaKouchak [16] reported similar findings when comparing three operational satellite products across the conterminous United States. Mei, Anagnostou [17] showed that satellite precipitation estimates are more biased for frontal events than for short-duration events. However, the error statistics of the products showed higher variability for the latter. Moreover, the products showed high inconsistency across different terrain [12] and climatic conditions [11]. These and other studies stress the need for more analysis and evaluation of the accuracy and performance of recent satellite products in capturing the behavior of extreme precipitation events by comparing them against products from ground-based measurement networks (radar or rain gauges).

Satellite-based precipitation products were found to be more accurate in a dry season and in wet tropical and dry zones than in semi-arid and mountainous regions. The uncertainty amongst the products was higher in estimating heavy rainfall storms in a semi-arid area. Moreover, the products, in general, overestimate the number of rainy days and underestimate the heavy rainfall storms [11]. Amongst the highly cited satellite-based products in the literature, the National Oceanic and Atmospheric Administration (NOAA) Climate Prediction Center (CPC) Morphing Technique (CMORPH) and Precipitation Estimation from Remotely Sensed Information using Artificial Neural Networks (PERSIANN) were reported to be spatially inconsistent [10–12,18–20]. The Tropical Rainfall Measuring Mission (TRMM) and its continuation mission GPM were found in many studies to be relatively consistent and more accurate but overestimated the average rainfall events and underestimated the heavy storm events in general [11–13,19,21].

The potential of high-resolution satellite precipitation estimates in hydrological applications is supported by the facts that satellite measurements are not inhibited by local topography and are available at a global scale. Forcing hydrological models with high-resolution satellite-based precipitation products can provide a streamflow forecast for ungauged, complex terrain basins. The manner in which rainfall errors propagate through a hydrologic model has important implications for building operational flow forecasts for such basins. Propagation of errors is influenced by spatial and temporal resolution of the satellite estimate, basin scale, and complexity of the physical interactions represented by the watershed model, among others. Presently, the majority of detailed error propagation studies were forced with radar rainfall data (e.g., Sharif, Ogden [22], Sharif, Ogden [23,24], Vivoni, Entekhabi [25]) with comparatively less work done for satellite-based precipitation (e.g., Nikolopoulos, Anagnostou [14], Gebregiorgis, Tian [26], Maggioni, Vergara [27], Chintalapudi, Sharif [28]). Moreover, most of the studies forced by satellite-based precipitation on propagation error into hydrologic predictions were focused on grid-based evaluation or long-term basin-averaged runoff response (e.g., Su, Gao [29], Wu, Adler [30]).

Spatial scale (with respect to both satellite resolution and basin size) is an important aspect in rainfall-to-runoff error propagation for satellite precipitation, and a more comprehensive understanding of it plays a vital role in mitigation of natural disasters. Nikolopoulos, Anagnostou [14] developed satellite rainfall ensembles for a single flood event and showed error propagation is strongly related to the size and characteristics of the watershed and the satellite product resolution. A rainfall-runoff process reduces the satellite-precipitation error variance in a mild-sloped catchment, and this effect exhibits the basin-scale dependence [31]. However, many other factors also have a significant impact, such as precipitation type, magnitude, and spatiotemporal pattern, and basin characteristics interact with the scale effect [31–33].

The Gridded Surface Subsurface Hydrologic Analysis (GSSHA) model, which is fully distributed and physically-based, was developed by the Department of Defense in order to simulate surface flows in non-Hortonian watersheds and watersheds with diverse characteristics of runoff production [34]. The model employs a mass-conserving solution of partial differential equations to produce the different components of hydrologic processes. The model was able to reproduce stream flows from a very diverse watershed with reasonable accuracy [35]. Moreover, the grid size can be used to optimize the required accuracy with the required computational power [36].

In the present study, the performance of several satellite precipitation products with respect to gauge corrected ground-based radar estimations for nine moderate to high magnitude events across the Guadalupe River system in south Texas was investigated. The analysis was conducted across three nested watersheds (ranging from 200 to 10,000 km<sup>2</sup> in area) to capture and quantify the effect of the scale on the propagation of the error. Satellite-based precipitation data sets were used to force a fully distributed physics-based Gridded Surface Subsurface Hydrologic Analysis (GSSHA) model to examine error propagation through the hydrologic model. Both gauge-corrected and uncorrected satellite products were used, encompassing a variety of latency times, spatial resolutions, and temporal resolutions. Satellite-based precipitation datasets used in the study include various products from GPM, PERSIANN system, CMORPH, and TRMM.

## 2. Materials and Method

### 2.1. Watershed

The Guadalupe River originates in south-central Texas and flows southeasterly until emptying into the Guadalupe estuary/Gulf of Mexico. In this study, the testbed is the middle and upper portions of the basin, with the watershed outlet taken near Gonzales, TX past the confluence of the Guadalupe and San Marcos rivers (herein referred to as Guadalupe basin). At the outlet, the basin drains approximately 9000 km<sup>2</sup>. Two additional catchments within the watershed were delineated for scale effect analysis: Little Blanco River (178 km<sup>2</sup>) and the Blanco River (1130 km<sup>2</sup>). The spatial extent of the Guadalupe watershed along with the two nested watersheds is shown in Figure 1. Canyon Lake reservoir is formed by an impoundment along the Guadalupe River and contains significant flood storage, thus, we removed the dam from our watershed model to simulate a naturally flowing river for the analysis of hydrograph error propagation.

The Guadalupe River flows across distinct landscapes with varying hydrological characteristics. The upper portion of the watershed is located in an area known as the Texas Hill Country. This region is comprised of a karstic landscape with steep surfaces, exposed bedrock, and very thin clayey soils. As the river passes through the Balcones Escarpment, it encounters the Edwards Aquifer recharge and artesian zones. In these regions, soils are permeable and there is much groundwater-surface water interaction. The lower portion of the river crosses the Blackland Prairies before entering the Coastal Plain. A generalized soil map of the study area including the recharge and artesian areas of the Edwards Aquifer is displayed in Figure 1. There are a number of studies available describing the surface characteristics of the watershed in detail along with its flood hydrology [36–38].

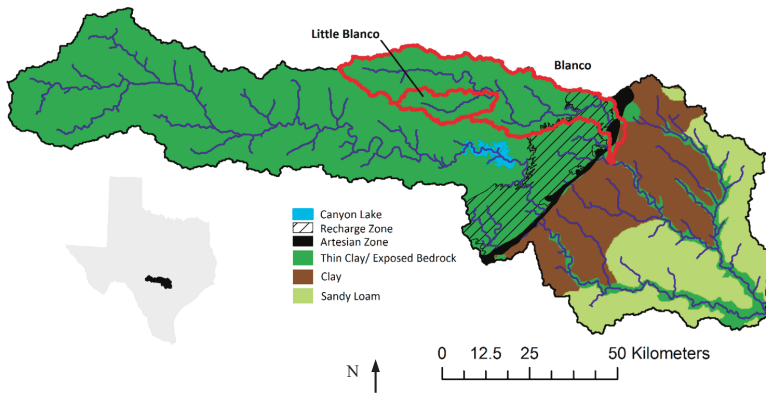


**Figure 1.** Location and area map of the study watersheds along with a generalized soil map. Each of the three interior watersheds are outlined, and the Edwards Aquifer recharge and artesian zones are displayed.

## 2.2. Storm Events

The Texas Hill Country is one of the most flash flood-prone areas of the entire United States due to its flood-prone physiography and susceptibility to extreme precipitation [38,39]. Although not considered among the very humid regions of the U.S., proximity to the Gulf of Mexico allows for extremely moist tropical air masses to reach the Balcones Escarpment where they can be subjected to orographic lift [40]. The region holds or has held several precipitation world records on time scales less than 24 h (USGS 2014). The precipitation envelope curve for Texas is comprised mostly from events in this region with others from the coastal plain. Once precipitation falls, the availability of steep slopes, high drainage density, exposed bedrock, and clay-rich soils have the ability to produce extremely high runoff coefficients with short lag times [41].

Here, nine large precipitation events from 2004–2015 across the middle Guadalupe basin were selected to examine satellite precipitation estimate performance and hydrologic model error propagation. All of the storm event accumulations from the Stage IV precipitation record are presented in Figure 2. The hydrometeorology of several of these events has been examined in detail including Furl, Sharif [42] (May 2015 event), Furl, Sharif [40] (September 2010 event), and Sharif, Sparks [36] (November 2004 events).

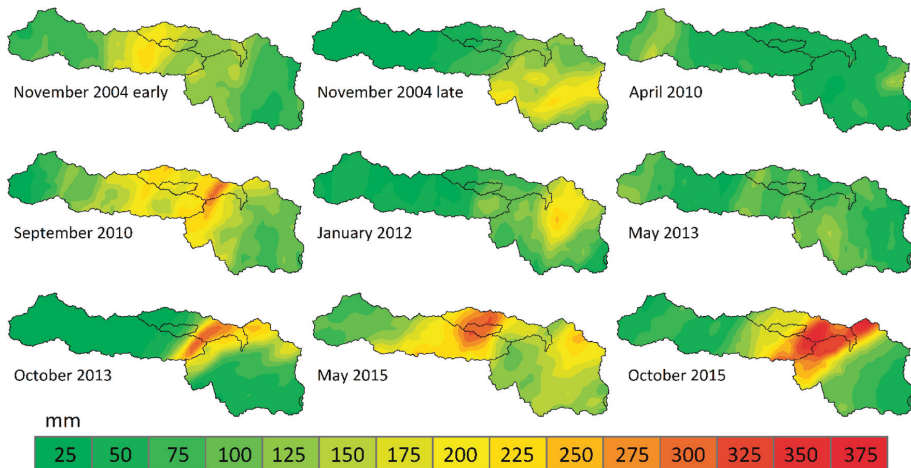


**Figure 2.** Total accumulations from stage IV data for individual storm events used in the analysis (mm). The month and year in which the storm occurred is displayed along with outlines of the interior watersheds. Numbers along the legend represent the maximum value from each category.

### 2.3. Precipitation Datasets

In total, ten satellite precipitation products were examined, encompassing a variety of spatiotemporal resolutions. Moreover, the examined products include gauge corrected and uncorrected products to assess the impact of the adjustment. A brief description of the precipitation products is included below.

#### 2.3.1. NEXRAD Stage IV

Each of the satellite precipitation datasets was compared to the National Weather Service (NWS) and the National Centers for Environmental Prediction (NCEP) stage IV Quantitative Precipitation Estimate (herein Stage IV) [43]. The precipitation estimate is a quality controlled multi-sensor product (radar and gauges) produced by NCEP from the NEXRAD Precipitation Processing System [44] and the NWS River Forecast Center precipitation processing [45]. Precipitation bins are  $4 \text{ km} \times 4 \text{ km}$  and have an hourly temporal resolution. The primary radar operating across the study area is National Weather Service in Austin/San Antonio (KEWX) station approximately 70 km from the watershed outlet.

The authors acknowledge the inherent biases that accompany radar-based precipitation estimates. However, the relatively fine space-time scales of the dataset provide the best means to describe the spatiotemporal heterogeneity of the rainfall across the basin and make satellite comparisons. Moreover, previous studies by the authors demonstrated that Stage IV products were more suitable than observations by typical rain gauge networks as inputs to physically based distributed-parameter models (e.g., [28,36]).

#### 2.3.2. GPM

The GPM core observatory was launched on 27 February 2014 providing a new means of satellite global precipitation measurement. The GPM consists of a core-satellite and numerous others in its constellation. The GPM mission is based on a constellation of microwave radiometers and integrated IR sensors to cover the blind spot of the microwave sensors. The Integrated Multi-Satellite Retrievals for GPM (IMERG) is the precipitation product developed by the GPM network. The core GPM satellite carries a dual-frequency precipitation radar along with multichannel microwave imagers and is used for calibration of the constellation satellites. Additionally, GPM can integrate infrared (IR)

measurements from geostationary data to cover areas not seen by constellation satellites. The data produces a near global precipitation product with a spatial resolution of  $0.1^\circ$  and 30-min temporal resolution [46,47].

IMERG output is available in Early, Late, and Final runs, with a latency of approximately 4 h, 18 h, and 4 months, respectively. The Final IMERG run is calibrated by monthly gauge precipitation data following a certain procedure (Huffman, Bolvin [46]). In the present study, version 3 processing algorithms were used, and each of the three IMERG products were examined.

### 2.3.3. PERSIANN

The PERSIANN system estimates rainfall from infrared image data provided by geostationary satellites. PERSIANN data are calibrated in real time from independent microwave precipitation estimates. The calibration process is based on an adaptive training technique which updates neural network parameters when microwave data are available [48]. The data are available in  $0.25^\circ$ , 30-min resolution approximately 2 days after the gridded IR images are collected. The rainfall product covers tropical and middle latitudes from 50 S to 50 N [48,49].

PERSIANN-Cloud Classification System (PERSIANN-CCS) allows for precipitation estimates at the same temporal resolution and a finer spatial resolution ( $0.04^\circ$ ). Additionally, the data are available in near real-time. The system allows for the discernment and classification of cloud patch features based on height, areal extent, and variable texture. These classifications are used to further refine the assignment rainfall within each cloud. The product with a latency of two days was used for PERSIANN-CCS in this study.

### 2.3.4. CMORPH

CMORPH estimates precipitation from microwave-based precipitation images advected in time using infrared images from geosynchronous satellites. The product combines the positive side of the two satellites: estimated precipitation from low orbited satellites using microwave images and transportation of the estimated precipitation in time using the IR from the geosynchronous satellites. Microwave images are much better in estimating precipitation but they are not continuous, and IR from geosynchronous satellites are available and are continuous in time. The precipitation product is available at 30 min intervals with 8 km resolution as well as 3-h,  $0.25^\circ$  resolution. Precipitation estimates are available approximately 18 h past instrument measurement [50]. CMORPH products used in this study include the raw satellite-only precipitation product (CMORPH\_RAW), the climate data record (CDR) version (CMORPH\_CDR) and the published 8 KM resolution product CMORPH\_8KM.

### 2.3.5. TRMM

The Tropical Rainfall Measuring Mission (TRMM) employs a combination of microwave and IR data to estimate precipitation at  $0.25^\circ$  every 3 h. The TRMM product is produced by combining microwave estimates which are used to calibrate IR estimates from geosynchronous satellites. The IR estimates are used to fill gaps left by the microwave sensors. TRMM 3B42 V7 and TRMM-RT 3B42 V7 were used in the study. Gridded monthly rain gauge values are used to adjust the TRMM 3B42 V7 estimates [51]. The TRMM-RT (Real-Time) product is a near real-time dataset with no gauge adjustments. An overview of the availability of the entire dataset is shown in Table 1.

**Table 1.** Description of satellite precipitation dataset availability.

	Nov. 2004 Early	Nov. 2004 Late	Apr. 2010	Sept. 2010	Jan. 2012	May 2013	Oct. 2013	May 2015	Oct. 2015	Gauge Adjusted
TRMM B42	x	x	x	x	x	x	x	x	x	Y
TRMM-RT B42	x	x	x	x	x	x	x	x	x	N
PERSIANN	x	x	x	x	x	x	x	x	x	N
PERSIANN CCS	x	x	x	x	x	x	x	x	x	N
CMORPH CDR	x	x	x	x	x	x	x	NA	NA	Y
CMORPH 8KM	x	x	x	x	x	x	x	NA	NA	Y
CMORPH RAW	x	x	x	x	x	x	x	x	x	N
GPM IMERG EARLY	NA	NA	NA	NA	NA	NA	NA	x	x	N
GPM IMERG LATE	NA	NA	NA	NA	NA	NA	NA	x	x	N
GPM IMERG FINAL	NA	NA	NA	NA	NA	NA	NA	x	x	Y

2.4. Hydrologic Model

Precipitation datasets were used to force the fully distributed physics-based GSSHA model [34,52]. Hydrological processes simulated included infiltration, landscape retention, overland flow, and stream routing. Evapotranspiration and deep aquifer contributions were assumed to be insignificant relative to the processes since the simulation is event based. Model preprocessing was conducted using ArcGIS and Aquaveo’s Watershed Modeling System. Watershed terrain was constructed from USGS 10 m digital elevation models (DEM) filled using the Cleandam algorithm distributed with the GSSHA model. Land use and land cover data were extracted from the National Land Cover Database 2011 (NLCD 2011) dataset. Soils data were prepared from SSURGO datasets along with maps from the Edwards Aquifer Authority defining the Edwards Aquifer recharge zone.

Infiltration calculations were conducted using Green and Ampt with redistribution [53] and pre-calibrated saturated hydraulic conductivity values taken from Rawls, Brakensiek [54]. Grid cells were assigned to one of four land use classes for retention and overland roughness. Stream channels were modeled using irregular cross sections for the main channel and large tributaries. The irregular channel and floodplain geometry were extracted from a triangular irregular network constructed from the DEM allowing for control of floodplain simulation. Upland tributaries were modeled as a uniform trapezoidal profile. Reach specific Manning’s n values were assigned based on field observations and prior modeling experience in this region of Texas. Routing was calculated using the diffusive wave equation in 1D for streams and 2D for overland flow. The hydrological model was run on a 150-m grid cell size with a 1-min simulation time step.

Distributed models have the distinct advantage of allowing examination of hydrologic properties at any point in the basin. In this study, three watershed models were constructed: Blanco watershed, Upper Guadalupe watershed, and Middle Guadalupe watershed. Results from the Little Blanco watershed were harvested from the proper interior node of the Blanco River watershed model. The Middle Guadalupe model (i.e., implementation of the hydrologic model over Middle Guadalupe) used streamflow from the outlets of the Blanco and Upper Guadalupe as boundary condition inflows, thereby allowing a very fine gridded distributed model over a 9000 km<sup>2</sup> basin. The Upper Guadalupe model discharge hydrograph was input into the Middle Guadalupe at the outlet of Canyon Lake, bypassing the reservoir.

The Blanco watershed model was the primary model calibrated. Furl et al. [42] calibrated the model to the November 2004 “early” event used here and achieved r<sup>2</sup>, Nash-Sutcliffe model efficiency (NSE), and percent bias (PBIAS) values of 0.91, 0.90, and 10.2%, respectively for the calibration run. Similar model parameter values were used for the Upper Guadalupe model. The setup for the Middle Guadalupe followed hydrologic parameters described by Sharif, Sparks [36], which described the November 2004 “late” event. It should be noted that our main objective with model calibration is to provide realistic rainfall-runoff mechanisms such that error propagation analysis can be conducted. Surface properties for the Blanco River watershed are shown in Table 2. The readers are directed to Sharif, Sparks [36] and Furl et al. [42] for detailed descriptions of the watershed models and their comparisons with measured flows.

**Table 2.** Gridded Surface Subsurface Hydrologic Analysis (GSSHA) infiltration and overland flow parameters for the Blanco watershed model.

Soil Texture/ Land Use	Saturated Hydraulic Conductivity (cm·hr <sup>-1</sup> )	Capillary Head (cm)	Effective Porosity	Manning's Roughed Coefficient	Retention Depth (mm)
Recharge zone	10.0	23.6	0.417	-	-
Clay	1.2	0.06	0.385	-	-
Loam	0.01	1.3	0.434	-	-
Fine loam	0.02	2.18	0.412	-	-
Fine silt	0.01	0.68	0.486	-	-
Fine sand	0.03	23.6	0.417	-	-
Urban	-	-	-	0.18	5.0
Forest	-	-	-	0.25	5.0
Shrub	-	-	-	0.20	5.0
Grasslan/agriculture	-	-	-	0.30	5.0

### 2.5. Evaluation Criteria

Satellite precipitation results were analyzed by comparing mean areal precipitation hyetographs with those generated from the Stage IV precipitation record. Here, the reference hydrographs were those driven by the reference precipitation product (radar). It will not be appropriate to use observed hydrographs as a reference since we do not have a precipitation product that will perfectly produce the observed hydrographs. A weighting method was used in the averaging routine to account for rainfall bins only partially covering a portion of the basin. For comparisons, satellite hyetographs were scaled to a one-hour time step using a simple linear transformation in order to match the Stage IV record. The comparison period was confined to when the Stage IV record indicated 1 mm of precipitation had fallen across the basin until rainfall ceased. Streamflow hydrograph comparisons were conducted in a similar manner by comparing satellite generated model output with the hydrograph generated by the Stage IV record. The analysis period was determined by visually examining the Stage IV generated hydrographs and capturing from just before the rising limb of the hydrograph until after the falling limb. The comparisons for hyetographs and hydrographs were completed using the percent bias (PBIAS), normalized root-mean-square-error (nRMSE), and Nash-Sutcliffe model efficiency (NSE) statistics. Simple relative error in precipitation, peak flow, and volume of flow was calculated for error propagation analysis. Calculations were completed using the hydroGOF package [55] in R environment as follows:

$$PBIAS = 100 \times \frac{\sum_{i=1}^N (S_i - O_i)}{\sum_{i=1}^N O_i} \quad (1)$$

$$nRMSE = 100 \times \frac{\sqrt{\frac{1}{N} \sum_{i=1}^N (S_i - O_i)^2}}{nval} \quad (2)$$

$$\text{where } nval = \begin{cases} sd(O_i), & \text{norm} = "sd" \\ O_{max} - O_{min}, & \text{norm} = "maxmin" \end{cases}$$

$$NSE = 1 - \frac{\sum_{i=1}^N (S_i - O_i)^2}{\sum_{i=1}^N (O_i - \bar{O})^2} \quad (3)$$

$$\text{relative error}(\delta x) = \frac{\Delta x}{x} = \frac{x_0 - x}{x} = \frac{x_0}{x} - 1 \quad (4)$$

where:

$S_i$  is the simulated rainfall (estimated by the product),

$O_i$  is the estimated rainfall by NEXRAD stage IV,

$x_0$  is the estimated rainfall by the product/precipitation/simulated peak flow with the product, and

$x$  is the estimated rainfall NEXRAD stage IV/simulated peak flow with NEXRAD stage IV rainfall.

3. Results and Discussion

3.1. Precipitation

Precipitation from the Stage IV record averaged over the entire watershed ranged from approximately 50–150 mm, and storm durations lasted from just a few hours to approximately 72 h. Among the 27 isolated storm event and watershed size combinations (9 storm events  $\times$  3 watersheds), the satellite-based precipitation products showed a wide range level of accuracy when compared to the Stage IV estimates. As shown in Figure 3, for the largest spatial domain, satellite precipitation estimates showed the ability to very closely match radar results (November 2004 (late), May 2013), and consistently overestimate (November 2004, early) and also systematically underestimate precipitation (October 2015). The products tended to significantly underestimate in four events and only once overestimated when compared to NEXRAD Stage IV estimates. In addition to the inherent errors in the satellite products due to calibration and the rainfall estimation technique (i.e., microwave or infrared), the relatively coarse resolution of the products may have contributed to the underestimations errors. Underestimation is more pronounced for the large events where satellite underestimates the high intensity periods. Interestingly, the Final GPM product underestimates rainfall more than the earlier products. This can also be attributed to the nature of the events where climatology and gauge adjustments did not capture the localized intensity of the events. In the rest of the four storm events, the NEXRAD product seemed to fit the average of all the satellite-based products (Figure 3). The satellite-based products failed to capture the storm events that occurred in the Fall (September, October) with the exception of the 2004 storm where they tended to overestimate the storm. In contrast, the margin of error was very low in storm events that occurred in May.

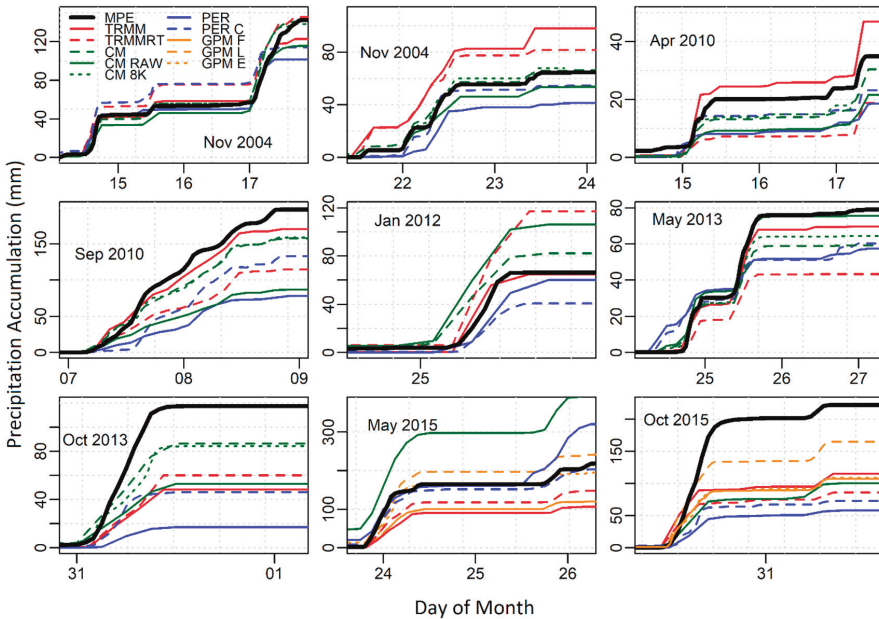


**Figure 3.** Storm event rainfall accumulations averaged over the Blanco watershed. Legend labels are abbreviated as follows: MPE—Stage IV, TRMM—TRMM 3B42, CM—CMORPH CDR, GPM F—GPM IMERG FINAL, CM 8K—CMORPH 8KM, PER C—PERSIANN CCS, GPM E—GPM IMERG EARLY, GPM L—GPM IMERG LATE, CM RAW—CMORPH RAW, TRMM-RT—TRMM-RT 3B42, and PER—PERSIANN.

In general, the satellite products (adjusted and unadjusted) underestimated the storm events from the stage IV record at all spatial scales with the exception of some storm events. This is not surprising given the small sample size focused on events on the tail side of the distribution. Other researchers have noted similar satellite underestimations for high magnitude events [14–16,56]. However, it should be noted there was no strong correlation between percent bias and total accumulated precipitation for any of the three spatial domains. Moreover, satellite-based products underestimated heavy storm events in larger spatial domains (0.4 to 1.3 million km<sup>2</sup>) in several regions of Africa [11].

Generally, the satellite-based precipitation products showed less variability in the case of the Guadalupe basin (Large) relative to the two smaller watersheds (Figure 4). This could be mainly because of the smoothing power of mean value over the large spatial domain (filtering the noise introduced by the products). Both products from CMOPRH (labeled as CM and CM 8K) showed very high correlation with the stage IV product in all spatial domains with very high Nash coefficient. GPM Early was found to be inconsistent with a very high variance of Nash coefficient in all spatial domains, however, the variance was decreased as the watershed size increase. Surprisingly, TRMM showed a very high variance in all the performance statics, especially in the two small watersheds. In contrast, the TRMM-RT product showed relatively better performance. As described above, the performance of GPM Final product was inferior to the earlier ones. The whole distribution of the performance statistics is provided in Figure 4.

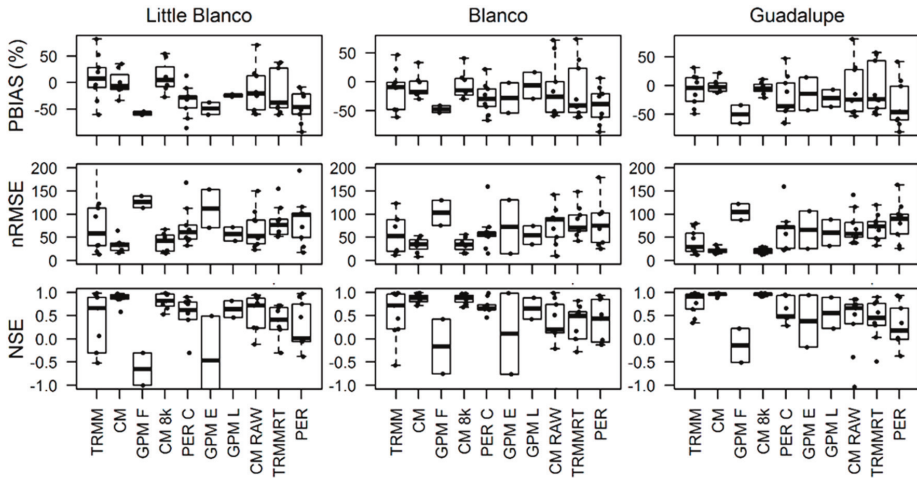


**Figure 4.** Boxplots for hyetograph performance statistics for all spatial domains. X-axis labels are abbreviated as follows: TRMM—TRMM 3B42, CM—CMORPH CDR, GPM F—GPM IMERG FINAL, CM 8K—CMORPH 8KM, PER C—PERSIANN CCS, GPM E—GPM IMERG EARLY, GPM L—GPM IMERG LATE, CM RAW—CMORPH RAW, TRMM-RT—TRMM-RT 3B42, and PER—PERSIANN. Boxplots display the lower and upper quartiles and median. Whiskers extend to the data point nearest  $\pm 1.5 \cdot$  interquartile range.

In order to provide some comparison between satellites products, performance statistic results were pooled from all spatial domains for each individual satellite product. Table 3 displays the median, average, and range of the statistics after this aggregation. For the 0.25° uncorrected products, performance statistics indicated CMORPH RAW > TRMM-RT > PERSIANN for the nine events examined. Sapiano and Arkin [10] found that correlations were highest with CMORPH in an inter-comparison and validation study on sub-daily satellite precipitation data. For the gauge corrected products at 0.25°, there was very little difference between TRMM and CMORPH when the same events were compared (2015 events unavailable for CMORPH). It is difficult to draw conclusions about the

performance of GPM given that only two events were measured. GPM results are compared to the other products for the 2015 events below.

**Table 3.** Satellite hyetograph performance statistics aggregated across the three spatial domains.

		Gauge Correction					No Gauge Correction				
		TRMM	CMORPH	GPM FINAL	CMORPH 8KM	PERSIANN CCS	GPM EARLY	GPM LATE	CMORPH RAW	TRMM-RT	PERSIANN
Average	PBIAS	-3.9	-2.9	-51.9	0.2	-28.2	-30.4	-17.6	-12.2	-14.2	-39.7
	nRMSE	58.2	29.5	111.2	31.4	66.9	83.5	57.3	72.3	79.3	84.1
	NSE	0.42	0.89	-0.32	0.87	0.38	0.01	0.62	0.32	0.26	0.06
	PBIAS	-4.4	-7.0	-54.1	-4.6	-29.7	-40.3	-24.3	-24.7	-37.2	-46.3
	nRMSE	48.0	26.9	117.8	28.0	59.8	88.7	57.2	67.9	73.2	90.0
Median	NSE	0.77	0.93	-0.40	0.92	0.63	0.16	0.64	0.53	0.45	0.18
	PBIAS	143.1	69.3	32.1	84.3	132.5	74.8	54.0	140.4	135.2	134.0
	nRMSE	210.7	56.5	63.5	54.7	153.2	138.2	56.1	140.9	123.0	176.0
Range	NSE	5.0	0.4	1.4	0.5	2.9	2.4	0.7	2.3	2.4	3.9
Count		27	21	6	21	27	6	6	27	27	27

### 3.2. Impact of Spatial Resolution

Several papers have noted a scale dependence of error caused by the inability of coarse-resolution products to adequately represent mean areal precipitation in smaller basins because their sampling involves an area much larger than the basin (e.g., Nikolopoulos, Anagnostou [14]). Here, we investigate the scale dependence of rainfall error first by comparing the CMORPH and PERSIANN products with their fine-scale counterparts and then by examining changes in PBIAS as a function of watershed size.

The PERSIANN CCS product has a spatial resolution of 0.04 degrees and has a similar size to stage IV bins across the study area. When compared to PERSIANN, the PERSIANN CCS product consistently performed better in each of the three watersheds for all performance statistics. However, the gap in performance statistics did not grow as watershed size decreased, as may be expected if scale issues were the root cause of the discrepancy. It is difficult to identify the primary causes for the differing performance given PERSIANN CCS uses different processing algorithms.

Unlike the PERSIANN products, there was virtually no difference between CMORPH and the CMORPH 8KM product with regard to performance statistics. This suggests the downscaling techniques employed by the CMORPH 8KM product are not adequate if their intent is to provide a more detailed spatial representation of rainfall.

### 3.3. GPM Rainfall Events

The two largest rain events from the dataset occurred in May and October of 2015, and both resulted in significant flash flood events along the Blanco River [42]. These events were captured by GPM and offer an initial look at GPM performance for short duration high magnitude storms. Figure 5 shows performance statistic results for each of the real-time products (PERSIANN, PERSIANN-CCS, TRMM-RT, and CMORPH RAW) along with the Early and Late GPM runs. Generally, the GPM products performed better than did the other real-time satellite products. For the May 2015 event, the Early product produced better estimates than the Late run, with the opposite pattern for the October 2015 event. Gauge corrected estimates (Table 3) showed a significant underestimation of the events, which is not surprising given it is adjusted to monthly values. The Early GPM product failed to capture the storm event of October 2015 showed by the negative value of Nash coefficient (Figure 5).

As anticipated, hydrograph results closely mimic the rainfall fields with respect to their ability to overestimate and underestimate the reference Stage IV forcing. The hydrographs driven by Stage IV rainfall along with satellite results for the nine storm events at the Guadalupe basin outlet are shown in Figure 6 (same as Figure 3). The hydrographs from the products were able to capture the bi-modal behavior of the hydrograph but with a high range of accuracy levels for November 2004 and May 2014 events. Some of the errors were quite high, indicating that the rainfall errors were amplified in the resulting runoff hydrograph. In the case of the events that have a one peak hydrograph, most of the products tend to underestimate the hydrograph by a considerable amount. As expected, the

hydrographs driven by the GPM Early and Late products had less errors than those driven by the Final products due to the severe underestimation of rainfall by the latter as described above (see Figures 3 and 4). In all the fall events, the pattern of the hydrograph was more or less captured, but with very significant underestimation of the precipitation. For the events that occurred in May, the magnitude and the pattern of the stage IV seem to be the mean value of the hydrographs from the satellite-based products.

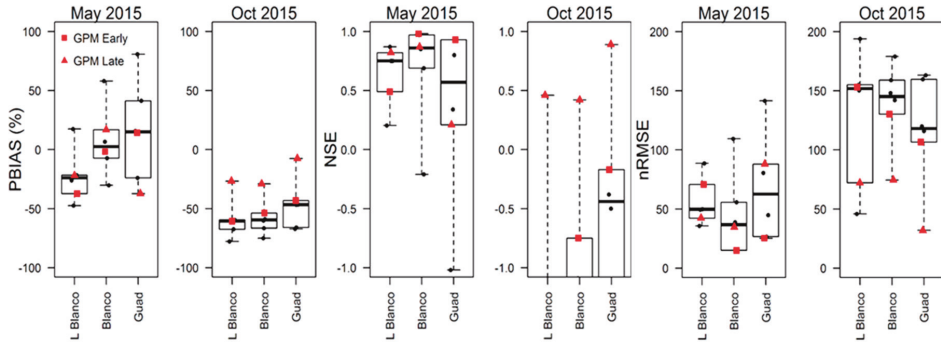


**Figure 5.** Performance statistic results for the non-gauge adjusted satellite results for the May and October 2015 storms that included the GPM products.

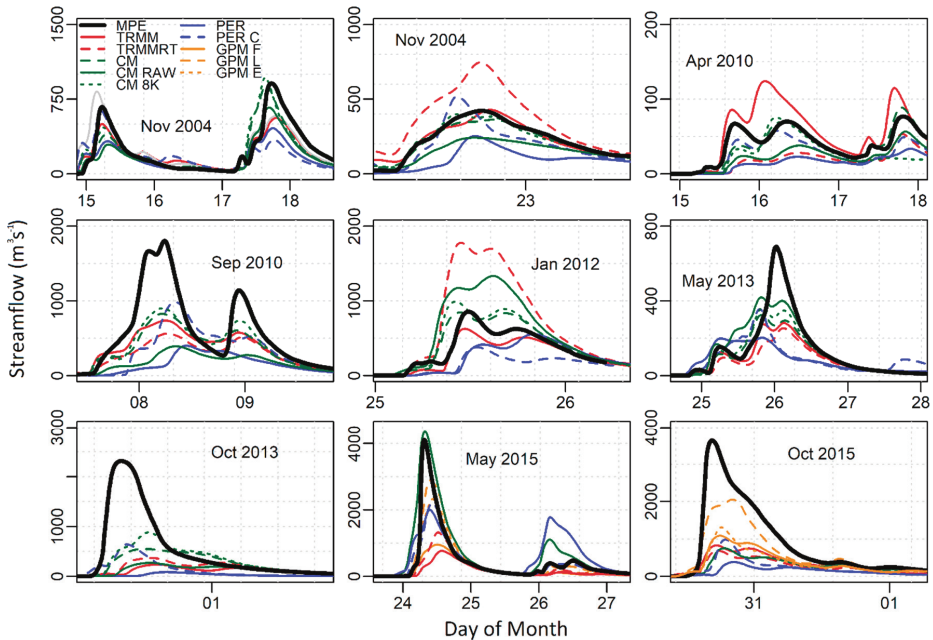


**Figure 6.** Streamflow hydrographs at the Blanco watershed outlet. Legend labels are abbreviated as follows: MPE—Stage IV, TRMM—TRMM 3B42, CM—CMORPH CDR, GPM F—GPM IMERG FINAL, CM 8K—CMORPH 8KM, PER C—PERSIANN CCS, GPM E—GPM IMERG EARLY, GPM L—GPM IMERG LATE, CM RAW—CMORPH RAW, TRMM-RT—TRMM-RT 3B42, and PER—PERSIANN.

The performance of the precipitation products in the simulated hydrograph followed a similar pattern as described in the precipitation analysis. However, the variability of the products seems to increase as the scale of the watershed increases. Boxplot results showing performance statistics at each of the three basins are displayed in Figure 7. The CMORPH product (labeled as CM) showed higher Nash coefficient in Little Blanco (the smallest basin) but as the size of the watershed increased, the performance was seen to plummet. A similar pattern was observed in most the products when moving from Little Blanco to Guadalupe. All evaluation criteria showed a very wide range and high variability in the case of the Guadalupe Basin (Figure 7). The accumulated effect of all the discrepancies in the products across the watershed caused a significant increase in variability at the outlet. However, the increase in spatial domain of the watershed improved the performance of the GPM Late product across all the criteria.

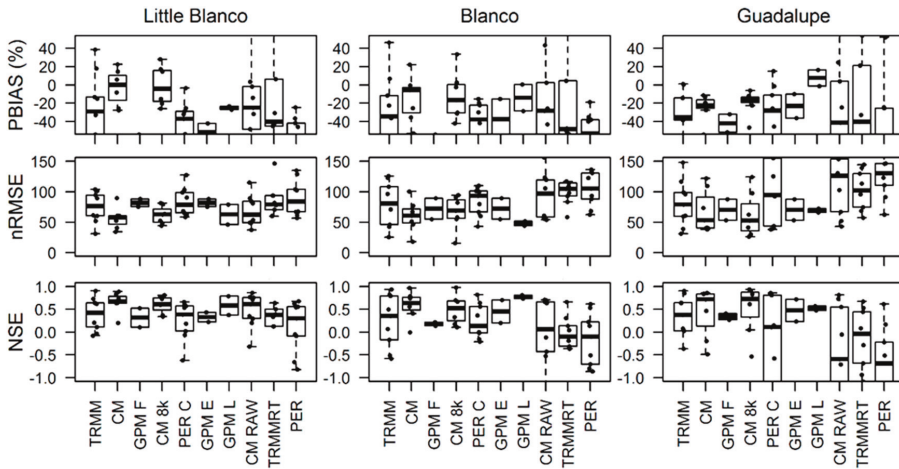


**Figure 7.** Boxplots for hydrograph performance statistics for all spatial domains. X-axis labels abbreviations and boxplot representations are the same as those described in Figure 4.

3.4. GPM Model Simulations

GPM products showed a higher Nash Coefficient than their counterparts in both events in all spatial scales except in the case of Little Blanco for the May 2015 event. Moreover, the Late GPM product outclassed the Early GPM product in almost all the criteria and in all spatial domains. There is no clear pattern of the impact of scale effect on a single product but, in case of GPM products, the performance of the PBIAS was improved as the spatial domain increased. However, the variability of the performance of the non-gauge adjusted products increased as the spatial domain size increased (Figure 8).

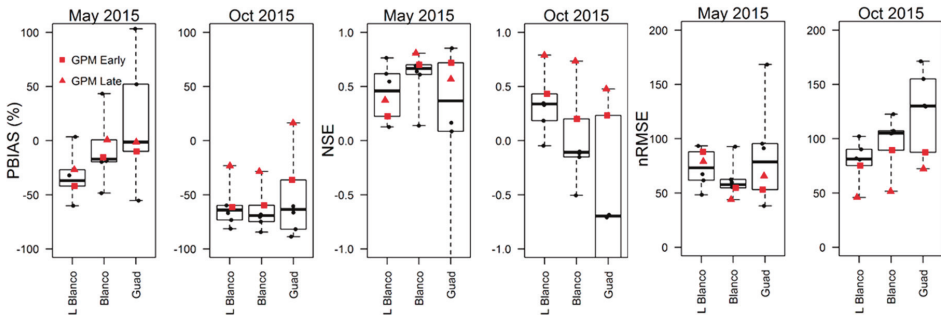


**Figure 8.** Performance statistic results for the non-gauge adjusted satellite results for the May and October 2015 storms that included the GPM products (for the hydrographs).

3.5. Error Propagation

The error was seen to propagate from the precipitation dataset to the hydrograph at the outlet. The propagation was magnified in all of the criteria shown in Figure 9 except in the case of the streamflow PBIAS. Moreover, the pattern was seen across all the spatial domains in the same manner. The scale effect of the spatial domains does not seem to affect the error propagation, as they were very close in all the evaluation criteria (Figure 9).

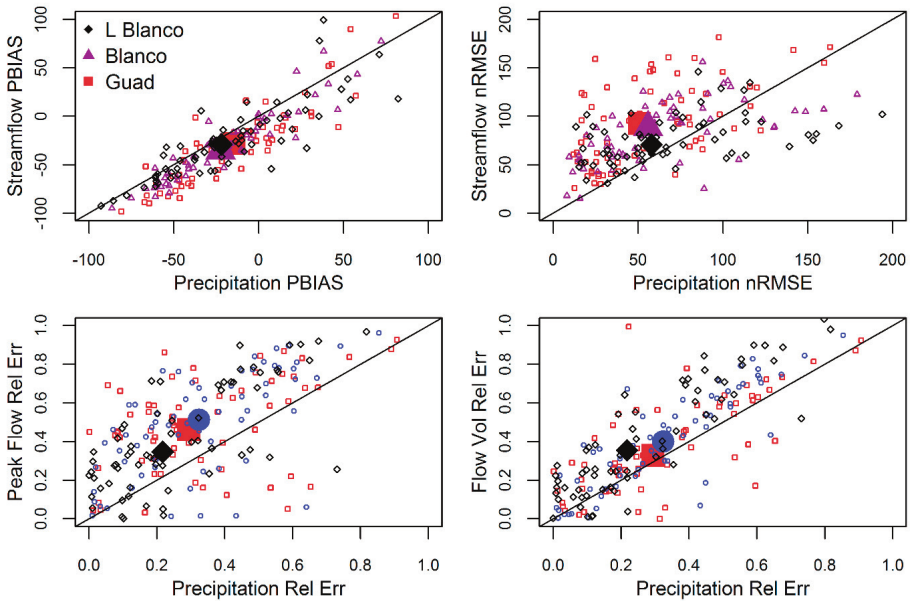


**Figure 9.** Annual Error propagations descriptions comparing streamflow and precipitation percent bias (PBIAS) and normalized root-mean-square-error (nRMSE) (top left and top right, respectively) and relative error in precipitation versus peak flow relative error (bottom left) and streamflow volume relative error (bottom right) N.B. the big markers represent the mean value.

#### 4. Conclusions

Precipitation is the main driver of all the hydrologic models that are used to predict/forecast the relationship between rainfall and runoff. Moreover, rainfall amount and distribution represent the major components of the floodplain analysis and water resource management practices. That is why it is a significant achievement to capture the spatial and temporal distribution of rainfall, since the accuracy of almost all hydrologic processes depends on the accuracy of the precipitation estimates. Rain gauges are only reliable for a very small area because of the intermittent behavior of precipitation. Radars have problems with beam blockage in complex terrain and lack even distribution across the globe. Satellite-based precipitation estimation with high spatiotemporal resolution has a potential to capture the spatiotemporal distribution of precipitation if the products and algorithms are improved to a reasonable accuracy.

The assessment of ten satellite-based precipitation products was carried in relation to the radar stage IV (NCEP product) over Guadalupe river basin with a drainage area of around 9000 km<sup>2</sup>. Moreover, the assessment was done in two smaller sub-watersheds of the Guadalupe river basin (Little Blanco River (178 km<sup>2</sup>) and the Blanco River (1130 km<sup>2</sup>)). This procedure was done to assess the scale impact on the accuracy of the products. Nine significantly large events with a wide spatial coverage were used in the analysis.

Furthermore, to understand the propagation of rainfall error into the predicted runoff, hydrologic model simulations were implemented. GSSHA, a physically-based fully distributed hydrologic model, forced with those ten satellite-based precipitation products, was used to simulate the rainfall-runoff relationship for the basins. The most widely used model evaluation criteria such as Nash-Sutcliffe, PBIAS, nRMSE, and relative error were used in the assessment of both precipitation and hydrographs of the outlet.

The products underestimated the storm events in relation to the radar product Stage IV. This pattern was seen in several other studies over various regions of the world [14–16,56]. Moreover, the satellite-based precipitation products showed a very compact distribution in all the evaluation criteria in the case of the largest basin. Both products of CMORPH showed a very high correlation in all spatial domains and was reflected with an average Nash-Sutcliffe coefficient of 0.81. GPM Early was found to be inconsistent with a very high variance of Nash coefficient in all spatial domains (from -0.46 to 0.38), however, the variance was decreased as the watershed size increased. This is mainly due to the smoothing caused by averaging over a larger area. Among all GPM products, the Final product underestimated rainfall most, indicating that the methodology used to prepare the product (using climatology and rain gauges) probably was not able to capture the areas and/or periods of very intense localized rainfall. Surprisingly, TRMM also showed a very high variance in all the performance statics, especially in the two small watersheds (from -4.0 to 0.99 with an average of 0.16). In contrast, the TRMM RT (non-gauge corrected product of TRMM) product showed relatively better performance of Nash-Sutcliffe with an average of 0.39 and a range from 0.05 to 0.82.

The pattern of the precipitation estimates was also reflected on the simulated hydrograph forced by the precipitation products. The average Nash-Sutcliffe coefficient was reduced from 0.81 in precipitation to 0.58 in the runoff for CMORPH. CMORPH product showed higher Nash coefficient in Little Blanco (the smallest basin) but as the size of the watershed increased, the performance was seen to plummet. A similar pattern was observed in most of the products when moving from Little Blanco to Guadalupe. However, the increase in the spatial domain of the watershed improved the performance of the GPM Late product across all the criteria.

The error was seen to amplify as it propagated from the precipitation dataset to the hydrograph at the outlet. The propagation was magnified in all of the evaluation criteria except in the case of the streamflow PBIAS. Moreover, the pattern was seen across all the spatial domains in the same manner. The scale effect of the spatial domains does not seem to affect the error propagation as it was very close in all of the evaluation criteria.

In summary, the satellite-based precipitation products provide very high spatiotemporal resolution precipitation estimates. However, the estimates lack accuracy, especially at a local scale. The products underestimate heavy storm events significantly, and the errors were amplified in the runoff hydrographs generated.

**Author Contributions:** H.O.S. and C.F. designed the overall study. C.F. downloaded the remote sensing products and prepared and performed the hydrologic model simulations with input from H.O.S. D.G. helped C.F. with post-analysis of the model outputs and preparation of the first draft. C.F. and H.O.S. reviewed and revised the manuscript. H.O.S. did the final overall proofreading of the manuscript.

**Acknowledgments:** This research funded in part by the U.S. Army Research Office (Grant W912HZ-14-P-0160). This support is cordially acknowledged.

## References

1. Dai, A. Precipitation Characteristics in Eighteen Coupled climate models. *J. Clim.* **2006**, *19*, 4605–4630. [CrossRef]
2. New, M.; Todd, M.; Hulme, M.; Jones, P. Precipitation measurements and trends in the twentieth century. *Int. J. Clim.* **2001**, *21*, 1889–1922. [CrossRef]
3. Krajewski, W.; Smith, J. Radar hydrology: Rainfall estimation. *Adv. Water Resour.* **2002**, *25*, 1387–1394. [CrossRef]
4. Wang, X.; Xie, H.; Sharif, H.; Zeitle, J. Validating NEXRAD MPE and Stage III precipitation products for uniform rainfall on the Upper Guadalupe River Basin of the Texas Hill Country. *J. Hydrol.* **2008**, *348*, 73–86. [CrossRef]
5. Habib, E.; Larson, B.F.; Grascel, J. Validation of NEXRAD multisensor precipitation estimates using an experimental dense rain gauge network in south Louisiana. *J. Hydrol.* **2009**, *373*, 463–478. [CrossRef]
6. Maddox, R.A.; Zhang, J.; Gourley, J.J.; Howard, K.W. Weather radar coverage over the contiguous United States. *Weather Forecast.* **2002**, *17*, 927–934. [CrossRef]
7. Nicholson, S.E.; Some, B.; McCollum, J.; Nelkin, E.; Klotter, D.; Berte, Y.; Diallo, B.M.; Gaye, I.; Kpabebe, G.; Ndiaye, O.; et al. Validation of TRMM and other rainfall estimates with a high-density gauge dataset for West Africa. Part II: Validation of TRMM rainfall products. *J. Appl. Meteorol.* **2003**, *42*, 1355–1368. [CrossRef]
8. McCollum, J.R.; Krajewski, W.F.; Ferraro, R.R.; Ba, M.B. Evaluation of biases of satellite rainfall estimation algorithms over the continental United States. *J. Appl. Meteorol.* **2002**, *41*, 1065–1080. [CrossRef]
9. Ebert, E.E.; Janowiak, J.E.; Kidd, C. Comparison of near-real-time precipitation estimates from satellite observations and numerical models. *Bull. Am. Meteorol. Soc.* **2007**, *88*, 47–64. [CrossRef]
10. Sapiano, M.; Arkin, P. An intercomparison and validation of high-resolution satellite precipitation estimates with 3-hourly gauge data. *J. Hydrometeorol.* **2009**, *10*, 149–166. [CrossRef]
11. Thiemig, V.; Rojas, R.; Zambrano-Bigiarini, M.; Levizzani, V.; de Roo, A. Validation of satellite-based precipitation products over sparsely gauged African river basins. *J. Hydrometeorol.* **2012**, *13*, 1760–1783. [CrossRef]
12. Hirpa, F.A.; Gebremichael, M.; Hopson, T. Evaluation of high-resolution satellite precipitation products over very complex terrain in Ethiopia. *J. Appl. Meteorol. Climatol.* **2010**, *49*, 1044–1051. [CrossRef]
13. Mantas, V.; Liu, Z.; Caro, C.; Pereira, A.J.S.C. Validation of TRMM multi-satellite precipitation analysis (TMPA) products in the Peruvian Andes. *Atmos. Res.* **2015**, *163*, 132–145. [CrossRef]
14. Nikolopoulos, E.I.; Anagnostou, E.N.; Hossain, F.; Gebremichael, M.; Borga, M. Understanding the scale relationships of uncertainty propagation of satellite rainfall through a distributed hydrologic model. *J. Hydrometeorol.* **2010**, *11*, 520–532. [CrossRef]
15. AghaKouchak, A.; Behrangi, A.; Sorooshian, S.; Hsu, K.; Amitai, E. Evaluation of satellite-retrieved extreme precipitation rates across the central United States. *J. Geophys. Res. Atmos.* **2011**, *116*. [CrossRef]
16. Mehran, A.; AghaKouchak, A. Capabilities of satellite precipitation datasets to estimate heavy precipitation rates at different temporal accumulations. *Hydrol. Process.* **2014**, *28*, 2262–2270. [CrossRef]

17. Mei, Y.; Anagnostou, E.N.; Nikolopoulos, E.I.; Borga, M. Error analysis of satellite precipitation products in mountainous basins. *J. Hydrometeorol.* **2014**, *15*, 1778–1793. [CrossRef]
18. Shen, Y.; Xiong, A.; Wang, Y.; Xie, P. Performance of high-resolution satellite precipitation products over China. *J. Geophys. Res. Atmos.* **2010**, *115*. [CrossRef]
19. Vernimmen, R.; Hooijer, A.; Mamenun; Aldrian, E.; van Dijk, A.I.J.M. Evaluation and bias correction of satellite rainfall data for drought monitoring in Indonesia. *Hydrol. Earth Syst. Sci.* **2012**, *16*, 133–146. [CrossRef]
20. Wehbe, Y.; Ghebreyesus, D.; Temimi, M.; Milewski, A.; al Mandous, A. Assessment of the consistency among global precipitation products over the United Arab Emirates. *J. Hydrol. Reg. Stud.* **2017**, *12*, 122–135. [CrossRef]
21. Omranian, E.; Sharif, H.O. Evaluation of the Global Precipitation Measurement (GPM) Satellite Rainfall Products Over the Lower Colorado River Basin, Texas. *J. Am. Water Resour. Assoc.* **2018**. [CrossRef]
22. Sharif, H.O.; Ogden, F.L.; Krajewski, W.F.; Xue, M. Numerical simulations of radar rainfall error propagation. *Water Resour. Res.* **2002**, *38*, 15-1–15-14. [CrossRef]
23. Sharif, H.O.; Ogden, F.L.; Krajewski, W.F.; Xue, M. Statistical analysis of radar rainfall error propagation. *J. Hydrometeorol.* **2004**, *5*, 199–212. [CrossRef]
24. Borga, M. Accuracy of radar rainfall estimates for streamflow simulation. *J. Hydrol.* **2002**, *267*, 26–39. [CrossRef]
25. Vivoni, E.R.; Entekhabi, D.; Hoffman, R.N. Error propagation of radar rainfall nowcasting fields through a fully distributed flood forecasting model. *J. Appl. Meteorol. Climatol.* **2007**, *46*, 932–940. [CrossRef]
26. Gebregiorgis, A.S.; Tian, Y.; Peters-Lidard, C.D.; Hossain, F. Tracing hydrologic model simulation error as a function of satellite rainfall estimation bias components and land use and land cover conditions. *Water Resour. Res.* **2012**, *48*. [CrossRef]
27. Maggioni, V.; Vergara, H.J.; Anagnostou, E.N.; Gourley, J.J.; Hong, Y.; Stampoulis, D. Investigating the applicability of error correction ensembles of satellite rainfall products in river flow simulations. *J. Hydrometeorol.* **2013**, *14*, 1194–1211. [CrossRef]
28. Chintalapudi, S.; Sharif, H.O.; Xie, H. Sensitivity of distributed hydrologic simulations to ground and satellite based rainfall products. *Water* **2014**, *6*, 1221–1245. [CrossRef]
29. Su, F.; Gao, H.; Huffman, G.J.; Lettenmaier, D.P. Potential utility of the real-time TMPA-RT precipitation estimates in streamflow prediction. *J. Hydrometeorol.* **2011**, *12*, 444–455. [CrossRef]
30. Wu, H.; Adler, R.F.; Tian, Y.; Huffman, G.J.; Li, H.; Wang, J. Real-time global flood estimation using satellite-based precipitation and a coupled land surface and routing model. *Water Resour. Res.* **2014**, *50*, 2693–2717. [CrossRef]
31. Vergara, H.; Hong, Y.; Gourley, J.J.; Anagnostou, E.N.; Maggioni, V.; Stampoulis, D.; Kirstetter, Pi. Effects of resolution of satellite-based rainfall estimates on hydrologic modeling skill at different scales. *J. Hydrometeorol.* **2014**, *15*, 593–613. [CrossRef]
32. Mei, Y.; Nikolopoulos, E.I.; Anagnostou, E.N.; Borga, M. Evaluating satellite precipitation error propagation in runoff simulations of mountainous basins. *J. Hydrometeorol.* **2016**, *17*, 1407–1423. [CrossRef]
33. Yong, B.; Ren, L.; Hong, Y.; Wang, J.; Gourley, J.J.; Jiang, S.; Chen, X.; Wang, W. Hydrologic evaluation of Multisatellite Precipitation Analysis standard precipitation products in basins beyond its inclined latitude band: A case study in Laohahe basin, China. *Water Resour. Res.* **2010**, *46*. [CrossRef]
34. Downer, C.W.; Ogden, F.L. GSSHA: Model to simulate diverse stream flow producing processes. *J. Hydrol. Eng.* **2004**, *9*, 161–174. [CrossRef]
35. Afshari, S.; Omranian, E.; Feng, D. *Relative Sensitivity of Flood Inundation Extent by Different Physical and Semi-Empirical Models*; CUAHSI Technical Report No. 13; The Consortium of Universities for the Advancement of Hydrologic Science, Inc.: Washington, DC, USA, 2016; pp. 19–24.
36. Sharif, H.O.; Sparks, L.; Hassan, A.A.; Zeitler, J.; Xie, H. Application of a distributed hydrologic model to the November 17, 2004, flood of Bull Creek watershed, Austin, Texas. *J. Hydrol. Eng.* **2010**, *15*, 651–657. [CrossRef]
37. Caran, S.C.; Baker, V.R. Flooding along the Balcones escarpment, central Texas. In *The Balcones Escarpment-Geology, Hydrology, Ecology and Social Development in Central TEXAS*; Geological Society of America: Boulder, CO, USA, 1986; pp. 1–14.

38. Baker, V.R. *Flood Hazards along the Balcones Escarpment in Central Texas Alternative Approaches to Their Recognition, Mapping, and Management*; Bureau of Economic Geology Circular; Bureau of Economic Geology, University of Texas at Austin: Austin, TX, USA, 1975.
39. Smith, J.A.; Baeck, M.L.; Morrison, J.E.; Sturdevant-Rees, P. Catastrophic rainfall and flooding in Texas. *J. Hydrometeorol.* **2000**, *1*, 5–25. [CrossRef]
40. Furl, C.; Sharif, H.O.; el Hassan, A.; Mazari, N.; Burtch, D.; Mullendore, G.L. Hydrometeorological Analysis of Tropical Storm Hermine and Central Texas Flash Flooding, September 2010. *J. Hydrometeorol.* **2015**, *16*, 2311–2327. [CrossRef]
41. Patton, P.C.; Baker, V.R. Morphometry and floods in small drainage basins subject to diverse hydrogeomorphic controls. *Water Resour. Res.* **1976**, *12*, 941–952. [CrossRef]
42. Furl, C.; Sharif, H.; Zeitler, J.W.; el Hassan, A.; Joseph, J. Hydrometeorology of the catastrophic Blanco river flood in South Texas, May 2015. *J. Hydrol. Reg. Stud.* **2018**, *15*, 90–104. [CrossRef]
43. Lin, Y.; Mitchell, K.E. 1.2 the NCEP stage II/IV hourly precipitation analyses: Development and applications. In Proceedings of the 19th Conference Hydrology, American Meteorological Society, San Diego, CA, USA, 9–13 January 2005.
44. Fulton, R.A.; Breidenbach, J.P.; Seo, D.; Miller, D.A.; O'Bannon, T. The WSR-88D rainfall algorithm. *Weather Forecast.* **1998**, *13*, 377–395. [CrossRef]
45. Nelson, B.R.; Prat, O.P.; Seo, D.-J.; Habib, E. Assessment and implications of NCEP stage IV quantitative precipitation estimates for product intercomparisons. *Weather Forecast.* **2016**, *31*, 371–394. [CrossRef]
46. Huffman, G.J.; Bolvin, D.T.; Nelkin, E.J. Integrated Multi-satellite Retrievals for GPM (IMERG) technical documentation. *NASA/GSFC Code* **2015**, *612*, 47.
47. Yong, B.; Liu, D.; Gourley, J.J.; Tian, Y.; Huffman, G.J.; Ren, L.; Hong, Y. Global view of real-time TRMM multisatellite precipitation analysis: Implications for its successor global precipitation measurement mission. *Bull. Am. Meteorol. Soc.* **2015**, *96*, 283–296. [CrossRef]
48. Hsu, K.; Gao, X.; Sorooshian, S.; Gupta, H.V. Precipitation estimation from remotely sensed information using artificial neural networks. *J. Appl. Meteorol.* **1997**, *36*, 1176–1190. [CrossRef]
49. Sorooshian, S.; Hsu, K.; Gao, X.; Gupta, H.V.; Imam, B.; Braithwaite, D. Evaluation of PERSIANN system satellite-based estimates of tropical rainfall. *Bull. Am. Meteorol. Soc.* **2000**, *81*, 2035–2046. [CrossRef]
50. Joyce, R.J.; Janowiak, J.E.; Arkin, P.A.; Xie, P. CMORPH: A method that produces global precipitation estimates from passive microwave and infrared data at high spatial and temporal resolution. *J. Hydrometeorol.* **2004**, *5*, 487–503. [CrossRef]
51. Huffman, G.J.; Bolvin, D.T.; Nelkin, E.J.; Wolff, D.B.; Adler, R.F.; Gu, G.; Hong, Y.; Bowman, K.P.; Stocker, E.F. The TRMM multisatellite precipitation analysis (TMPA): Quasi-global, multiyear, combined-sensor precipitation estimates at fine scales. *J. Hydrometeorol.* **2007**, *8*, 38–55. [CrossRef]
52. Downer, C.W.; Ogden, F.L. *Gridded Surface Subsurface Hydrologic Analysis (GSSHA) User's Manual*; Version 1.43 for Watershed Modeling System 6.1.; Engineer Research and Development Center Coastal and Hydraulics Lab.: Vicksburg, MS, USA, 2006.
53. Ogden, F.L.; Saghafian, B. Green and Ampt infiltration with redistribution. *J. Irrig. Drain. Eng.* **1997**, *123*, 386–393. [CrossRef]
54. Rawls, W.J.; Brakensiek, D.L.; Miller, N. Green-Ampt infiltration parameters from soils data. *J. Hydraul. Eng.* **1983**, *109*, 62–70. [CrossRef]
55. Zambrano-Bigiarini, M. Package 'hydroGOF': Goodness-of-Fit Functions for Comparison of Simulated and Observed Hydrological Time Series. R package Version 0.3-8. Available online: <https://cran.r-project.org/web/packages/hydroGOF/hydroGOF.pdf> (accessed on 8 February 2018).
56. Su, F.; Hong, Y.; Lettenmaier, D.P. Evaluation of TRMM Multisatellite Precipitation Analysis (TMPA) and its utility in hydrologic prediction in the La Plata Basin. *J. Hydrometeorol.* **2008**, *9*, 622–640. [CrossRef]